School of Civil and Mechanical Engineering
Department of Mechanical Engineering

Fluid and Thermal behaviour of Multi-Phase Flow through Curved Ducts

Nima Nadim

This thesis is presented for the Degree of
Doctor of Philosophy
of
Curtin University

September 2012

Declaration

To the best of my knowledge and belief this thesis contains no material previously published by any other person except where due acknowledgment has been made. This thesis contains no material which has been accepted for the award of any other degree or diploma in any university.

Date:
Signature:

Dedicated to

Tooba, Mahsa and Ali

For turning some dreams into reality

Abstract

Fluid flow through curved ducts is influenced by the centrifugal action arising from duct curvature and has behaviour uniquely different to fluid flow through straight ducts. In such flows, centrifugal forces induce secondary flow vortices and produce spiralling fluid motion within curved ducts. Secondary flow promotes fluid mixing with intrinsic potential for thermal enhancement and, exhibits possibility of fluid instability and additional secondary vortices under certain flow conditions. Reviewing published numerical and experimental work, this thesis discusses the current knowledge-base on secondary flow in curved ducts and, identifies the deficiencies in analyses and fundamental understanding. It then presents an extensive research study capturing advanced aspects of secondary flow behaviour in single and two-phase fluid flow through curved channels of several practical geometries and the associated wall heat transfer processes.

As a key contribution to the field and overcoming current limitations, this research study develops a new three-dimensional numerical model for single-phase fluid flow in curved ducts incorporating vortex structure (helicity) approach and a curvilinear mesh system. The model is validated against the published data to ascertain modelling accuracy. Considering rectangular, elliptical and circular ducts, the flow patterns and thermal characteristics are obtained for a range of duct aspect ratios, flow rates and wall heat fluxes. Results are analysed for parametric influences and construed for clearer physical understanding of the flow mechanics involved. The study formulates two analytical techniques whereby secondary vortex detection is integrated into the computational process with unprecedented accuracy and reliability. The vortex inception at flow instability is carefully examined with respect to the duct aspect ratio, duct geometry and flow rate. An entropy-based thermal optimisation technique is developed for fluid flow through curved ducts.

Extending the single-phase model, novel simulations are developed to investigate the multi-phase flow in heated curved ducts. The variants of these models are separately formulated

to examine the immiscible fluid mixture flow and the two-phase flow boiling situations in heated curved ducts. These advanced curved duct flow simulation models are validated against the available data. Along with physical interpretations, the predicted results are used to appraise the parametric influences on phase and void fraction distribution, unique flow features and thermal characteristics. A channel flow optimisation method based on thermal and viscous fluid irreversibilities is proposed and tested with a view to develop a practical design tool.

FIGURES

CONTENTS

NOMENCLATURE

Ar	Aspect Ratio= a/b
A_i	Interfacial area (m^2)
a	Height of duct cross section (m)
b	Width of cross section (m)
C_f	Skin friction coefficient $= \frac{2\tau_w}{\rho U_{in}^2}$
C_p	Specific Heat (j/kg-K)
C_{pq}	Isobaric heat capacity of phase-q (J/kg-mol.K)
D_h	Hydraulic diameter (m)
d_b	Bubble diameter (m)
$\vec{F}_{q-body}$	Body forces on phase-q (N)
$\vec{F}_{lift}$	Lift force (N)
$\vec{F}^{D}{}_{pq}$	Drift force of phase-p on phase-q (N)
$\vec{F}^{TD}{}_{pq}$	Turbulence drift force of phase-p on phase-q (N)
G	Mass flow rate ($kg/m^2.s$)
G_k, G_ε	Turbulence kinetic energy and dissipation rate production terms
g	Gravity acceleration (m/s^2)
H^*	Dimensionless Helicity
h	Heat transfer coefficient ($W/m^2.K$)
h_{sl}	Ranz-Marshal heat transfer coefficient ($W/m^2.K$)
h_{pq}	Inter-phase enthalpy (kJ/kg)
h_{fg}	Latent heat of evaporation (kJ/kg)

$\Delta h_{s\tan dard}$	Standard enthalpy difference between phases (J/kg.mol)
I_T	Turbulence intensity ($s^{1/2}/m^{1/2}$)
K	Dean number = $\left(\frac{D_h}{R}\right)^{\frac{1}{2}}$ Re
k	Turbulence kinetic energy (m^2/s^2)
k_f	Bulk thermal conductivity (W/m.K)
L_H	Length of heated section (m)
L_{NH}	Length of non-heated section (m)
$\dot{m}_{pq}$	Mass transfer from phase-p to phase-q (kg/s)
Nu	Nusselt number
p	Static pressure (Pa)
$p*$	Dimensionless static pressure = $\frac{p}{1/2\rho U_{in}^2}$
p	Pressure (MPa)
Re_b	Bubble Reynolds number
Re_∇	Bubble shear Reynolds number
q	Applied heat flux(W/m)
$\dot{q}_L$	Liquid phase heat transfer (W/m)
$\dot{q}_V$	Vapour phase heat transfer (W/m)
$\dot{q}_Q$	Quenching heat flux (W/m)
$\dot{q}_E$	Evaporating heat flux (W/m)
$\dot{q}_w$	Wall heat flux (W/m^2)
R	Radius of curved channel (mm)
Re	Reynolds number = $\frac{U_{in} D_h}{\upsilon}$

$\widehat{S}$ direction	Coordinate along duct cross section defining secondary flow
S_T	Energy source term
S_k, S_ε	Turbulence source term in bubbly flow regime
S_T'''	Volumetric average entropy generation rate due to heat flow ($W/m^3 \cdot K$)
S_p'''	Volumetric average entropy generation rate due to friction ($W/m^3 \cdot K$)
S_{gen}'''	Total entropy generation ($W/m^3 \cdot K$)
T_{in}	Bulk inlet temperature (K)
T_{sat}	Saturation temperature (K)
$\Delta T_{sub} = T_{sat} - T_{in}$	Sub-cooled inlet temperature (K)
u, v, w	Cartesian velocities component (m/s)
u^*, v^*, w^*	Dimensionless velocity $= \frac{u, v, w}{U_{in}}$
u', v', w'	Turbulence fluctuating velocities (m/s)
U_{in}	Velocity at duct inlet (m/s)
V_r	Axial velocity (m/s)
x, y, z	Coordinates (m)
$\vec{v}_q$	Velocity of q-phase
$\vec{v}_{pq}$	Relative density of p-phase to q-phase
v_{xq}, v_{yq}, v_{zq}	Cartesian velocity components of phase-q (m/s)
x, y, z	Coordinates (m)
y^+	Dimensionless wall distance

Greek symbols

α	Volume of fraction
γ	Curvature ratio
ε	Turbulence dissipation rate (m^2/s^3)
θ	Angular position of cross section (deg)
μ	Dynamic viscosity (Ns/m^2)
ν	Kinematic Viscosity (m^2/s)
ρ	Density (kg/m^3)
$\sigma_{xx}, \tau_{xy}, \tau_{xz}$	Viscous shear stress (pa)
τ	Viscous stress tensor
τ^T	Turbulence stress tensor
$\tau^T{}_T$	Temperature turbulence stress tensor
$\vec{\omega}$	Vorticity (1/s)
Φ	Dissipation function
ω	Specific turbulence dissipation rate ($1/s$)

Chapter 1

Introduction

1.1. Background

Curved fluid flow passages are common in most technological systems involving fluid transport, heat exchange and thermal power generation such as, compact heat exchangers, boilers, gas turbines blades, air conditioning systems and refrigeration. The geometrical curvature in fluid passages brings about special flow characteristics essentially from the centrifugal forces induced by the passage radius of curvature and the fluid momentum associated with continuous flow directional change. These additional body forces acting on the fluid mass create unique flow features that are fundamentally different to those of flow through straight passages. These flow features also significantly influence the heat transport mechanisms in curved passages that would behave vastly different to thermal characteristics in straight ducts. The purpose of the study presented in this thesis is to examine the intricate aspects of the complex flow behaviour and thermal transport in fluid flow passages with stream-wise curvature while identifying the influence from various flow and geometrical parameters. In achieving this, a review of relevant literature is performed to identify the deficiencies in the present state of knowledge. Novel methodologies are then formulated and outcomes are analysed for clearer fundamental understanding of the flow mechanisms involved.

The curvature of a fluid channel imparts two key effects on the fluid flow. It generates on the flowing fluid a centrifugal action that radially emanates from the channel's centre of curvature. These centrifugal forces act on the axial fluid flow to induce a lateral (or radial) fluid movement from the inner channel wall towards the outer wall. The interactive action between this lateral fluid movement and the axial flow develops a spiralling fluid motion in curved duct making the flow behaviour uniquely different to that within straight flow passages. The lateral fluid movement generated by the centrifugal action is referred to as the secondary flow, that characterises the flow patterns within curved channels and appear as large counter-rotating pairs of vortices in

the duct cross section. The strength of these secondary vortices is essentially dependant on the flow axial velocity through the curved channel.

The channel curvature-induced centrifugal action also forms a radial fluid pressure gradient within the flow through curved channels. This pressure field is set up with a positive gradient from the inner to outer channel wall while its intensity is determined by the axial flow velocity. The lateral fluid circulation of the secondary flow occurs within this adverse pressure gradient, which acts to retard the secondary fluid motion assisted by the viscous effects in the vicinity of the channel outer wall.

The combined actions of the positive radial pressure gradient and viscous forces cause the development of a stagnant fluid region near the outer wall. When the axial flow rate is increased beyond a certain critical value, the radial pressure gradient would become dominant and disturb the fluid equilibrium in the stagnant region at the outer wall. This triggers a highly-localised fluid circulation in the stagnant region to form smaller additional pairs of vortices. This flow condition is known as the Dean's Instability and the additional vortices are named Dean Vortices, in recognition of the pioneering work by Dean [1], who first discovered this flow phenomenon in curved flow geometries. It has been established that the dimensionless group Dean Number, K as defined by $K = \left[\frac{D_h}{R}\right]^{\frac{1}{2}} Re$, characterises the secondary flow behaviour in curved channels equivalent to the Reynolds number in conventional straight pipe flows.

The secondary flow structures have a very profound influence on the thermal transport characteristics within curved channels. In its most basic form, the secondary flow promotes fluid mixing in the flow channel and breaks up the thermal boundary layer near the heated wall to bring about a certain degree of heat transfer augmentation. With this intrinsic thermal enhancement ability, the secondary flow behaviour delivers significant heat transport benefits even under laminar flow conditions.

The flow patterns and thermal characteristics associated with secondary flow are far more complex than the flow behaviour within straight channels. These are fundamentally dependant on the flow geometry, inclusive of channel cross section, channel aspect ratio and curvature, and the external operating parameters such as the flow rate and wall heat flux. Multi-phase fluid flow, with or without boiling in curved channels, and the flow turbulence would introduce further complexities to the secondary flow behaviour and associated heat transfer processes. Compounded by these, the

secondary flow behaviour is not fully comprehended by the current state of published research in this area.

In reported literature, the early attempts on curved duct research were confined to experimental studies, which primarily focussed on visualisation methods to understand the secondary flow characteristics. These were limited in scope due to measurement constraints and flow control difficulties. Rectangular duct geometries have been traditionally considered in these investigations on curved ducts. By virtue of shape, such ducts offer less flow confinement for secondary vortex formation, making it relatively easier for experimentation, including flow visualisation and numerical modelling. Ducts with elliptical and circular cross sections have been lightly treated in research in spite of being common and popular channel geometries used in industrial and technological systems.

With the advent of advanced computational tools and methodologies, extended opportunities are now available for precise numerical simulations and parametric investigations, by which the curved channel flow behaviour can be analysed for deeper and improved understanding. In these, a major challenge is to synthesise more realistic numerical formulations that are congruent with the complex nature of the secondary flow vortex motion. In this regard, almost all reported numerical simulations up to now have significant modelling deficiencies, in terms of geometrical range of applicability, consistency of results and parametric considerations. The parametric influences of the channel geometry and the flow variables remain unexplored and poorly understood. Additionally, there are no decisive techniques for defining or identifying the onset of Dean's Instability and, the formation of Dean vortices and their locations. Most of these models do not accommodate the temperature dependency of fluid properties variations leading to unrealistic predictions, especially with heated curved channels. Majority of reported models are limited to single-phase fluid flow systems and, are not adaptable or conducive for multi-phase fluid flows. In this latter type of fluid flow, specific requirements exist to capture the distribution of fluid phases and account for the physical interaction across phases through heat and mass transfer processes, interfacial evaporation and surface tension effects.

1.2. Scope of work

The study presented in this thesis is carefully developed and carried out to address many of the above-mentioned shortcomings in the current state of fundamental knowledge and analytical methodologies in secondary flow behaviour within heated curved channels. Formulating necessary User Defined Functions (UDF) for the computational fluid dynamics software FLUENT, the study develops novel simulations models for single and multi-phase fluid flows through curved channels having several practical cross sectional geometries. These models incorporate flow parameters and mesh arrangements that are highly congruent with the secondary vortex structures compared to previous models for much realistic representation of intricate flow features. As a critical analytical tool for this field of research, the study also develops two intuitive approaches for detecting the onset of Dean Instability with an appraisal of their merits. An optimisation scheme is developed and tested for curved passages in achieving most effective thermal performance for a given set of parametric conditions and geometry.

In discussing above details, the thesis is broadly arranged to provide the aspects that are specific to the individual situations of single phase, immiscible two-phase and two-phase boiling fluid flows through curved channels.

1.3. Research Objectives

This research study examines the fluid flow and heat transfer characteristics in curved channels for single and two-phase fluid flows. In the latter case, both immiscible (or non-mixing) two-phase mixtures and the fluid flow boiling are considered. Fluid and thermal characteristics are appraised with regard to secondary flow features and parametric influences within rectangular, elliptical and circular channel geometries.

In view of these, the objectives of the study are as follows:

(a) For single-phase fluid flow in curved channels:

- Improving on current modelling limitations, a novel three-dimensional simulation approach is developed for single phase fluid flow through curved rectangular, elliptical and circular geometries. Suitable mesh arrangements are considered with the necessary capabilities in capturing intricate details of

secondary vortex formation and to achieve high consistency of results. The model is validated against the published experimental data.

- In fulfilling a critical need for this field of research, practical and accurate criteria are formulated to identify the onset of Dean's Instability and Dean vortex generation. These are appraised for their suitability for various channel geometries under consideration.
- Above single-phase model is deployed to investigate the fluid behaviour within rectangular, elliptical and circular channels in terms of fluid flow rate, channel aspect ratio and wall heat flux.
- A thermal optimisation scheme is developed for the fluid flow through curved channels.

(b) For immiscible two-phase fluid flow in curved channels:

- Accounting for the simultaneous flow of two non-mixing fluid components within a curved passage, a new three-dimensional simulation is developed specifically for this type of two-phase flow in a circular channel. Suitable mesh arrangements are considered with the necessary capabilities in capturing the distribution of immiscible fluid phases, unique features arising from momentum transfer between phases and the details of secondary vortex formation in each fluid phase. The model consistency is tested and established.
- Above immiscible two-phase model is deployed to investigate the fluid behaviour in a circular channel within each fluid phase, identifying the interactive nature of centrifugal forces and momentum transfer across phase boundaries. Thermal characteristics unique to this type of flow are examined with appropriate physical explanations.
- A thermal optimisation scheme is developed for this two-phase fluid flow through curved channels.

(c) For two-phase flow boiling in curved channels:

- Above single-phase model is modified and extended to two-phase flow boiling situation by considering wall heat partitioning techniques, where both mass and heat transfer are considered with the phase interfacial momentum transfer. This new approach represents the most accurate to-date in terms of physical

mechanisms involved among two-phase flow models for this type of fluid flow with boiling.

- The model is deployed to examine the unique characteristics of phase distribution and boiling heat transfer in circular channels whereby special flow features are identified.

CHAPTER 2

Literature Survey

2.1. Secondary flow and hydrodynamic instability

The pioneering experimental work on the secondary flow and hydrodynamic instability was carried out by Eustice [1], investigating the resistance against fluid flow in metal pipes - both straight and curved. First, the concept of critical velocity (threshold of transient regime) was shown to be extended to a higher flow rate for curved pipes and, then he reported new proportion of fluid with velocity below critical fluid velocity. These experiments showed that the flow rate in a curved channel to be proportional to the velocity raised to the power "n". Further work by Eustice [2] showed the flow pattern in a curved channel by visualizing streamlines. Figure 2.1 shows the test set-up used by Eustice [2] wherein he observed streamlines based on the location of dye injectors This was the first published work on the description of secondary flow in curved pipes which also qualitatively discussed the parametrical effect of flow and geometry effect, and the critical flow rate extension.

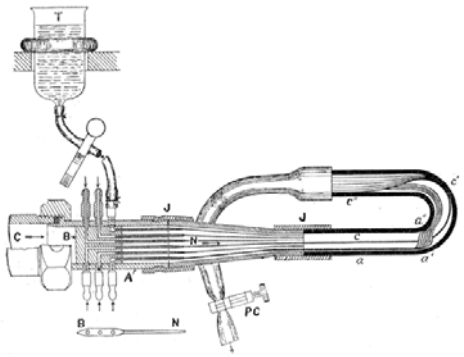

Figure 2.1. Eustice's experimental arrangement [2]

The first analytical and numerical work was established by Dean [3] in a coiled pipe with a circular cross section in an attempt to model what Eustice had reported experimentally demonstrating the complicated and unique behaviour of streamlines in such a field. Assuming small curvature ratio (diameter of pipe to radius of curvature)

and consequently negligible axial velocity gradient Dean managed to obtain a good qualitative agreement between his model and experimental model.

The results from this work showed the effect of flow rate on pressure drop and confirmed that pressure drop does not change linearly with Reynolds number and accordingly introduced effective dimensionless ratio in curved channels. Using stream-function definition he analytically proved flow features and streamline arrangements are related to the ratio of $\frac{D}{R}\mathrm{Re}^2$, where D and R are the diameter of tube and curvature radius, respectively. The model was utilized to investigate flow streamlines in a given cross section of pipe to demonstrate secondary flow and counter rotating vortices in top and bottom sides of the cross section; moreover, by tracking streamlines in a plane at the middle of pipe, the study provided the longitudinal distance along coiled pipe at which a certain streamline moves from outer wall to inner wall. Two points were concluded out of these demonstrations; first the spiral motion of streamlines and then effect of flow rate (in laminar regime) on vortex structure. As an extension of this work, Dean published two reports [4,5] that provided an analytical correlation for pressure drop versus bulk flow velocity in curved channels. Dean modified initial definition of influential dimensionless number in curved channels to what is known as the Dean number ($K = (\frac{D}{R})^{1/2}\,\mathrm{Re}$) and explained its effect for different curvature ratios.

Another important aspect of this research was identifying a new type of instability for curved channels which was fundamentally different from turbulence. Beyond a certain flow rate, far below the turbulence threshold, streamlines were found to be broken in some flow areas where the flow was steady and incompressible. Dean's numerical model showed that a type of small disturbance which could not persist in a straight channel is possible in a curved channel. Parabolic velocity profile previously proved for pipe flows was showed to be inconsistent for curved channels.

Dean's work was of utmost value in that he pointed to a basis of correlation describing a particular feature of fluid flow in a curved channel.

White [6] carried out experimental work over a range of flows at least twice as great as that investigated by Eustice to explore the relation between Dean number and pressure drop in curved and coiled pipes. Using oil with different densities and water, White succeeded to carry out the experiment over a wide range of Reynolds numbers (0.06 to

40,000) and concluded that the results covered the whole practical range of the criterion he suggested. He explained that an increase in the resistance of curved pipe against flow is due to an internal circulation in the plane of the cross section of the pipe, superimposed upon the normal streamline velocity distribution and suggested a correlation for pressure drop in such curved pipes based on the Dean number. The traditional experimental approach of streamlines observation was utilized for turbulence investigation and Reynolds number of 9000 and 6000 suggested as a transient threshold for curved pipe with curvature ratio of 1/15 and 1/50 respectively which confirmed extended range of flow for laminar regime due to introduction of radial pressure effect in curved channels.

Baylis [7] conducted an experimental investigation for flow in curved channel with a square cross section focusing on the flow resistance and boundary layer behaviour at high Dean number and confirmed the dependence of flow resistance on $K^{1/2}$. Humphery et al [8] developed a numerical solution of Navier-Stokes equation using the finite difference method to calculate flow features of water in a 90˚ bend of 40 x 40 mm cross-section and additionally carried out an experiment at a Reynolds number, based on the hydraulic diameter and bulk velocity of 790 (corresponding to a Dean number of 368).

This research is one of the earliest reports which investigated the effect of aspect ratio (height to width) of cross section as a critical geometrical parameter by quantitative identification of the critical Dean number; they suggested a minimum Dean number of 125 just applicable for regions beyond 25˚ of curvature for the occurrence of Dean instability.

Experimental work of Cheng et al. [9] considering flow visualization in a rectangular curved channel with wide range of aspect ratios (1 to 12) reported critical Dean numbers for different aspect ratios validated the previous numerical work by emphasizing the importance of aspect ratio as a key geometrical parameter affecting the interaction between secondary flow and so-called boundary-value-type vortices. The axial development of Dean vortices along a curved channel with a rectangular cross section was studied by Ghia and Sokhey [10] for both parabolic and flat inlet velocity profiles and critical Dean numbers for different axial positions were obtained. Enayet et al [11] compared a moderately curved channel with square cross section for strongly curved channels in terms of turbulent characteristics. They reported displacement of maximum

velocity to the outside of the bend and resulted in an accumulation of slow moving fluid on the inner wall. Accordingly inward flows at the side-walls ensured that the boundary layers remained thin. Turbulence intensity and shear stress measured in this research were reported to be higher at inner corners of cross section at the outlet plane.

Sugiyama et al [12] conducted an experiment to describe the development of secondary flow and reported the effect of aspect ratio and curvature ratio. As it is evident from Figure 2.2 the flow pattern changes as a result of flow rate increase in curved channels.

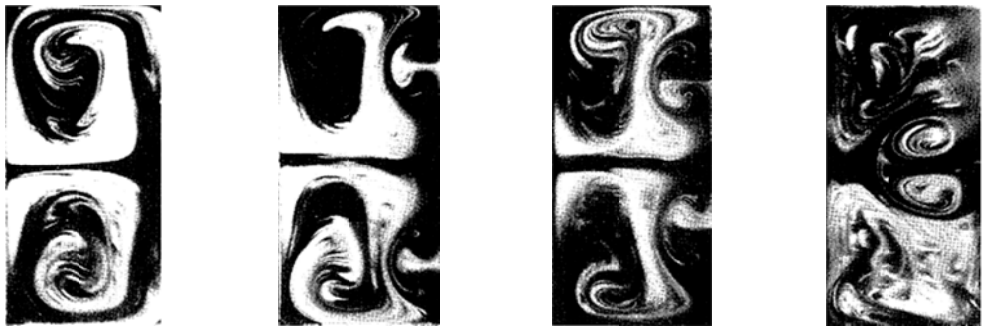

K=127 K=180 K=224 K=391

Figure 2.2. Cross sectional view of flow pattern at the end of curvature (experiment by Sugiyama et al [12])

Based on the obtained flow visualization they classified the sequence of secondary flow development into three steps. First, the occurrence of secondary flow as a well-known pattern of cross sectional flow, then, occurrence of retarded layer near to outer wall in addition to main secondary vortices and finally the inception of additional vortices developed by retarded layer. The report defined critical Dean number at which retarded region develops new pairs of vortices and suggested higher critical Dean number for aspect ratio less than 1 as compared to 2, and then an abrupt rise for changing aspect ratio from 1 to 2; however, their experimental technique failed beyond a certain Dean number for each aspect ratio to clearly capture the cross-sectional vortex structure and they left this area without any discussion. Dong and Ebadian [13] numerically investigated the flow field and vortices formed in elliptical curved channels, reported some differences compared to rectangular channels in the formation of the secondary flow instability.

Chandratilleke et al [14] report an extensive parametric study examining the effects of curvature ratio, aspect ratio and external wall heat flux. Their numerical formulation was effectively a 2-dimensional model incorporating toroidal coordinates and a stream function approach with dynamic similarity in axial direction. Intersecting contours of

stream function were adapted as a qualitative criterion for establishing the occurrence of flow instability and Dean vortices. Chandratilleke et al [14, 29, 30] presented results for rectangular ducts for a comprehensive range of Dean numbers $25 \leq K \leq 500$, aspect ratio $1 \leq Ar \leq 8$. They represented a trend for the variation of the critical Dean number versus the aspect ratio and curvature ratio, which confirmed the trends observed in Cheng et al [9] with some modification based on their qualitative stream function approach.

In an attempt to define a quantitative criterion to identify the onset of Dean instability, Fellouah et al [15] conducted a numerical-experimental analysis. They used the finite-volume CFD package to solve the three-dimensional Navier-Stokes equation for laminar, incompressible flow. They also had a well-controlled water tunnel with long entrance section and a curved testing section for flow visualization using the LIF (Laser induced florescence) technique. They suggested that the radial gradient of the axial velocity measured along the line connecting eye to eye of the Dean vortices as a criterion for Dean instability inception and compared their prediction, based on defined criterion, with LIF flow visualization.

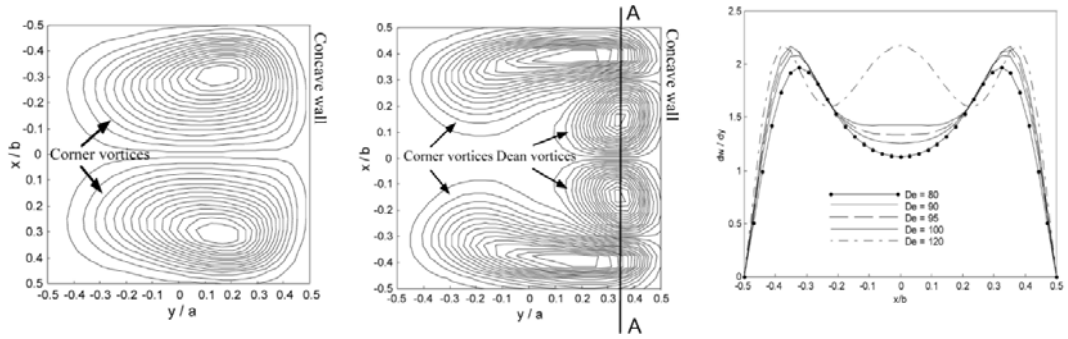

K=80 K=150 Radial gradient of axial velocity

Figure 2.3. Quantitative assessment of instability inception by Fellouah et al [15]

The criterion delivered an original attempt of quantitative assessment of instability; yet, was not generalized regarding of geometry and flow rate since it was not possible to predict the exact position of Dean vortices' eye for different geometries and flow conditions as shown in Figure 2.3. The critical Dean numbers for different aspect and curvature ratios did not suggest considerable difference with the previous two-dimensional numerical models or classic experimental studies by Cheng et al [9] or Ghia and Sokhey [10]. Their study investigated the concept of fully development

length in curved channels for mentioned inlet velocity profiles and suggested different correlations for cross section of rectangular cross section. Helin et al [16] used a finite volume numerical model to investigate secondary flow and Dean instability with a shear-thinning Phan-Thien–Tanner fluid in a U-curved channel of square section for tiny range of Dean number ($125 \leq K \leq 150$). The first results of this research obtained a lower flow rate required for the transition to the four-cell structure (known as Dean instability threshold) for viscoelastic fluid as compared to Newtonian fluid with the same condition as the inertial term is increased. Moreover, for explored range of Dean numbers they established that increasing the power-law index n of the Phan- Thien–Tanner model retards the onset of additional Dean vortices; in contrast, additional computations with an Oldroyd-B fluid demonstrated that the size and intensity of the secondary vortices present in the four-cell pattern increase with elasticity.

Fellouah et al [17] later used their own developed quantitative criterion to identify the effect of rheological fluid behaviour on the Dean instability of power-law and Bingham fluids in curved rectangular ducts. Their results confirmed a decrease in the critical Dean number as a result of power law index increase and showed an opposite effect for Bingham number. Variation of rheological parameters however was found to be merely effective on position of vortices and not on size of them and the flow visualization showed that the effect of the yield stress on the shape of the flow to be the dominant parameter.

2.2. Thermal behaviour with secondary flow

Secondary flow which is basically due to centrifugal effect is a lateral-cross sectional motion of fluid results in an increase in the mixing rate. Accordingly the rate of convective heat transfer is substantially increased by the new main and extra vortices in the flow field. Moreover, the contribution of the extra body force due to buoyancy effect for a given flow rate and material properties will be considerable resulting in a mutual interaction between buoyancy and centrifugal source terms. Common application of curved channel and tubes in addition to the importance of the unique physics of heat transfer in such flow fields has attracted researchers during past decades. Accordingly, extensive numerical and experimental reports are available in literature regarding the mutual effect of heating and curvature on flow field and heat transfer in curved confined geometries.

Cheng et al [18] conducted a numerical analysis of forced convection in a curved channel with rectangular cross section, investigating the velocity and temperature fields as well as Nusselt number on the heated wall. The study included a dimensionless parameter analysis investigating the effect of critical values such as flow rate, aspect ratio and Prandtl number on the velocity and temperature profiles in comparison with correspondent values in a straight channel. The results suggested the trend for temperature similar to velocity profile where the maximum value is pushed toward the outer wall as Dean number increases. The effect of aspect ratio on the flow field was found to displace the centre of secondary vortices and consequently make a variation in velocity and temperature field; however, Prandtl number was found to be just effective on heat transfer and not on streamlines. Mori et al [19] reported a more detailed analysis for hydro-thermal assessment of curved channel with a square cross section and by assuming material properties to be temperature-independent, neglecting the effect of temperature field on velocity and streamlines. They also conducted an experiment using air as fluid and four independent heaters with constant heat flux on walls and successfully validated their analytical solution up to Re=8000 including transition range of flow for both velocity and Nusselt number. As a main contribution of this study, they explained the structure of boundary layer region and the important effect of that on both velocity and temperature fields by taking secondary flow effect into account for obtaining boundary layer equation particularly for curved channels. The suggested Nusselt number correlation, based on such an analysis, was showed to be more accurate rather than previously reported estimations as compare to experimental results.

Tyagi and Sharma [20] published another study of laminar forced convection with circular cross section taking viscous dissipation effect into account. They claimed the presence of a marked distinction between thermal boundary condition cases of straight and curved tubes when the cross-sections of both are circular due to circumferentially non-uniform viscous dissipation. Based on such an assumption they carried out a perturbation analysis to investigate the velocity and temperature field and consequently assessed convective heat transfer by discussing Nusselt number. Their result, interestingly, showed a reversed effect of viscous dissipation rate in curved channel. An analytical correlation for Nusselt number in curved channels, as a result, was modified taking viscous heating effect into account.

Mixed convection flows in concentric curved annular ducts with constant wall temperature boundary condition were studied numerically by Hoon [21]. He focused on effect of radius ratio (ratio of the inner core radius to the outer pipe radius), the Dean number and Grashof number on Nusselt number and friction factor. As one of the earliest studies which highlighted the relative importance of centrifugal and buoyancy forces in curved tubes, Hoon explained the secondary flow pattern exhibits a strong asymmetry as a result Grashof number increase (i.e. increase of buoyancy force) when the Dean number is low enough. On other hand, by increasing the Dean number, the flow field was found to be pushed back to its almost symmetric pattern. Comparing two different orders of Grashof number, results suggested a slight dependence of Nusselt number and friction factor to either Dean number or radius ratio for $Gr = 12500$ whereas these ratios increase as either the radius ratio increases or Dean number, contrary to the case of $Gr = 12.5$.

Targett et al [22] solved the equations for the conservation for mass, momentum and energy for fully developed angular flow and fully developed convection in the annulus between two concentric cylinders. Flow was assumed to have invariant physical properties, Newtonian behaviour and negligible viscous dissipation and accordingly reported Nusselt number to be mostly dependent on heat flux density ratio as well as Dean number. They assessed Nusselt number for complete range of heat flux density ratios, (both positive and negative), on the inner and outer surfaces, for Dean numbers up to 2.5 times the critical value for the onset of vertical motion and the computed results were concluded to be applicable, within some mentioned geometrical restrictions, as a good approximation for true double-spiral heat exchangers in terms of the local Dean number. The effect of Dean vortices on forced convection was studied by Ligrani and Choi [23]; to accomplish this task, buoyancy influences were minimized by orienting the channel so that gravity acted in the span-wise direction perpendicular to the bulk flow direction and additionally, a new procedure was applied to deduce forced convection Nusselt numbers from Nusselt numbers measured in a mixed convection environment with relatively weak buoyancy. In given procedure, Nusselt numbers at different $\beta\Delta T$ were measured, by varying heating power, and then measured data are extrapolated to $\beta\Delta T = 0$ which gives forced convection Nusselt numbers with no buoyancy influences. Comparing concave and convex walls they reported the Nusselt number exceeding significantly at concave (outer) wall over a certain Dean number (or longitudinal length of channel) due to secondary flows which result as tiny Gortler-like

vortices start to form near the concave surface of the channel. They later experimentally compared mixed convection in straight and curved channels with buoyancy orthogonal to the forced flow [24].

For Grashof number ranging from 0 to 5×10^6 and Reynolds numbers from 343 to 2057 (i.e. laminar and transient regime) they discussed the interaction between centrifugal and buoyancy forces, effect of curvature, and summarized four different heat transfer regimes; pure natural convection, mixed convection with strong buoyancy, mixed convection with weak buoyancy, and pure forced convection. For large aspect ratio of 40, they suggested that pure natural convection is present when $Gr.\mathrm{Re}^{0.5} > 900\,000$, and pure forced convection is present for $Gr.\mathrm{Re}^2$ values near zero. Mixed convection with strong buoyancy is present when Re<687, $Gr.\mathrm{Re}^2 > 50$, and $Gr.\mathrm{Re}^{0.5} < 900\,000$. For Re < 687, mixed convection with weak buoyancy was observed for $Gr.\mathrm{Re}^2 < 50$. For Re > 687, mixed convection with weak buoyancy was observed for < 900,000. Figure 2.4 compares Nusselt number on concave and convex walls for different heat transfer regimes whereas regardless of the Reynolds number, forced convection Nu data lie on the ordinate at $Gr.\mathrm{Re}^2 = 0$ and pure natural convection values are located at the right-hand side. Mixed convection data are distributed in between the natural convection and forced convection data.

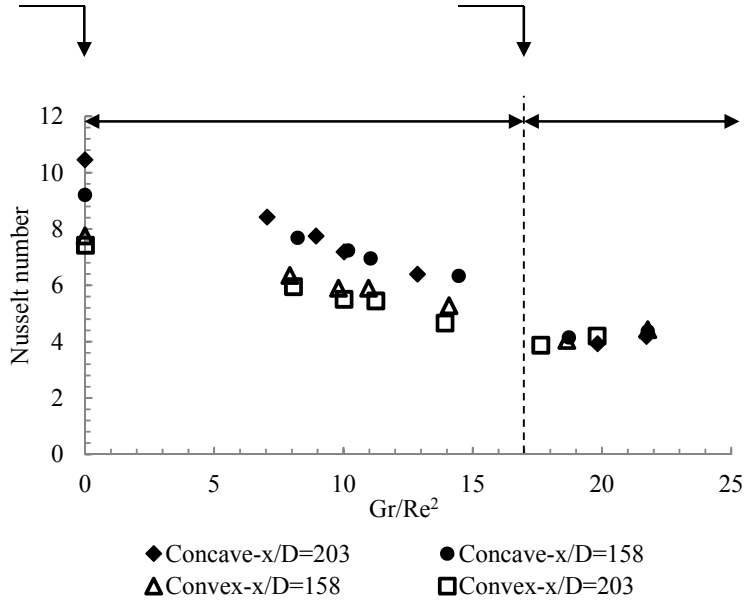

Figure 2.4. Nusselt number in different heat transfer regimes at Re=1371, Ligrani and S. Choi [24]

Mixed convection with strong buoyancy was reported as having non-linearity, strong coupling in the field equations, and complicated convolutions of the temperature field, especially near walls. This is the reason for the non-linear dependence of Nusselt numbers on $\beta\Delta T$ and reference bulk velocity of fluid between pure forced convection and pure natural convection limits. As a complementary report Ligrani and Hedlund published the experimental assessment of same geometry for turbulent flow [25] and suggested that Nusselt numbers measured on the concave surface in a given portion of the channel are significantly higher than values measured on the convex surface when compared at the same x/D. It was concluded that Dean vortex pairs are not only present in the channel at these Dean numbers, but they also strongly influence thermal flow field behaviour, even when the curved channel flow is fully turbulent (or near-fully turbulent).

Silva et al [26] developed a finite volume numerical model to investigate and compare elliptical and rectangular cross section. They successfully captured streamlines representing secondary flow and beyond a certain Dean number Dean vortices. Friction factor for elliptical cross section did not show a substantial dependence on aspect ratio; however, for rectangular cross section by exceeding Dean number from 200, friction factor values varied for different aspect ratios. Comparing such a trend with pressure drop in straight channels it was concluded that friction factor in curved ducts (regardless of cross-section shape) for low Dean numbers is mostly affected by axial flow rather than secondary flow. For elliptical cross section such an effective threshold value for flow rate is postponed substantially since as a result cross section shape, higher centrifugal force is required to overcome lateral pressure and push Dean vortices toward the out wall. They highlighted the fact that regardless of Dean instability, as the secondary flow itself is more intense in curved channels for all ranges of Dean number duct with elliptical cross section experience a higher rate of pressure drop rather than rectangular cross sections. Heat transfer represented by Nusselt number, unlike to pressure drop, was found to be essentially affected by secondary flow for all range of Dean numbers. For elliptical cross section more intense secondary flow will enhance Nusselt number significantly as compare to rectangular cross section as it is expected; yet, the enhancement due to extra vortices merged with outer wall is again postponed by the same mechanism mentioned for friction factor.

Andrade et al [27] investigated the effect of temperature dependent viscosity on heat transfer and velocity profile for a fully developed forced convection case in a curved duct using a finite element model. They analysed both cooling and heating cases and under cooling conditions, the Nusselt values with variable-viscosity were found to be lower than the constant-properties results due to the increase of the viscosity at the inner points of the curved tube section that reduces the secondary flow effects and the heat transfer rate.

An experimental study performed by Christopher and Mudawar [28], discussed the enhancement mechanism of heat transfer in curved channel for a fully turbulent regime. They first compared stream-wise Nusselt number variation for straight and curved channels and obtained different thermally fully developed region for each case. At a location close to the inlet, the Nusselt number was found to be almost the same as those obtained for straight channel. It showed that it takes a finite distance for the secondary flows to develop and influence the heat transfer as previously for laminar flow secondary flow was suggested to be effective beyond turn angles $\theta > 15°$. Further downstream of this point they obtained an enhancement ratio defined as $\frac{Nu_{curved}}{Nu_{straight}} = \mathrm{Re}^{0.046}(\frac{D_h}{2R})^{0.1}$ and improved the former available correlations by 6%.

Chandratilleke et al [29] has used the idea of secondary flow to optimize heat exchanger performance based on former studies. Following this study, they conducted an experiment [30] to investigate mutual effect of heating and centrifugal force in curved channel with rectangular cross section; in which they experimentally assessed a wide range of effective parameters by view of flow visualization and heat transfer analysis. They used air as the main flow and smoke as flow indicator and managed to capture cross sectional view of vortices structure in different cross section through curved duct. Their result showed the most vivid prospect of centrifugal versus buoyancy force interaction qualitatively where the effect of geometrical parameters (e.g. aspect ratio, curvature ratio and hydraulic diameter) was demonstrated. Beyond a mere qualitative assessment, their important work [13] which was the most comprehensive numerical model up to the time, used a finite volume CFD code for incompressible laminar flow which was validated against their own former experiment and utilized stream-function for instability analysis of vortex structure whereas curved section was uniformly heated. Using Boussinesq approximation, the effect of buoyancy force was taken into

account and the precise assessment of interaction between that with centrifugal force was carried out. As it is evident from Figure 2.5, for a non-heated channel the centrifugal force merely is affecting flow field leads a symmetrical vortex structure where the Dean vortices are apparent next to the outer wall; nevertheless, by applying heating buoyancy will perform as a vertical driven flow and significantly changes flow domain. The unbalanced secondary vortex motion found to enhance fluid velocities parallel to the outer wall in the top half of the duct and impede fluid velocities in the bottom half. Combined with the repositioning of the stagnant region, this velocity imbalance near the outer wall reduces the formation potential of flow reversal cells for a given aspect ratio. Hence, the Dean vortices are diminished in number with the application of external heating on the outer wall of curved ducts.

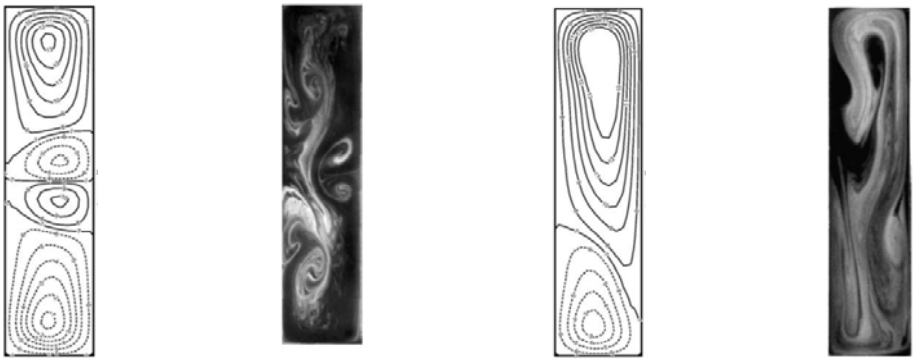

a) non-heated wall

b) partially heated channel ($q=25W/m^2$)

Figure 2.5. Effectiveness of buoyancy; assessment of stream function versus flow visualization at the curvature exit (θ=180, K=380, Ar=4) [13]

They reported an intense temperature gradient at the outer wall of the duct and an unsymmetrical temperature field in the fluid at lower flow rates due to thermal stratification. As the flow rate increases, the temperature field gradually acquires the symmetry associated with the stronger secondary flow-vortex motion. It was seen that for a given duct aspect ratio, increasing flow rate leads to gradual enhancement of Nusselt number. This research observed that the Nusselt number for a curved duct is 20–70% higher than that of a corresponding straight passage. This heat transfer enhancement was justified with two operating mechanisms; the secondary vortex motion gives a rise to higher fluid velocities at the outer wall and causes rapid removal of the hotter fluid there and shifting of flow distribution towards the outer wall causes thinning of the thermal boundary layer at the heated wall, (as indicated by their

temperature distribution) and leads to reduced thermal resistance to heat flow from the heated boundary to the fluid. They finally assessed the effect of aspect ratio on convective heat transfer and obtained higher Nusselt number for larger aspect ratio since more number of Dean vortices will be produced by increasing aspect ratio.

Yanase et al [31] analyzed a non-isothermal curved duct with a rectangular cross section fixed at aspect ratio of 2 using the spectral method. Their numerical research explored the linear instability and heat transfer for the case of heated outer and cooled inner wall, where parametric analysis was carried out over the range of $100 \le Gr \le 1000$ and $0 \le K \le 1000$. They assessed the range of Dean numbers for two Grashof number of 500 and 1000 in detail and obtained five branches of steady solution using the Newton-Raphson iteration method for either of cases. Accordingly, they studied linear stability of each branch with respect to two-dimensional perturbations and suggested unexpected results. It was found that among multiple steady solutions obtained, only one steady solution is linearly stable for a single range of the Dean number for $Gr = 500$, for $Gr = 1000$, on the other hand, linear stability region exists in three different intervals of the Dean number on the same branch. Unsteady analysis of the flow show that for $Gr = 500$, the laminar flow turns into chaotic through a time periodic state in a straightforward way (i.e. steady–periodic–chaotic), for $Gr = 1000$, on the other hand, the flow undergoes (i.e. steady–periodic–steady– periodic–steady–periodic–chaotic), as the Dean number increases. As a heat transfer assessment of field, they compared Nusselt number for all cases of steady, periodic and chaotic flow and reported a general increase due to curvature effect and a specific rise due to periodic and chaotic effect for those given ranges of Dean number.

Ko et al extensively assessed entropy generation analysis in curved channel field [32-35]. They first developed a finite volume CFD model which recognized the influential parameters on irreversibility due to either heat transfer or fluid friction terms [32]. For a partially heated channel with rectangular cross section they showed that for a given heat flux by increasing flow rate, FFI (fluid friction irreversibility) gradually increase and at the certain flow rate overcomes HTI (heat transfer irreversibility) which means volumetric average Bejan number approaches form 0 to 1. Ko et al studied the effect of longitudinal ribs on heat transfer and pressure drop in curved channels [33, 34] numerically. Calculation of cases with various rib size under different Dean number and heat flux revealed that addition of ribs can effectively reduce entropy generation from

heat transfer irreversibility since augmentation of secondary vortices makes temperature gradient smoother. In turn, entropy generated by fluid friction irreversibility rise up due to wider solid walls and the complex flow disturbed by ribs. Analysis of the optimal trade-off was carried out based on the minimal total entropy generation principle and optimal rib size suggested to be dependent on Dean number and heat flux. Figure 2.6 illustrates variation of Bejan number (ratio of HTI to total entropy generation) throughout a 180° curved section.

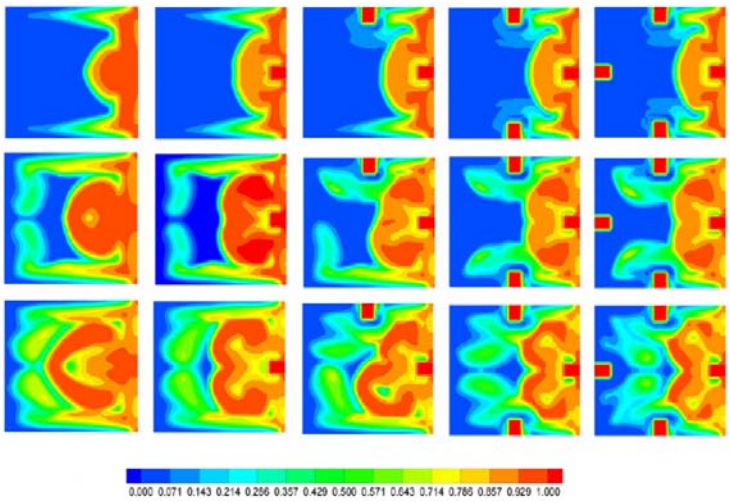

Outer heated wall located at right, K=1000, $\frac{Q.D_h}{k.T_{in=}} = 0.112$

Figure 2.6. Local Bejan number for different number of ribs in different angular position through curved section [34]

Their extensive contribution includes another study on the flow and heat transfer characteristics in curved ducts for a turbulent regime [35]. In presence of turbulence energy cascade, new terms which influence entropy generation, were considered and well established methodology of trade-off analysis for entropy generation carried out. A substantial increase in FFI was justified due to the introduction of turbulent Reynolds stress terms where aspect ratio was found to have a remarkable direct effect on enhancement of total entropy generation due to FFI.

Wang and Liu [36] addressed the effect of curvature on bifurcation structure and stability of forced convection in slightly forced micro-channels with a numerical study. They suggested that no matter how small the channel's cross-section is; the channel

curvature always generates the secondary flow in the channel cross-plane which increases the mean friction factor moderately and the Nusselt number significantly. They also examined flow stability by the direct transient computation and found fully developed flow respond against dynamic perturbation fundamentally different as Dean number changes. Three different ranges of Dean numbers were reported; the range at which flow could recover its stability after a transition time, flow leading a periodic behaviour and flow which falls into chaotic regime due to dynamic perturbation. Thereafter, they applied the same methodology on a forced convection case in a curved duct [37] with aspect ratio of 10 and curvature ratio of 0.5 and reported an optimum Dean number for maximum Nusselt number and minimum $f.\mathrm{Re}$. Figure 2.7 illustrates application of this methodology and a sample range of pseudo-Dean number analysed for Ar=10.

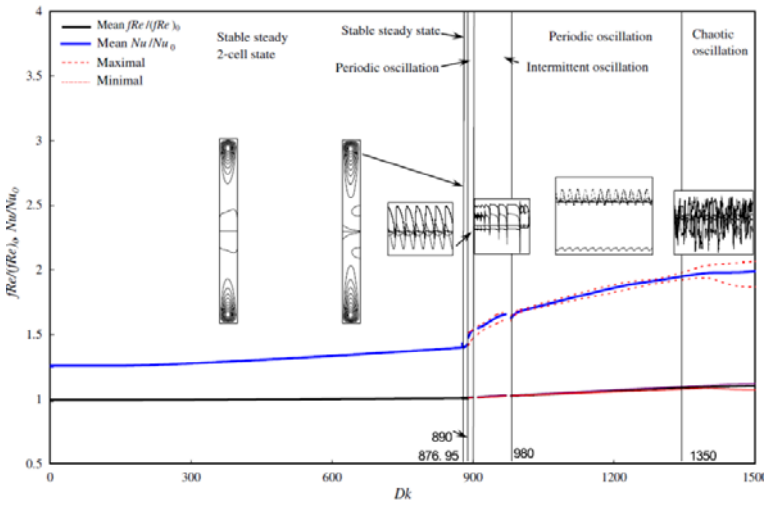

Figure 2.7. Mean Nusselt number and friction factor in different stability ranges of pseudo-Dean number [37]

The concept of dimensionless entropy generation in curved ducts was introduced by Gue et al [38] and used for a second law thermodynamic analysis of curved section with a rectangular cross section. Utilizing such an approach they reported an increase in either Reynolds number or curvature decreases dimensionless total entropy generation. Nusselt number was found to increase significantly with a penalty of slight rise in pressure drop as a result of higher aspect ratio or curvature ratio. The physical description of such trend would be directly linked with Dean vortices. Poskas et al [39] published a numerical-experimental study comparing the effect of one-side (i.e. merely concave wall) heating versus both-sides (i.e. concave and convex wall) heating in a curved rectangular channel over a wide range of Reynolds numbers ($\mathrm{Re} = 10^3 - 2\times10^5$)

and geometrical parameters ($D_h / a = 5 - 90$ and $Ar = b / a = 2 - 20$). Critical Reynolds number were reported to be identical for both case of one-side and two-side heating whereas Nusselt number increase was observed by 50% for laminar-vortex flow and by 20% for turbulent flow regime for two-side heating as compare to one side heating.

An experimental work was conducted by Fu et al [40] to investigate the effects of a reciprocating motion on mixed convection of a curved vertical cooling channel with a heated top surface, and numerical work was executed simultaneously to validate the experimental results. The experimental apparatus consisted of three main parts of a cooling channel, reciprocating movement and heating control to control and measure Reynolds numbers, frequencies, amplitudes and temperature differences. Heat transfer enhancement was found to have a direct relation with frequency since contributions of flow flowing and reciprocating motion to the heat transfer rate are mutually affected.

2.3. Secondary flow and centrifugal force in multi-phase domains

Multi-phase domain in a curved section subjected to centrifugal force behaves in specific way, regarding phase arrangement and vortex structure. Since such a domain consists of elements with different material properties such as density, viscosity and thermal properties, first phase arrangement will be unique owing to centrifugal force. Accordingly, secondary flow for fluid domain will be influenced by phase re-arrangement and momentum exchange between phases. Given the unique features of flow, this area has several applications in the industry such as phase separation, mixing and optimized heating effect.

Gao et al [41] published a work contributing some knowledge of phase separation phenomena of liquid–solid two-phase turbulent flow in curved pipes. They first numerically simulated liquid-solid phase domain, using Euler–Lagrangian scheme, and examined the effect of particle size, liquid flow-rate and coil curvature with different assumptions regarding centrifugal force, drag force, pressure gradient force, gravity force, buoyancy force, virtual mass force and lift force. They additionally conducted an experiment using a nonintrusive Malvern 2600 particle sizer based on laser diffraction to analyse the effect of secondary flow on phase separation. Their results suggested that the solid particles with higher density as compare to liquid phase are driven to outer bend due to centrifugal effect; however, by taking turbulence dispersion effect into

account trajectories becomes somewhat irregular which shows a negative effect of this term on separation due to strong randomicity. Centrifugal force was found to be prime driving force whereas the drag force and the pressure gradient play an opposite role for separation, lift force is notable near the wall and helpful to separation and virtual mass force could be omitted.

Shen et al [42] employed a 3D non-isotropic algebraic stress/flux turbulence model to simulate turbulent buoyant helicoidal flow and heat transfer in a rectangular curved open channel and by which reported a unique flow pattern including two major and one minor secondary flow eddies in a cross section. The numerical results revealed that two comparable eddies rotating in opposite directions are formed in cross sections of the turbulent buoyant helicoidal flow in a curved open channel. The boundary between the two eddies is located right in the thermocline This report was one of the early and limited researches generally discussing structure of secondary flow for immiscible flow through confined ducts and showed that the turbulence intensity is smaller in the vertical and radial directions than the tangential direction due to turbulence suppression by buoyancy and centrifugal forces. In contrast with the separation effect of curved channel for immiscible phases (including solid-fluid mixture), curved ducts are possible to be used for mixing enhancement due to additional lateral motion.

Kumar et al [43] numerically investigated the complex mixing regime of two miscible fluids in a coil of circular cross section and obtained new trends and phase distributions. Three-Dimensional grid was adopted in Cartesian coordinate system for this multi-phase model whereas the two liquids were considered to have the same properties. Two flows stream with inlet scalar concentrations of zero and unity in the two halves of a tube perpendicular to the plane of curvature and were allowed to mix by convection and diffusion. In straight tube the mixing is governed by a single parameter ($\mathrm{Re}.Sc$), where in a helical tube the mixing reported to be more complex because of the secondary flow generation due to centrifugal forces that depend on the Reynolds number (Re), Schmidt number (Sc) and the curvature ratio. This research described that mixing in curved tubes at intermediate Reynolds number is far more efficient than a straight tube of similar dimensions. The mixing in curved tubes is significantly greater at higher Reynolds numbers, whereas in straight tubes, mixing efficiency decreases as the Reynolds number increases. Since in a curved tube, the increase in Reynolds number produces increased levels of secondary flow, mixing would be enhanced. In contrast,

the increase in Reynolds number in a straight channel decreases the residence time for diffusion to take place, and accordingly the mixing efficiency. Therefore it could be concluded that the mixing mechanisms in curved and helical tubes is due to not only molecular diffusion but also secondary flow. They showed that at low Reynolds numbers (i.e. of the order of 0.1) curved tube mixers are not very practical because of the low intensity of the secondary flow, but at higher values of Reynolds number, of the order of 10–100, curved tube suggest an efficient solution. Figure 2.8 compares the mixing of miscible phases in different Reynolds number by use of scalar concentration obtained at the planes with given angular positions:

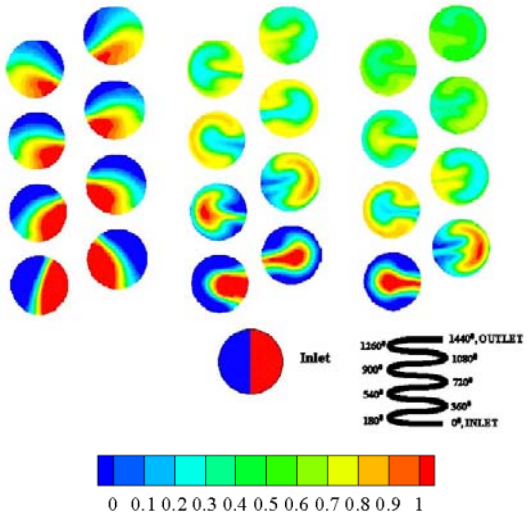

Figure 2.8. Distribution of the scalar concentration in the helical tube for Sc = 1000 after every 180 turns [44]

Wang et al [44] experimentally provided a visual observation of two-phase flow pattern of the air-water mixture through return bend tubes vertically oriented. They assessed two different tube diameters of 3mm and 6.9mm and reported phenomena such as reversal and freezing slug for larger diameter which had not been observed for horizontal configuration previously. The effect of tube diameter, mass flux, volume of fraction at inlet and curvature were examined. Accordingly, various flow regimes were discussed to evaluate interaction between three various forces; inertial, centrifugal forces which would be enhanced by flow rate effect and buoyancy force which is dependent on volume fraction and bubble sizes. It was concluded that for a given curvature and fluid (regardless of volume fraction) tube for tube diameter below a certain size all these phenomena would disappear and the only determining force will be flow inertial force.

Fries and von Rohr [45] investigated the influence of the channel radius on the mass transfer in rectangular meandering micro-channels (width 200–400 μm and height of 150μm) for gas–liquid flow. Laser induced velocimetry measurements were compared with numerical results and the symmetrical velocity profile, known from the straight channel, was found to change to an asymmetrical one for the meandering channel configuration. As a result of this variation in velocity profile in the presence of secondary flow, radial mass transfer enhanced inside liquid slug and resulted in a reduced mixing length.

2.4. Flow boiling modelling

Tube boiling is another interesting phenomenon which is significantly influenced in curved ducts due to centrifugal effect. Numerical investigation of tube boiling which is inherently a multi-phase fluid domain having heat and mass transfer has been developed by many researchers.

Luteset [46] used nitrogen and sapphire plate to investigate experimentally the transition of nucleate to film boiling on a flat surface. The study reported instability in boiling conditions and the transition between nucleate and film boiling regions, where the heat flux observed was almost three times the critical heat flux for pool boiling. Using water and refrigerant R113, Shiotsu and Hama [47] conducted forced convection film boiling experiments in a vertical cylinder with the test liquid flowing upward. The effect of parameters, such as flow rate, operating pressure, sub-cooled temperature were analysed and a correlation was suggested for forced convection film boiling heat transfer with thermal radiation. These results showed a good agreement with the published experimental data. Based on liquid sub-layer dry out mechanism, Liu et al [48] have developed one of the most up-to-date theoretical models for predicting critical heat flux for sub-cooled flow boiling. This model has been conclusively validated against the experimental data that spans almost the entire range of physical applicability. Their parametric analysis involving mass flux, pressure, pipe diameter and heated length-to-diameter ratio established the model consistency with non-uniform pipe heating and for liquids such as water, nitrogen and R113.

Baduge et al [49] experimentally investigated the boiling heat transfer characteristic in vertical capillary tubes under atmospheric pressure conditions. Within the parametric

range of mass flux (23.4 - 152.7 kg/m2s), heat flux (10 - 715 kW/m2) and dryness fraction (0 - 0.8), they showed that in vertical capillary tubes, the slug-annular and annular flow dominated the flow patterns while the liquid film evaporation was the primary heat transfer mechanism. It was concluded that the boiling correlation for normal sized tubes would under-predict heat transfer in capillary tubes.

Li et al [50] reported one of the early computational simulations on flow boiling, where they modified the RPI approach and incorporated two-phase correlations into a CFX model. This simulation was tested against the experimental results for flow boiling of liquid nitrogen in a vertical tube, and showed a significant improvement in accuracy in predicting the void fraction and wall temperature. Bostjan and Eckhard [51] have successfully simulated convective boiling in vertical annulus obtaining good qualitative agreement with experimental data. They illustrated that for two-phase modelling, the Eulerian method was a very reliable approach for simulating turbulent sub-cooled boiling although an over-prediction of velocity was evident in the near-wall regions. This work examined the void fraction, phase velocity, turbulent kinetic energy and temperature while investigating the effects of non-drag forces, bubble diameter and interfacial drag models.

Two-phase flow boiling numerical models developed thus far are very sensitive in terms of convergence and stability to the applied boundary conditions. In most cases, these models fail to predict the critical heat flux (CHF) signalling of modelling shortfalls. Sindhuja et al [52] have reported a much-improved numerical simulation, where they studied a vertical tube carrying R-407C refrigerant and uniformly heated with wall heat flux exceeding CHF. This work over- predicted the heat transfer rates compared to three established correlations, hence a modified correlation has been suggested in the study. Chen et al [53] have carried out an identical study except with more complicated geometry of horizontal coiled tube. Investigating the occurrence of CHF, they observed a non-symmetrical temperature distribution in the coil cross section, which was not rationalised but possibly arising from the coil curvature. The results developed a new correlation for predicting dry-out of R134a flow boiling in this geometry with a heat flux of 70-100 kW/m2. Li et al [54] developed a non-equilibrium two-phase boiling model. This was compared with the RPI approach and tested against four different boiling cases, namely nucleate boiling of sub-cooled water in an upward flowing heated pipe, R113 refrigerant flow through a vertical annulus with internal heated walls, three

dimensional flow boiling in a rectangular duct and, critical heat flux and post dry-out in vertical pipes. Scrutinising the mathematical formulation of FLUENT CFD software, they reported that, compared to RPI, the non-equilibrium method is more robust for boiling regime beyond the departure of nucleate boiling (DNB), where the wall heat flux could be evaluated from liquid and vapour phases by considering thin liquid wall film. The study also assessed the merits of (k-ε) and (k-ω) models. The latter model solves the turbulence equations in viscous sub-layer while complying with requirement for which a high grid resolution is required near the wall.

Publications on flow boiling in curved pipes are rather limited due to the modelling complexities arising from mutually interacting two-phase and secondary flow mechanisms. In curved passages, the centrifugal forces drive the heavier liquid component of two-phase flow towards the outer pipe wall while displacing the lighter vapour phase towards the inner wall. Consequently, unsymmetrical flow patterns are generated with fundamental changes to phase formation and affecting the heat transfer characteristics.

For flow boiling in curved ducts, Sturgis and Mudawar [54] reported essentially a single phase model where a wavy distribution was assumed for the vapour phase with liquid occupying the troughs of the wave called wetting fronts. They developed a CHF model for long curved surfaces through considerations of separated flow, thermal energy balance, interfacial instability and bubble lift-off criterion. These models were limited in scope for neglecting the interfacial condensation and were applicable only for near-saturated boiling conditions. Jo et al [55], numerically investigated the two-phase flow heat transfer in helical tubes of pressurized water reactor steam generator using a CFX code. Both the RPI boiling model and the bulk boiling model were used for the flow boiling simulations on a vertical straight pipe and helical channel. They reported the formation of a liquid film on the opposite side of helix axis, which was attributed to the centrifugal force effect in curved sections, and discussed forms of heat transfer in flow passages. Predicted results showed good agreement with experimental data.

2.5. Experimental techniques for vortex visualization in curved channels

Experimental results are more reliable rather than other approaches such as analytical and numerical modelling of a fluid field since no simplification is considered for them; nevertheless, even experimental approaches could include inconsistent results due to a wide range of reasons such as inappropriate initial and/or operating condition, poor data acquiring procedure, human error or other more detailed error resources. Same as other research methodologies, flow visualization techniques have been evaluated from simple pioneer idea of dyed flow (i.e. Reynolds experiment) to sophisticated contemporary optical methods competent to provide an instantaneous velocity and temperature fields with an extremely high accuracy.

To begin with, Eustice's experiment [1,2] first sparked the idea of secondary flow existence and in term of importance could be compared with Reynolds experiment. Flow visualization was carried out identically with dyed flow; however, unlike Reynolds experiment even for laminar regime of flow, streamline tracking just along tube was not sufficient enough and it had to be taken care across tube's cross section as well. Their pioneering experiment was competent enough to report some general flow characteristics such as pressure drop difference with straight channels and spiral nature of flow in coiled section which was the milestone of secondary flow investigation. Humphry et al [8] addressed one of the earliest quantitative flow assessments in curved section by use of dye traces, and laser-Doppler anemometry (LDA) technique. Their mechanical design of the bend, precluded measurements of the z component of velocity whereas it comprised a 5mW helium-neon laser, an optical unit, a light collection arrangement, an EM1 9568B photo-multiplier and a frequency-tracking demodulator (DISA 55L20). They used a digital voltmeter to read out velocity, extracted r.m.s fluctuation and proved it to be negligible for given Reynolds number. The angle between the transmitted light beams was 14.5˚ and, in combination with the forward-scatter on-line collection system, resulted in a control volume calculated to be 1.47 mm in length and 187μm in diameter: the effective dimensions were reduced by the discrimination level of the frequency-tracking demodulator. The combined effect of transit-time, gradient and noise broadening was evaluated and had negligible influence on the measured mean velocity, which had an estimated precision of around 0.5% of the bulk velocity. By comparison of experimental and numerical results reasonable quantitatively consistency was reported. LDA was also used by Enayet et al [11] to

measure mean velocity and turbulence intensity, and the corresponding Reynolds shear stress in a curved channel for Re=35200.

Sugiyama et al [12] based their study on qualitative assessment of flow to identify critical Dean number and inception of extra vortices by using photographs taken from lit air-smoke mixture in a curved rectangular duct at a certain cross section. Experiment conducted by Mori et al [19] thermistors to measure velocity and temperature in a rectangular shape curved channels with iron plates used at top and bottom sides and brass plates for curved inner and outer walls. The surface temperature of walls was measured by Cu-Co thermocouples installed to it. The temperature distribution in the channel was measured by a Cu-Co thermocouple of 0.1 mm diameter where lead wires of the thermistor and the thermocouple were in an L-shape support so that influence of measuring hole could be reduced.

Chandratilleke et al [14,29,30] published their experimental findings regarding their flow visualization in curved channels in which they vividly captured secondary flow and Dean inception with an improved precision in detection of hydrodynamic instability. Their report is one of the earliest published experimental works which visualizes the interaction between buoyancy and centrifugal forces in a heated channel and the correspondent influence on structure of vortices. They illuminated air-smoke mixture in a transparent channel at a given cross section and first illustrated main secondary and extra vortices formed due to centrifugal force and Dean instability mechanism. Then they demonstrated the effect of buoyancy force as a vertically oriented force (i.e. perpendicular to centrifugal force) and discussed effective of each body force versus heating and flow rate. The results clearly showed that by increasing flow rate secondary flow gets amplified and flow field approaches a symmetrical pattern which means negligibility of buoyancy force as compare with centrifugal force; however, in a fixed Dean number flow direction near heated wall will have a vertical inclination which is due to buoyancy force. Laser Induced Florescence (LIF) technique was applied by Fellouah et al to study laminar Newtonian [15] and non-Newtonian flow [17] in rectangular curved channel with aspect ratio of 8. They managed to capture vortex structure with reasonable quality demonstrating main secondary vortices as well as Dean vortices in various angular positions throughout a 180˚ curved section for a wide range of Dean number. Though their results showed good agreement with

numerical simulation, it was still a qualitative assessment and the optical method did not include any quantitative report of vector domain.

2.6. Summary

According to reviewed literature some decisive shortfalls are recognised and research is based on that. As a result of common limitation in numerical modelling and computational resources, lack of a reliable CFD model which could be used for instability analysis is evident. Accuracy of such a model should be more than demanded accuracy for instability threshold value. Additionally, the detection of Dean instability inception remains unreturned, since most of suggested approaches are valid just for certain conditions. Novel and comprehensive criterion is to be developed in order to detect onset of Dean instability regardless of flow conditions or geometry.

Shortfalls in numerical modelling is more evident in multi-phase fields as complicated phase and flow pattern should be specially taken care. On top of numerical modelling and validity concerns, investigation of hydrodynamic and thermal behaviour of multi-phase fields in curved channels consists of extra unattended phenomena associated with heat, mass and momentum transfer between phases.

Among few immiscible fluid flow studies in curved channel, there is no report on vortices structure and momentum exchange between phases. Effect of phase interaction on secondary flow and Dean instability due to momentum transfer through phases and thermal behaviours of such fields are yet to be discussed.

Limited studies have been published reporting unique behaviour of flow boiling in curved channels. However, substantial variation of boiling heat transfer in curved channels and details of heat partitioning mechanism are unattended yet. Although flow boiling heat transfer in curved channels could be enhanced in a very beneficial way, as a result of inadequate knowledge of phase behaviour and heat partitioning there is no report suggesting any thermal optimization approach.

CHAPTER 3

Modelling Methodology

3.1. Governing equations of fluid flow and heat transfer

The most fundamental parameters which define any behaviours of flow and heat transfer in a fluid medium are velocity, pressure and temperature. Mathematical statement of flow and heat transfer is expression of conservation laws, in term of these crucial parameters and their time and space derivation which primarily provide the fundamental insight of the flow field [56]. The fluid is considered as a continuum domain and equations are to be valid for macroscopic length (micro and larger) scale where molecular structure and motion could be neglected [57]. The first principle is the oldest and the simplest one which is conservation of mass or so called continuity equation. This principle simply consider variation of mass in a control volume to be directly proportional with net inlet mass [58]

$$\frac{\partial M_{cv}}{\partial t} = \sum_{inlet\_ports} \dot{m} - \sum_{outlet\_ports} \dot{m} \qquad 3.1$$

Equation.3.1equates net mass flow rate with the rate of mass variation inside control volume (cv) where M_{cv} is an instantaneously measured value. For obtaining desired form of continuity equation in term of velocity components, the control volume is assumed to be an infinitesimally small $\Delta x \Delta y \Delta z$ parallelepiped drawn around fixed location of (x, y, z). Taking as local velocity u, v, w components in x, y, z directions respectively, equation.3.1 will be converted to

$$\frac{\partial}{\partial t}(\rho \Delta x \Delta y \Delta z) = \rho u \Delta y \Delta z - [\rho u + \frac{\partial(\rho u)}{\partial x} \Delta x] \Delta y \Delta z + \rho v \Delta x \Delta z - [\rho v + \frac{\partial(\rho v)}{\partial y} \Delta y] \Delta x \Delta z + \rho w \Delta x \Delta y - [\rho w + \frac{\partial(\rho w)}{\partial z} \Delta z] \Delta x \Delta y \qquad 3.2$$

And it would be simplified to

$$\frac{\partial \rho}{\partial t} = \frac{\partial (\rho u)}{\partial x} + \frac{\partial (\rho v)}{\partial y} + \frac{\partial (\rho w)}{\partial z} \qquad 3.3$$

or

$$\frac{D\rho}{Dt} + \rho . \nabla V = 0 \qquad 3.4$$

Hence, continuity equation for and steady state, incompressible flow will be reduced to

$$\frac{\partial u}{\partial x} + \frac{\partial v}{\partial y} + \frac{\partial w}{\partial z} = 0 \qquad 3.5$$

Newton's second law states rate of momentum change for a particle in a given direction is equal to sum of forces applied to the particle along that direction. For explained differential cubic particle, forces could be classified into two categories: surface and body forces. Surface forces are from pressure and viscous tensions which specifically could be stated for a fluid particle; yet, body forces are a wide variety of forces usually are stated in form of source terms including gravity, buoyancy, centrifugal and electromagnetic forces. This law could be basically formulated as:

$$\rho \frac{DV}{Dt} = f_{body} + f_{surface} \qquad 3.6$$

To start with, by considering free body diagram of differential element in x-direction we could equate terms as [56, 57, 58]

$$\rho \frac{Du}{Dt} \Delta x \Delta y \Delta z = \sigma_{xx} \Delta y \Delta z - [\sigma_{xx} + \frac{\partial \sigma_{xx}}{\partial x} \Delta x] \Delta y \Delta z + \tau_{xy} \Delta x \Delta z - [\tau_{xx} + \frac{\partial \tau_{xy}}{\partial y} \Delta y] \Delta x \Delta z + \tau_{xz} \Delta x \Delta y - [\tau_{zx} + \frac{\partial \tau_{xz}}{\partial z} \Delta z] \Delta x \Delta y + f_{x-body} \qquad 3.7$$

Considering an incompressible flow, by simplifying and dividing all the terms into $\Delta x \Delta y \Delta z$ equation.3.7 will be reduced to

$$\rho \frac{Du}{Dt} = \frac{\partial \sigma_{xx}}{\partial x} + \frac{\partial \tau_{xy}}{\partial y} + \frac{\partial \tau_{xz}}{\partial z} + f_{x-body} \qquad 3.8$$

Then stress terms (i.e. $\sigma_{xx}, \tau_{xy}, \tau_{xz}$) should be related to the local flow field at differential element using constitutive relations as follow

$$\sigma_{xx} = -p + 2\mu \frac{\partial u}{\partial x} \qquad 3.9\ (a)$$

$$\tau_{xy} = -\mu(\frac{\partial u}{\partial y} + \frac{\partial v}{\partial x}) \qquad 3.9\ (b)$$

$$\tau_{xz} = -\mu(\frac{\partial u}{\partial z} + \frac{\partial w}{\partial x}) \qquad 3.9\ (c)$$

Replacing eauation.3.9 in equation.3.8 x-momentum equation will reform as

$$\rho\frac{Du}{Dt} = -\frac{\partial p}{\partial x} + \mu[(\frac{\partial^2 u}{\partial x^2} + \frac{\partial^2 u}{\partial y^2} + \frac{\partial^2 u}{\partial z^2}) + \frac{\partial}{\partial x}(\frac{\partial u}{\partial x} + \frac{\partial v}{\partial y} + \frac{\partial w}{\partial z}) + f_{x-body} \qquad 3.10$$

Which finally for an incompressible, steady case could be finalized as

$$u\frac{\partial u}{\partial x} + v\frac{\partial u}{\partial y} + w\frac{\partial u}{\partial z} = -\frac{1}{\rho}\frac{\partial p}{\partial x} + \frac{\mu}{\rho}\nabla^2 u + f_{x-body} \qquad 3.11\ (a)$$

And similarly momentum equation along y and z-direction would be

$$u\frac{\partial v}{\partial x} + v\frac{\partial v}{\partial y} + w\frac{\partial v}{\partial z} = -\frac{1}{\rho}\frac{\partial p}{\partial y} + \frac{\mu}{\rho}\nabla^2 v + f_{y-body} \qquad 3.11\ (b)$$

$$u\frac{\partial w}{\partial x} + v\frac{\partial w}{\partial y} + w\frac{\partial w}{\partial z} = -\frac{1}{\rho}\frac{\partial p}{\partial z} + \frac{\mu}{\rho}\nabla^2 w + f_{z-body} \qquad 3.11\ (c)$$

A thermal convection problem, moreover, needs solution of temperature distribution equation throughout fluid domain especially in vicinity close to the solid wall bathed by heat-carrying fluid stream [58]. First law of thermodynamic is utilized to derive an equation relating temperature distribution with convective and diffusive terms heat transfer. First law of Thermodynamics equates energy conservation of a differential control volume as:

The rate of energy increase in CV	=	The net heat transfer by fluid stream through CV	+	The net heat conduction

The rate of heat generation inside CV	+	The amount of work done by CV on the environment

Considering the same differential element, balancing convective and conductive heat fluxes and dissipation rate, such a statement for an incompressible steady case, could be formulated as:

$$u\frac{\partial T}{\partial x} + v\frac{\partial T}{\partial y} + w\frac{\partial T}{\partial z} = \frac{K}{\rho C_p}\nabla^2 T + \Phi + S_E \qquad 3.12$$

Where Φ is a non-negative term known as dissipation rate and presents work on fluid element due to deformation by stress terms

$$\Phi = \mu\left\{2[(\frac{\partial u}{\partial x})^2 + (\frac{\partial v}{\partial y})^2 + (\frac{\partial w}{\partial z})^2] + (\frac{\partial u}{\partial y} + \frac{\partial v}{\partial x})^2 + (\frac{\partial u}{\partial z} + \frac{\partial w}{\partial x})^2 + (\frac{\partial v}{\partial z} + \frac{\partial w}{\partial y})^2\right\} \qquad 3.13$$

S_E is energy source term which could be defined according to specific type of heat sources or sinks in a particular cases.

3.2. Specific source terms

Among different types of source terms, centrifugal and buoyancy terms should be considered as fundamental source terms in the current investigation. Centrifugal force which is the reason for unique behaviour of fluid in curved sections has to be defined according to configuration of geometry and coordinate system. Constant curvatures are defined to have a constant radius in a plane (here xz plane); accordingly, centrifugal force has no projection on the third axis (i.e. y-direction). Figure 3.1 illustrates a differential fluid element moving along a constant curvature radius of which is defined in xz plane where origin of coordinate system has been fixed on the centre of curvature.

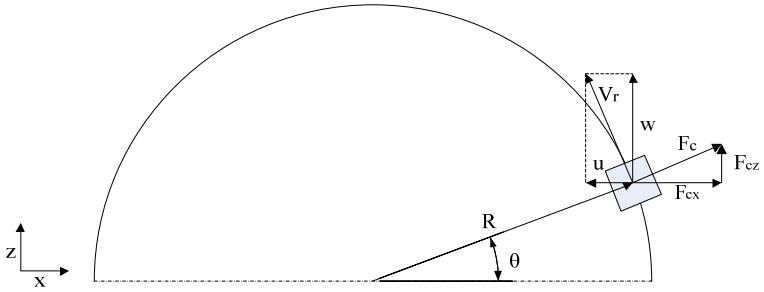

Figure 3.1. Differential element experiencing centrifugal body force in current configuration of Cartesian coordinate system

Centrifugal force, acting perpendicular to curvature, is defined for unit of volume, based on radius of curvature and tangential velocity, as

$$\vec{F}_c = \rho\frac{V_r^2}{R} = \rho\frac{u^2 + w^2}{R} \qquad 3.14$$

By replacing local value of $R, \sin\theta$ and $\cos\theta$ as $\sqrt{x^2+z^2}$, $\frac{z}{\sqrt{x^2+z^2}}$ and $\frac{x}{\sqrt{x^2+z^2}}$ respectively, components of centrifugal force in x and z direction would be as

$$F_{cx} = F_c \cos\theta = \rho.x\frac{u^2+w^2}{x^2+z^2} \qquad 3.15\ (a)$$

$$F_{cz} = F_c \sin\theta = \rho.z\frac{u^2+w^2}{x^2+z^2} \qquad 3.15\ (b)$$

It should be taken care to apply this source term just for curved section of domain (i.e. $z \geq 0$) and not for those straight inlet and outlet sections. This has been ensured by including a sign function as follow

$$F_{cx} = \rho.x.sign(z)\frac{u^2+w^2}{x^2+z^2} \qquad 3.16\ (a)$$

$$F_{cz} = \rho.z.sign(z)\frac{u^2+w^2}{x^2+z^2} \qquad 3.16\ (b)$$

Buoyancy effect should be taken into account as well since this research investigates mixed convection and interaction between centrifugal and buoyancy forces. This source term, which acts in opposite direction of gravity, is induced by density difference due to temperature gradient in flow field. The common solution which is usually utilized with reasonable accuracy is linear Boussinesq assumption. This assumption linearly relates pressure gradient along gravity direction with density difference [58, 59]. Nevertheless, this model uses a higher order of temperature dependency and defines buoyancy force as

$$\vec{F}_b = \rho(T)[g_x\hat{i} + g_y\hat{j} + g_z\hat{k}] \qquad 3.17$$

3.3. Turbulence modelling

Fundamental conservation equations of mass and momentum are solely enough to predict flow behaviour and temperature distribution for a laminar regime. However, by increasing Reynolds number they would be inadequate to model random and chaotic features of flow raised by turbulence. Reynolds Averaged Navier Stokes (RANS) turbulent models have been developed assuming mean and fluctuating component for flow velocity based on specific time and length scale proportional with eddies' scale

[60]. Among wide range of turbulence models, two-equation models, which were first introduced by Kolmogrov, are well established to have a reasonable competency for prediction of such a flow characteristics. For current investigation proper turbulence models has been designated with prospective of two concerns: first, accuracy of flow inside the field and then, competency of wall treatment procedure. $k-\varepsilon$ and $k-\omega$ closures will be represented in the following chapters where both have been applied for the specific case studies. However, turbulence modelling and its relevance to conservation equation is generally explained here.

As it is mentioned, for a turbulent flow velocity has mean and fluctuating value defined as $u = U + u'$, $v = V + v'$ and $w = W + w'$whereas similarly pressure would be defined as $p = P + p'$. On ground of that turbulence kinetic energy could be formulated as

$$k = \frac{1}{2}(u'^2 + v'^2 + w'^2) \qquad 3.18$$

and it would be related to turbulence intensity using reference velocity as

$$I_T = \frac{(\frac{3}{2}k)^{1/2}}{U_{ref}} \qquad 3.19$$

Utilizing new obtained velocity and pressure terms into equation.3.11 and 3.12, they would reformed into

$$U\frac{\partial U}{\partial x} + V\frac{\partial U}{\partial y} + W\frac{\partial U}{\partial z} = -\frac{1}{\rho}\frac{\partial P}{\partial x} + \frac{\mu}{\rho}\nabla^2 U - [\frac{\partial \overline{u'^2}}{\partial x} + \frac{\partial \overline{u'v'}}{\partial y} + \frac{\partial \overline{u'w'}}{\partial z}] + f_{x-body} \qquad 3.20\ (a)$$

$$U\frac{\partial V}{\partial x} + V\frac{\partial V}{\partial y} + W\frac{\partial V}{\partial z} = -\frac{1}{\rho}\frac{\partial P}{\partial y} + \frac{\mu}{\rho}\nabla^2 V - [\frac{\partial \overline{u'v'}}{\partial x} + \frac{\partial \overline{v'^2}}{\partial y} + \frac{\partial \overline{v'w'}}{\partial z}] + f_{y-body} \qquad 3.20\ (b)$$

$$U\frac{\partial W}{\partial x} + V\frac{\partial W}{\partial y} + W\frac{\partial W}{\partial z} = -\frac{1}{\rho}\frac{\partial P}{\partial z} + \frac{\mu}{\rho}\nabla^2 W - [\frac{\partial \overline{u'w'}}{\partial x} + \frac{\partial \overline{v'w'}}{\partial y} + \frac{\partial \overline{w'^2}}{\partial z}] + f_{z-body} \qquad 3.20\ (c)$$

and

$$U\frac{\partial T}{\partial x} + V\frac{\partial T}{\partial y} + W\frac{\partial T}{\partial z} = -+\frac{K}{\rho C_p}\nabla^2 T - [\frac{\partial \overline{u'T}}{\partial x} + \frac{\partial \overline{v'T}}{\partial y} + \frac{\partial \overline{w'T}}{\partial z}] + \Phi + S_E \qquad 3.21$$

For more clarity Reynolds stress terms have been presented in term of fluctuating velocities; however, these tensor notation of these terms is written as

$$\tau_{ij} = -\rho\overline{u_i u_j} = \mu_t\left(\frac{\partial U_i}{\partial x_j} + \frac{\partial U_j}{\partial x_i}\right) \qquad 3.22$$

This stress terms which are key parameter for coupling turbulence and conservation equations is defined according to applied turbulence model. Turbulence viscosity by $k-\omega$ model is defined as:

$$\mu_t = \frac{\rho k}{\tilde{\omega}}\ , \qquad \tilde{\omega} = \max\left\{\omega, C_{\lim}\sqrt{\frac{2S_{ij}S_{ij}}{\beta^*}}\right\}\ , \qquad C_{\lim} = \frac{7}{8} \qquad 3.23$$

where

$$S_{ij} = \frac{1}{2}\left(\frac{\partial U_i}{\partial x_j} + \frac{\partial U_j}{\partial x_i}\right) \qquad 3.24$$

This key parameter is defined by $k-\varepsilon$ model as

$$\mu_t = 0.0845\rho\frac{k^2}{\varepsilon} \qquad 3.25$$

3.4. Finite volume and Discretisation

Conservation equation for momentum, energy and turbulence are a set of partial differential equation known as transport equation are to be numerically solved by of so called Finite Volume method. This method which has been widely applied and approved in for CFD method is quite well established; however, it should be taken into account that crucial sub-procedure (e.g. discretisation, pressure-velocity coupling, pressure correction) should be specifically set for each case. It basically takes advantage of integrating transport equation over a differential control volume and then uses an integral conversion to obtain the integral in surface form of that. Regardless of pressure gradient term, effectiveness of which will later be taken into account by velocity-pressure coupling formulation, a general form of a diffusive-convective transport equation for general property of φ, where Γ is diffusion coefficient and S_φ is property source term, would be as

$$\nabla(\rho U\varphi) = \nabla^2(\Gamma\varphi) + S_\varphi \qquad 3.26$$

which could be integrated over a control volume and then converted to a surface integral over surfaces of given volume as

$$\int_{CV} \nabla(\rho U\varphi)dV = \int_{CV} \nabla^2(\Gamma\varphi)dV + \int_{CV} S_\varphi dV \qquad 3.27\ (a)$$

$$\oint_A n.(\rho U\varphi)dA = \oint_A n.\nabla(\Gamma\varphi)dA + \int_{CV} S_\varphi dV \qquad 3.27\ (b)$$

Assuming a point of P at the centre of cubic differential control volume, known as cell, which is neighboured with six other cells having centre points of E, W, S, N, T and B respectively, representing west, east, south, north, top and bottom side of P, equation.3.27-b could be rewritten in form of

$$\begin{aligned}&(\rho u\varphi A)_e - (\rho u\varphi A)_w + (\rho v\varphi A)_n - (\rho v\varphi A)_s + (\rho w\varphi A)_t - (\rho w\varphi A)_b = \\ &\left[\Gamma_e A_e\left(\frac{\partial\varphi}{\partial x}\right)_e - \Gamma_W A_W\left(\frac{\partial\varphi}{\partial x}\right)_w\right] + \left[\Gamma_n A_n\left(\frac{\partial\varphi}{\partial x}\right)_n - \Gamma_s A_s\left(\frac{\partial\varphi}{\partial x}\right)_s\right] + \\ &\left[\Gamma_t A_t\left(\frac{\partial\varphi}{\partial x}\right)_t - \Gamma_t A_t\left(\frac{\partial\varphi}{\partial x}\right)_b\right] + \bar{S}_\varphi \Delta V\end{aligned} \qquad 3.28$$

Using neighbour cell values, gradient value are to be obtained and as the length scale is assumed to be fine enough, it would be a consistent to assume linear variation for given property φ respect to differential length and replace cell gradient values as:

$$\begin{aligned}&(\rho u\varphi A)_e - (\rho u\varphi A)_w + (\rho v\varphi A)_n - (\rho v\varphi A)_s + (\rho w\varphi A)_t - (\rho w\varphi A)_t = \\ &\left[\Gamma_e A_e\left(\frac{\varphi_E - \varphi_p}{\delta x_{EP}}\right) - \Gamma_W A_W\left(\frac{\varphi_P - \varphi_W}{\delta x_{PW}}\right)\right] + \left[\Gamma_n A_n\left(\frac{\varphi_n - \varphi_p}{\delta y_{NP}}\right) - \Gamma_s A_s\left(\frac{\varphi_P - \varphi_S}{\delta y_{PS}}\right)\right] + \\ &\left[\Gamma_t A_t\left(\frac{\varphi_T - \varphi_P}{\delta z_{TP}}\right) - \Gamma_t A_t\left(\frac{\varphi_P - \varphi_B}{\delta z_{PB}}\right)_t\right] + \bar{S}_\varphi \Delta V\end{aligned} \qquad 3.29$$

Face values for convective term should be interpolated using neighbour cells values. This procedure which is known as discretisation could be carried out using various formulations such as central, upwind, hybrid and quick. Each method is assessed by fundamental criteria of Conservativeness, Boundedness and Transportiveness, well explained in literature. Upwind scheme has been chosen as an optimum method for discretization as it is preferred, as compared to central scheme, for prediction of flow direction where strong convection is involved [57]. Upwind differencing method (also called “donor cell differencing scheme”) takes the direction of flow into account when estimating value at cell face: the convective value ($\rho u\varphi$) at cell face will be assumed to be equal with upstream node value. Based on explained coordinate system (i.e. x-

positive East to West, y-positive South to North, z-positive Bottom to Top) Table.3.1 shows application upwind scheme for derivation of convective terms

Table 3.1. Application of upwind scheme for derivation of convective terms

	$(\rho u\varphi)_e$	$(\rho u\varphi)_w$		$(\rho v\varphi)_s$	$(\rho v\varphi)_n$		$(\rho w\varphi)_b$	$(\rho w\varphi)_t$
$u \geq 0$	$(\rho u\varphi)_E$	$(\rho u\varphi)_P$	$v \geq 0$	$(\rho v\varphi)_S$	$(\rho v\varphi)_P$	$w \geq 0$	$(\rho w\varphi)_B$	$(\rho w\varphi)_P$
$u < 0$	$(\rho u\varphi)_p$	$(\rho u\varphi)_W$	$v < 0$	$(\rho v\varphi)_P$	$(\rho v\varphi)_N$	$w < 0$	$(\rho w\varphi)_P$	$(\rho w\varphi)_T$

In spite of good stability and consistency with transportiveness requirements for highly convective field, such a formulation occasionally causes numerical error known as "False diffusion". Preventing such a problem and improving interpolation accuracy, second order of upwind discritization could be utilized by which more neighbour nodes will be involved and a wider influence will be taken into account (as it has been applied for current study). Having the equation sorted according to φ_P ,it would be possible to use either explicit or implicit to solve the equation which will be a numerical policy based on physics of problem, type of coupling and etc. However, for steady state problem explicit approach is usually competent and fast enough and is recommended. Second order upwind is preferred discretisation in most cases in this study and so is explained briefly; nevertheless, in some cases (specially for the purpose of multi-phase modelling) other schemes have been used which will be just pointed in the relevant parts.

3.5. Pressure-velocity Coupling, pressure correction and residual

Since generalized form of transport equation does not include pressure gradient term which is a crucial term of momentum equation, direct solution of this form of equation cannot obtain correct velocity field. Among different available algorithm, SIMPLE (Semi-Implicit Method for Pressure Linked Equations) has been chosen for single phase simulation where it basically uses a staggered grid which has different nodes for scalar and velocity values. Using initial guess fields (i.e. u^*, v^*, w^*, p^*) and finite volume formulation, uncorrected velocities (u', v', w') would be first obtained. Then, so called

pressure correction equation will be solved to obtain p' where pressure interpolation would be necessary to discretise such equation. Finally by the key approximation of SIMPLE algorithm, corrected pressure is used to obtain corrected velocities and this iterative procedure would be continued until convergence achievement.

In presence of large body forces and strongly swirling, it is necessary either to pack the mesh in regions of high gradient to resolve the pressure variation adequately or to use alternative interpolation scheme such as body force weighted which has been utilized here. The body-force-weighted scheme computes the face pressure by assuming that the normal gradient of the difference between pressure and body forces is constant.

There are different policies as convergence criteria such as classic absolute and relative error approach which explicitly compares results from current iteration with the previous one and on such basis judges about convergence. Applied solver, however, uses another method based on computed residual term for transport equation and could be utilized both globally and locally. "Globally scaled" residual term for applied solver is defined as:

$$R^{\phi} = \frac{\sum_{n=1}^{Cells} \left| \sum_{nb} a_{nb}\phi_{nb} + b - a_p\phi_p \right|}{\sum_{n=1}^{Cells} a_p\phi_p} \qquad 3.30$$

where "p" and "nb" subscripts represent centre and neighbour cell values and coefficients. This residual could also be defined "locally scaled" as:

$$R_{\phi} = \frac{\sqrt{\frac{1}{n}\sum_{n=1}^{Cells} \left| \frac{\sum_{nb} a_{nb}\phi_{nb} + b - a_p\phi_p}{a_p} \right|}}{(\phi_{\max} - \phi_{\min})_{domain}} \qquad 3.31$$

Moreover, consistency of mass transfer between inlet and outlet is monitored for all cases as well as some other local monitoring if required which will be discussed in relevant part.

3.6. Grid generation

The analysis focuses on the curved duct that is designated by 0^o at inlet to 180^o at outlet. The coordinate system used, origin of which is pegged at centre of curvature where the whole curved section is located at positive side of z-axis and the key geometrical parameters, duct height, width and radius of curvature considered in the study. For the purpose of parameter analysis, the wide of cross section is kept constant; aspect and curvature ratio will be adjusted by variation of height of cross section and radius of curvature respectively. Assessment of shape of cross section consists of a comparison between elliptical and rectangular cross section for which geometry with elliptical cross section and variable aspect ratio is examined. The general geometry characteristics of elliptical geometry are the same as rectangular and aspect ratio is defined as ratio of vertical to horizontal diameter of cross section for elliptical cross section.

Straight section at the inlet has a constant length; however, for different flow rates different length is required to obtain fully developed velocity profile at the inlet. Solving this problem (if required), momentum equations would be solved for separated straight section and the resulted outlet profile will be applied at the inlet. The extra length of which is calculated according to experimental correlation introduced by Muchnik et al [61] as follow:

$$L_{dev} \geq \begin{cases} 0.09\,\mathrm{Re}.D_h & Ar = 2 \\ 0.07\,\mathrm{Re}.D_h & A2 = 4 \\ 0.035\,\mathrm{Re}.D_h & Ar = 10 \end{cases} \qquad 3.32$$

Grid generation is a crucial procedure and has to be optimized both qualitatively and quantitatively in order to obtain reliable results. Increasing mesh size (i.e. decreasing grid number) results with accuracy reduction since all the discretised equations are differential equation which have been simplified with algebraic estimation. In contrast, mesh size cannot be refined without limitation as it severely influences computational effort. Not only the mesh size but also distribution of nodes will be important to have fine enough and consistence mesh size throughout the generated grid. Policy which has been taken in this study, consist of cross sectional grid generation and then sweeping such, by having sufficient number of grid along curvature (i.e. regeneration cross sectional grid for number of layers). Grid sensitivity study will extensively be discussed in following chapter; however, the qualitative description of grid especially in cross sectional view and crucial parameter will be briefly introduced here. Five specific

concerns in case of curved channel have to be taken into account for proper grid generation:

- Adequate number of grid is required in all three-dimensions (i.e. horizontal, vertical and axial direction) which could be obtained through grid sensitivity analysis.
- For both rectangular and elliptical cross sections structure mesh is preferred in order to reduce effect of False-diffusion and reducing computational effort. Achieving such a requirement the elliptical cross sections should be meshed as a multi-zone plane which will be explained in details in following sections.
- For single-phase instability analysis pressure-gradient should be grid independent on the outer wall; for such a purpose mesh should be compacted toward outer wall.
- For multi-phase instability analysis due to relocation of different phases next to inner and outer walls, mesh should be compacted toward both inner wall and outer wall.
- For turbulent cases, the mesh should be refined in order to obtain consistence y^+ value obeying requirement of model and solver (i.e. $y^+ \leq 5$ for $k-\omega$ model and $30 \leq y^+ \leq 300$ for $k-\varepsilon$ model)

Figure 3.2. illustrates samples of mesh in cross sectional and axial views obeying explained confinements. As an example, Figure 3.2 (a) is depicting a grid which could be used for investigation of Dean instability in single phase domain; however, for two-phase investigation as it was mentioned grid should be compacted toward inner wall as well as outer wall which turns it to what is shown in Figure 3.2 (b). Mesh sweeping in axial direction is not so critical and nodes are distributed uniformly as a part of curved section is shown in Figure 3.2 (b); yet, number of nodes should be optimized with grid sensitivity examination.

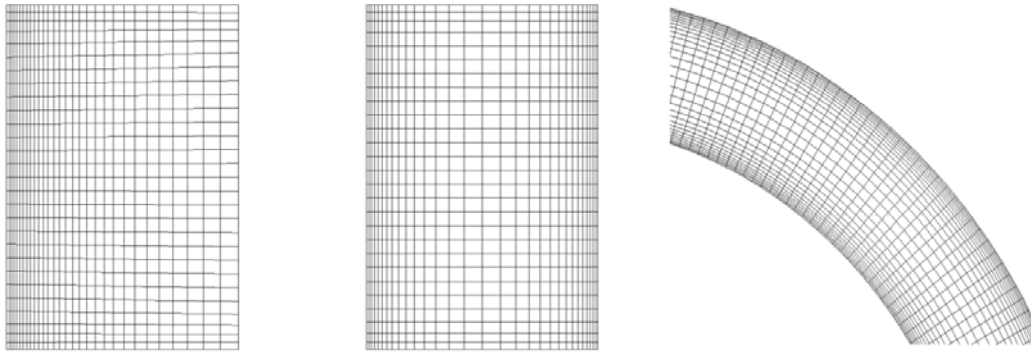

(a) Compact toward outer wall (b) Compact toward walls (c) Axial view

Figure 3.2. Samples of applied grids satisfying different flow field conditions

Once mesh is generated it will be smoothed by appropriate number of iteration using Laplace operators. In Laplace method, constraints on the components of the metric tensor of the curvilinear coordinates (i.e. physical boundaries) are used to achieve orthogonality and to control the spacing of coordinate lines [62]; however, it would affect bias defined inside domain as well and hence number of iteration should be noted.

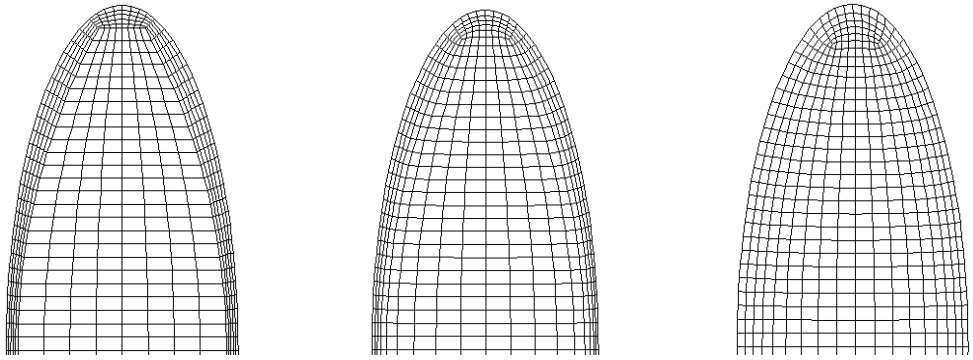

(a) before iteration (b) 50 iterations (c) 100 iterations

Figure 3.3. Application of Laplace operator for mesh smoothing

Figure 3.3 shows the effect of grid smoothing using Laplace operator in two different views. It is clearly shown that excessive number of iteration could adversely influence compaction of mesh toward walls which is a redundant effect.

3.7. Boundary conditions

Boundary condition is defined as known or assumed scalar and vector values on physical fluid's boundary, which is essential requirement to solve differential equation. Boundary conditions of differential equation could be classified into Dirichlet which

assumes constant value on the given boundary (i.e. $\varphi = cons\tan t$) or Neumann which assumes constant gradient (i.e. $\frac{\partial \varphi}{\partial x_i} = cons\tan t$). Nevertheless, it should be noted that unlike a purely mathematical problem, while these equation are used to model a physical phenomenon, boundary condition assumption should be physically valid; so that, there are a series of limitation according which boundary conditions should be applied precisely. Current model consists of three types of physical boundaries: inlet, outlet and solid wall which will be adjusted according to physics of fluid (e.g. single/multi-phase, laminar/turbulence flow) or applied numerical model (e.g. $k-\varepsilon$/ $k-\omega$ model).

a) Inlet

- Velocity inlet: this type of boundary condition which is here used for both single and multi-phase analysis, assumes velocity at inlet to be function of position. For sake of having a fully developed velocity profile, in most cases inlet velocity profile has been extracted form an inlet straight section. Other scalars including temperature (T_{in}=Constant=300 ˚K), turbulence kinetic energy (k), turbulence dissipation rate (ε) and specific dissipation rate (ω) could be defined as either constant or function of position by an input profile. For an incompressible fluid this type of boundary condition is the same as mass flow rate boundary condition.

b) Outlet

- Outflow: this type of boundary condition is used when the outlet condition is almost unknown and fields such as pressure and velocity are left to be computed by solver. It should be seriously taken care to have fairly fully developed velocity and temperature fields at the outlet while using this boundary condition. The reason for this confinement is all gradients will be assumed to be constant normal to such boundary by definition; hence, if the field is not fully developed field will introduce an error into domain from the outlet boundary. Having the outlet passage section in the geometry will guarantee a confident application of outflow boundary condition for single-phase model as a robust boundary accelerating convergence. However, due to modelling limitation and due to lack of development conditions for VOF and Mixture model at the outlet this

boundary is not the best choice there and it was replaced with a pressure-outlet boundary.

- Pressure outlet: Using this type of boundary condition fully development confinement will be eliminated and by which occurrence of back-flow will be possible. Defined pressure at the outlet will be gauge pressure. It could be used especially if the pressure drop inside the channel is known.

c) Wall

- No slip boundary condition: possibly the most common solid boundaries assumption which consider fluid velocity to be the same as solid wall velocity in adjacent of that. Accordingly flow will have zero velocity next to stationary wall.
- Isothermal boundary condition: fluid temperature is the same as solid wall in adjacent of that. This type of boundary condition has been used for both single and multi-phase models.
- Constant heat flux: temperature gradient on the solid surface in normal direction ($\left(\frac{\partial T}{\partial n}\right|_{n=0} = cons\tan t$) should be kept constant to have constant heat flux. This type of boundary condition has been used for both single and multi-phase models.
- Turbulence model near wall treatment: as it was mentioned in turbulence modelling part, estimation of fluid behaviour in sub-layer, defect-layer and log layer referred as wall treatment significantly affects investigation of parameters such as wall shear stress or pressure gradient. Generally explaining, $k-\omega$ model solves sub-layer whereas model $k-\varepsilon$ estimate it using an algebraic equation. Considering solver (i.e. FLUENT) and model requirement for current model, turbulence dimensionless distance from wall should be taken care to satisfy $y^+ < 5$ and $30 < y^+ < 300$ for $k-\omega$ and $k-\varepsilon$ respectively in order to have consistent turbulence results.

3.8. Multi-phase flow modelling

A multi-phase numerical model calculates velocity and other scalar properties of fluids and to track phase interfaces. Different multi-phase models are available which could

be used according to type of flow, limitation and requirements. The most common multi-phase models, which are available in applied commercial packages, are VOF (Volume Of Fraction), Mixture and Eulerian models each of them has competencies and limitations. VOF and Mixture models both solve a single set of transport equation for all phases whereas Eulerian model solves it for each phase separately. VOF and Eulerian method have been used respectively for immiscible flow (where just momentum is being transferred between phases) and boiling case (where mass diffusion through phase interface is additionally taken into account). As it first pointed, the most crucial challenge in multi-phase modelling is recognition of phase interfaces for which a new concept is introduced known as "volume of fraction" and represented by α. This scalar identifies volume of cell which is occupied with a given fluid. As an instant for fluid referred by "W" , volume fraction of α_W represents:

- $\alpha_W = 0$: cell is empty of given fluid
- $\alpha_W = 1$: cell is full of given fluid
- $0 < \alpha_W < 1$: cell is located on boundary of fluids and partially is filled with given flow

Referring "volume fraction" definition, it is summarized that $\sum_{p=1}^{n} \alpha_p = 1$. This statement in addition with continuity equation which takes volume fraction into account, accomplish interface tracking. Continuity equation however, is solved separately for each phase to obtain volume of fraction which is also used for calculation of material properties as well. For phase-q, continuity equation in steady form is written as:

$$\frac{1}{\rho_q}\left[\nabla.(\alpha_q \rho_q \vec{V}_q) = \sum_{p=1}^{n}(\dot{m}_{pq} - \dot{m}_{qp})\right] \qquad 3.33$$

In this equation, $\dot{m}_{pq}$ is mass transfer from phase-p to phase q and $\dot{m}_{qp}$ is mass transfer from phase-q to phase-p. By obtaining volume fraction, it would be initially possible to calculate material properties as bulk values in cells placed on the interfaces. Every scalar will be calculated according to each material properties and given volume fraction as:

$$\varphi = \sum_{p=1}^{n} \alpha_p \varphi_p \qquad 3.34$$

Properties such as density, viscosity, thermal conductivity and specific heat capacity are calculated according to such formulation and will be used in momentum and energy equation which are solved throughout domain for all the phases. This forms the simplest yet competent methodology for interface tracking and multi-phase flow analysis which is known as VOF. However, these equations are to be numerically solved by finite volume approach previously mentioned. For discritization and interpolation procedure, explained schemes (e.g. central, upwind, quick) are available for multi-phase as well; yet, interpolation on the interfaces is a specific concern which affects not only on cell values but also on shape of interface. Donor-acceptor and geometry-reconstruction method are introduced as the most sophisticated approaches for interface interpolation [63].

In cells close to phase interfaces, "donor-acceptor" scheme is used to determine the amount of fluid advected through the face where for rest of cells having volume fraction of one, standard interpolation scheme is used. This scheme identifies one cell as a donor of fluid from one phase and another (neighbor) cell as the acceptor of that same amount of fluid. The amount of fluid from one phase that can be convected across a cell boundary is limited by the minimum of two values: the filled volume in the donor cell or the free volume in the acceptor cell [64]. In this approach phase interface in each cell could be either vertical or horizontal according to direction of volume fraction gradient. Geo-reconstruction scheme is another precise interpolation method which is specifically suggested for interface interpolation in multi-phase domains. Geo-reconstruction scheme represents the interface between fluids using a piecewise-linear approach and generalized for unstructured grids assuming the interface between two fluids has a linear slope within each cell. Position of the linear interface relative to the center of each partially-filled cell is calculated, based on information about the volume fraction and its derivatives in the cell. Surface tension which is raised as a result of attractive force between molecules is another important parameter and could be related to pressure jump (i.e. pressure difference between phases) on boundaries. It is calculated based on contact angle of two phases and surface tension coefficient which could be dependent to temperature. Although surface tension has a well-established and simple formulation it should be noted that avoiding numerical instability pressure does not jump from one cell to the neighbour cells and so the phase boundary does not have a distinct recognition and depend on model is a strip or fine volume. Developing VOF model, level-set model has been recently introduced which helps to capture and track sharp interfaces

especially when immiscible flows are concerned. This formulation defines a sign function based on volume fraction values identifying each phase and uses that function to calculate curvature coefficient and consequently surface tension. The better robustness and stability has been observed using this formulation where sharp interfaces are being deformed through domain.

3.9. Convergence and stability assessment

As the formulation was discussed, residual is calculated as a cell value and is used as a criterion of convergence where as a default value is continuously being monitored during iteration procedure. However, based on the nature of problem, crucial parameters which could be used as an evidence of stability and validity may be monitored additionally. The more straightforward parameter which is necessary to be checked in multi-phase problem is net mass flow rate. Figure 3.4 shows monitoring of the mass flow rate balance and average temperature at the outlet for a multi-phase boiling case. As it is shown in Figure 3.4 (a) and 3.4 (b), although large initial discrepancy of mass flow rate balance will be lessened quickly after a few iteration, but still it could fluctuate while considering the percentage of difference in this example it is essential to keep iterating even after convergence achievement based on cell residual values.

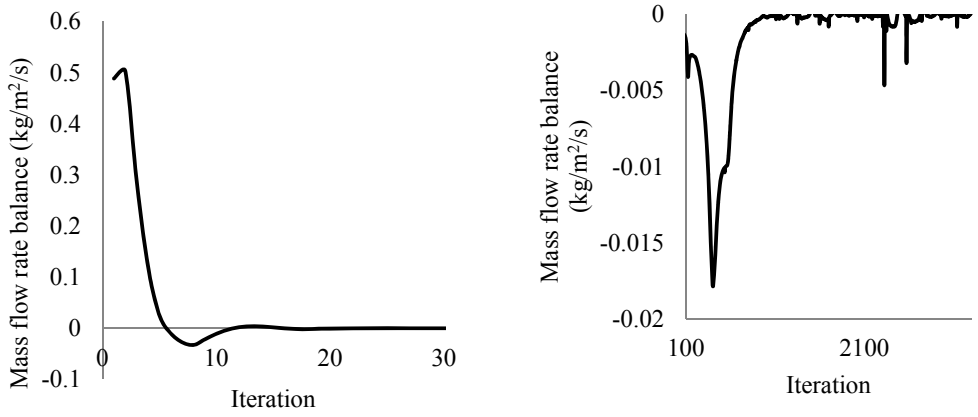

(a) Mass flow rate at initial iteration (b) Mass flow rate at late iteration

Figure 3.4. Monitoring of local values as stability and validity evidences

3.10. Summary

In this chapter general guidelines of CFD methodology, valid for all case studies in this research, have been explained. Three different numerical models will be developed, explained and utilized in following chapters on the basis of this methodology either of them has specific modelling and validation concerns. Governing equation, boundary condition configuration and validation criteria will be discussed for each model separately.

CHAPTER 4

Single-Phase Flow and Heat Transfer in Curved Channels

4.1. Scope of Chapter

Reviewing published numerical and experimental work, this chapter discusses the current knowledge-base on secondary flow in curved ducts and, identifies the deficiencies in analyses and fundamental understanding. It then presents an extensive research study capturing advanced aspects of secondary flow behaviour and associated wall heat transfer processes for both rectangular and elliptical ducts.

Overcoming current limitations, the study develops a new three-dimensional numerical model incorporating helicity approach that is validated against published data. Flow patterns and thermal characteristics are obtained for a range of duct aspect ratios, flow rates and wall heat fluxes. Results are analysed for parametric influences and construed for clearer physical understanding of the flow mechanics involved. The study formulates two analytical techniques whereby secondary vortex detection is integrated into the computational process with unprecedented accuracy and reliability. The vortex inception at flow instability is carefully examined with respect to the duct aspect ratio, duct geometry and flow rate. An entropy-based thermal optimisation technique is developed and tested for fluid flow through curved rectangular and elliptical ducts.

4.2. Introduction

The centrifugal action induced by duct curvature imparts two key effects on the fluid flow. It produces a lateral fluid movement directed from inner duct wall towards the outer wall in the axial flow, thus causing a spiralling fluid motion through the duct. This lateral fluid movement is manifested by large counter rotating pairs of vortices appearing in the duct cross section and is referred to as secondary flow. The centrifugal action also forms a radial fluid pressure gradient positively biased towards the outer

duct wall. The lateral fluid circulation takes place adversely to the radial pressure field and is dampened by the viscous effects. The combined actions of positive radial pressure gradient and viscous forces form a stagnant fluid region near the outer wall. Beyond a certain critical axial flow rate, the radial pressure gradient would exceed the equilibrium condition in the stagnant fluid region at outer wall and triggers a localised flow circulation to form additional pairs of vortices. This flow condition is known as Dean Instability [5] and the additional vortices are called Dean Vortices.

Most experimental and numerical analyses on curved ducts have been performed on rectangular duct geometries. By virtue of shape, such ducts have less wall interference on secondary vortex formation making it relatively easier for numerical modelling and convenient for experimentation including flow visualisation. Ducts with elliptical and circular cross sections have received less research attention in spite of being a common geometry used in most technological systems and, remain relatively unexplored.

Above scrutiny of published literature indicates that the available modelling methods have yet to develop for realistic representation of complex secondary flow behaviour and improved predictability for Dean Instability. Parametric influences of duct geometry and flow variables remain unexplored and poorly understood with no decisive approach for defining the onset of Dean vortices and their locations. Significantly improving these shortfalls, this chapter describes an advanced three-dimensional numerical simulation methodology based on helicity, which is congruent with the vortex motion of secondary flow. Facilitating much compliant tracking of vortex flow paths, the model uses a curvilinear mesh that is more effective in capturing the intricate details of vortices with the advantage of being applicable for both rectangular and elliptical ducts. Two intuitive approaches for detecting the onset of Dean Instability are proposed and tested in the study. An extensive parametric investigation is presented with physical interpretation of results for improved understanding of flow behaviour. A thermal optimisation scheme based on flow irreversibilities is developed and demonstrated for curved ducts.

4.3. Numerical model

4.3.1 Geometry and boundary conditions

Figure 4.1 shows the rectangular and elliptical duct geometries used for the three-dimensional simulation model in the current study. It also indicates the key geometrical parameters, duct height a, width b and the radius of curvature R. The geometrical

model consists of a semi-circular curved duct test section fitted with a straight inlet passage to ensure fully developed flow at entry to the curved duct and an outlet passage for smooth flow exit.

The analysis focuses on semi-circular curved ducts having fixed width *b* of 10 mm and constant 125 mm radius of curvature *R*. The duct aspect ratio *Ar* is changed by varying height *a*. The working fluid air is assumed to be an incompressible Newtonian fluid with temperature-dependent fluid properties. It enters at an inlet temperature of 300 K and flows steadily through the passage under laminar flow conditions. A uniform heat flux is applied on the outer wall (rectangular duct) or outer half of duct periphery (elliptical duct) while treating other walls as adiabatic. Constant velocity condition is applied to the inlet of the straight duct preceding the curved duct. The flow exit is taken to be a pressure outlet. The duct walls are assumed to have no slip boundary condition.

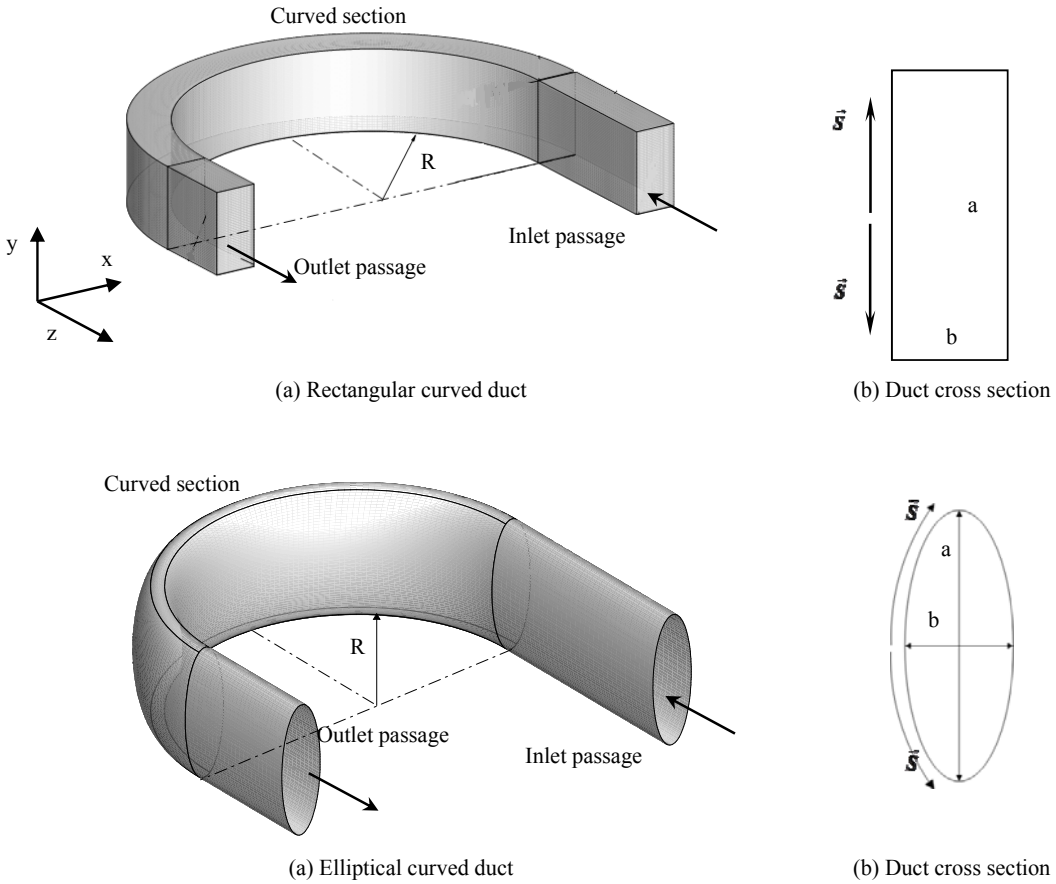

(a) Rectangular curved duct (b) Duct cross section

(a) Elliptical curved duct (b) Duct cross section

Figure 4.1. Geometry of rectangular and elliptical curved duct models

4.3.2 Governing equations

Equation should be derived for an incompressible, laminar steady flow with centrifugal force as specific momentum source term. As a result of heating and temperature gradient in the domain, buoyancy source term should be taken into account as well.

The numerical model solves the following governing equations:
Time-averaged continuity equation:

$$\nabla.(\vec{V}) = 0 \qquad 4.1$$

the momentum and energy conservation equations:

$$\vec{V}.\nabla(\rho\vec{V}) = -\nabla p + \mu\nabla^2\vec{V} + \rho_m\vec{g} + \vec{F}_c \qquad 4.2(a)$$

$$\vec{V}.\nabla(\rho c_p T) = k\nabla^2 T + S_T \qquad 4.2(b)$$

The magnitude of the centrifugal body force term in radial direction is given by,

$$F_c = \rho\frac{V_r^2}{r} = \rho\frac{(u^2 + w^2)}{\sqrt{x^2 + z^2}} \qquad 4.3$$

Considering the position and alignment of curved part of geometry, centrifugal source term in Cartesian coordinate system is obtained from,

$$\vec{F}_c = \rho\frac{1 + sign(-z)}{2}\frac{(u^2 + w^2)}{x^2 + z^2}(x\hat{i} + z\hat{k}) \qquad 4.4$$

In Equation 4, a Sign Function is used to ensure the centrifugal source term is applied only on the curved side of the geometry (i.e. $z \leq 0$). For obtaining the dimensionless parameters, the characteristics length, velocity and pressure are chosen to be D_h, U_{in}, $\frac{1}{2}\rho U_{in}^2$, respectively.

The thermally-induced buoyancy is included in the model by relating the density ρ_m in Equation. 4.2 (a) to local fluid temperature. For this, a sixth-order polynomial as given by Equation.4.5 is developed, where the given polynomial is defined according to NIST standard reference database (webBook). This order of polynomial is essential to capture behaviour of fluid at very high temperature and to achieve R-square value larger than 0.995". This approach is necessary because the linearity of the Boussinesq approximation caused some discrepancy and is found to be inadequate for evaluating the wall pressure gradient.

$$\rho(T) = 10^{-15}T^6 - 3\times10^{-12}T^5 + 3\times10^{-9}T^4 - 2\times10^{-6}T^3 + 6\times10^{-4}T^4 - 0.1008T + 9.3618 \quad 4.5$$

In capturing the helix-like fluid motion of secondary flow, this three-dimensional model incorporates a helicity function, which is defined by Equation.4.6. The helicity is non-dimensionalised using the reference helicity based on hydraulic diameter, as given by Equation.4.7.

$$H = \vec{V}.\vec{\omega} = u(\frac{\partial w}{\partial y} - \frac{\partial v}{\partial z}) + v(\frac{\partial u}{\partial z} - \frac{\partial w}{\partial x}) + w(\frac{\partial v}{\partial x} - \frac{\partial u}{\partial y}) \quad 4.6$$

$$H \approx \frac{U_{in}^2}{D_h} \Rightarrow H^* = H(\frac{D_h}{U_{in}^2}) \quad 4.7$$

For identifying the onset of Dean instability, the model proposes two separate criteria. The first criterion is based on helicity, which is computed from Equation.4.7. The second criterion uses the outer duct wall pressure gradient profile for which the non-dimensional wall pressure gradient is obtained from Equation.4.8. A sign convention is incorporated in Equation.4.8 to designate the opposite rotational directions of the vortices in upper and lower half of duct cross section, following the selection of coordinate $\vec{S}$ along the outer wall of duct cross section, as depicted in Figure 1 (b).

$$\frac{dp^*}{d\vec{S}} = \begin{cases} -\dfrac{D_h}{\frac{1}{2}\rho U^2{}_{in}}\dfrac{dp}{ds} & \text{at lower half of cross section} \\ \dfrac{D_h}{\frac{1}{2}\rho U^2{}_{in}}\dfrac{dp}{ds} & \text{at upper half of cross section} \end{cases} \quad 4.8$$

For the forced convective heat transfer in the duct, the local Nusselt Number is defined as $Nu = \frac{hD}{k}$ where the heat transfer coefficient h, is determined by considering the grid cell temperature difference between the heated wall and the adjacent fluid cell. The average Nusselt number is obtained from the surface integral, $\overline{Nu} = \frac{\int_A Nu dA}{A}$.

The model formulates a thermal optimisation scheme using flow irreversibility as a criterion. For this, the overall entropy generation split in to the components of irreversibility contributed by the wall heat transfer, including thermally-induced buoyancy effects and, that due to fluid flow friction compounded by secondary fluid motion. As such, the components of entropy generation from heat transfer (S_T) and that

from fluid friction (S_p) within the solution domain are evaluated using the expressions 4.9 (a), (b) and (c).

$$S_T = \frac{k}{T^2}\left[(\frac{\partial T}{\partial x})^2 + (\frac{\partial T}{\partial y})^2 + (\frac{\partial T}{\partial z})^2 \right] \quad 4.9(a)$$

$$S_P = \frac{\mu}{T}\Phi \quad 4.9(b)$$

where,

$$\Phi = 2\,[(\frac{\partial u}{\partial x})^2 + (\frac{\partial v}{\partial y})^2 + (\frac{\partial w}{\partial z})^2] + (\frac{\partial u}{\partial y} + \frac{\partial v}{\partial x})^2 + (\frac{\partial w}{\partial y} + \frac{\partial v}{\partial z})^2 + (\frac{\partial u}{\partial z} + \frac{\partial w}{\partial x})^2 \quad 4.9(c)$$

The entropy terms are generalised as volumetric-averaged values using,

$$S_T''' = \frac{\int S_T dv}{dv} \quad 4.10(a)$$

$$S_p''' = \frac{\int S_p dv}{dv} \quad 4.10(b)$$

$$S_g''' = S_T''' + S_p''' \quad 4.10(c)$$

Based on the above volumetric entropy generation terms, Bejan number is defined as,

$$Be = \frac{S_T'''}{S_g'''} \quad 4.11$$

Bejan Number reflects the relative domination of flow irreversibility by heat transfer with respect to the overall irreversibility [65]. In this, magnitude 1 for Bejan Number indicates totally heat transfer-dominated entropy generation while 0 refers to fluid friction causing all of flow irreversibility. Thus for curved ducts, the Bejan number performs as a visual map signifying the relative strength of thermal effects within the fluid domain interacted by the secondary flow and Dean vortices. This approach is then utilised for thermally optimising the forced convection process in ducts.

Incorporating above governing equations, a finite volume-based CFD model is formulated with the commercial package FLUENT where SIMPLE algorithm is used for pressure-velocity coupling. The momentum and energy equations are discretised by first and second order schemes, respectively. Since the model considers both buoyancy and centrifugal source terms, pressure discretisation is performed with body force-weighted approach. The stability of the solution is monitored through continuity, velocity, energy and dimensionless helicty where the convergence is achieved with values not higher than 10^{-5}. Grid independency is carefully checked paying a special attention to boundary layer modelling at the outer wall.

The simulation is performed to obtain the profiles of velocity, helicity, temperature and Bejan Number at curved duct for a range of flow rates giving Dean Number within 80 to 1600. The wall heat flux is varied up to 4000 W/m^2. The results showing some signs of Dean vortices are further refined by re-running the simulations with closer steps of K to determine the exact point of instability and the critical Dean number. This procedure is repeated for all aspect ratios, flow rates and heat fluxes. Forced convection is evaluated by the local and average Nusselt numbers at the duct wall.

4.3.3 Grid sensitivity and Model Validation

In secondary flow simulations, the solution convergence is critically dependent on the grid selection because of the intricate flow patterns and intense flow gradients. For rectangular ducts, a single-zone mesh would be adequate. However, due to the geometrical shape, elliptical ducts have much extreme flow field gradients and would require a more stringent grid arrangement.

In rectangular ducts a progressively reducing mesh is used with a much finer mesh near the outer wall where the onset of Dean Instability is anticipated. This approach has not been attempted in previous studies [13, 15, 17] wherein it was argued that a mesh size less than 1 mm would not improve accuracy, but only to increase computational time. The mesh refinement of the present analysis clearly identifies that a finer mesh near the wall is critical for detecting the onset of Dean vortices as accurately as possible. For testing grid dependency, the study uses five mesh schemes indicated in Table 1. In this, columns A, B and C represent the number of grids over duct width, height and length, respectively, while the column D indicates the progressive reduction of grid size over duct width towards the outer wall.

Table 2. Grid selection and mesh schemes for rectangular ducts

Scheme	Number of Grids			
	A	B	C	D
Mesh1	26	51	305	1
Mesh2	31	64	305	1
Mesh3	43	84	305	1
Mesh4	50	98	305	1
Mesh5	26	51	305	1.05

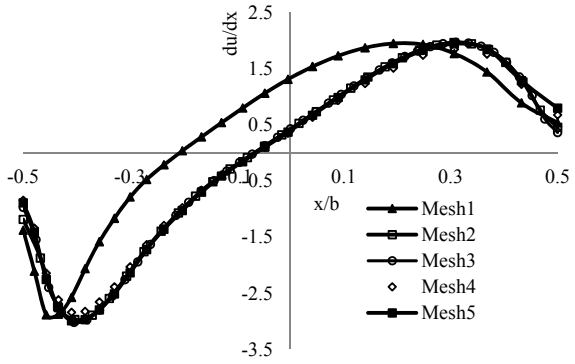

(a) Velocity derivative in x-direction at a mid-plane in cross section

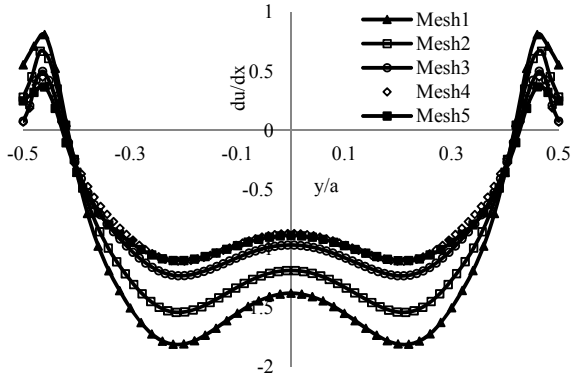

(b) Velocity derivative in y-direction at outer wall

Figure 4.2. Grid independency test for different grid schemes at curved duct exit, K=130, Ar=2

Figure 4.2 illustrates the grid dependency test through two separate variables. Figure 4.2 (a) considers the velocity derivative in x-direction at the mid-point of duct cross-section while Figure 4.2 (b) shows the velocity derivative in y-direction at outer wall. The Schemes 4 and 5 having mesh size less than 1 mm show better suitability than the other three schemes. However, the Scheme 5 is chosen as the optimum because of its slightly larger cell volume arising from progressively varied mesh size. This approach remarkably improved the vortex capturing ability in the solution domain without excessive computational demand. As such, the present study performed all computations with Scheme 5 of mesh size less than 1 mm, achieving much higher accuracy than any previous reported work.

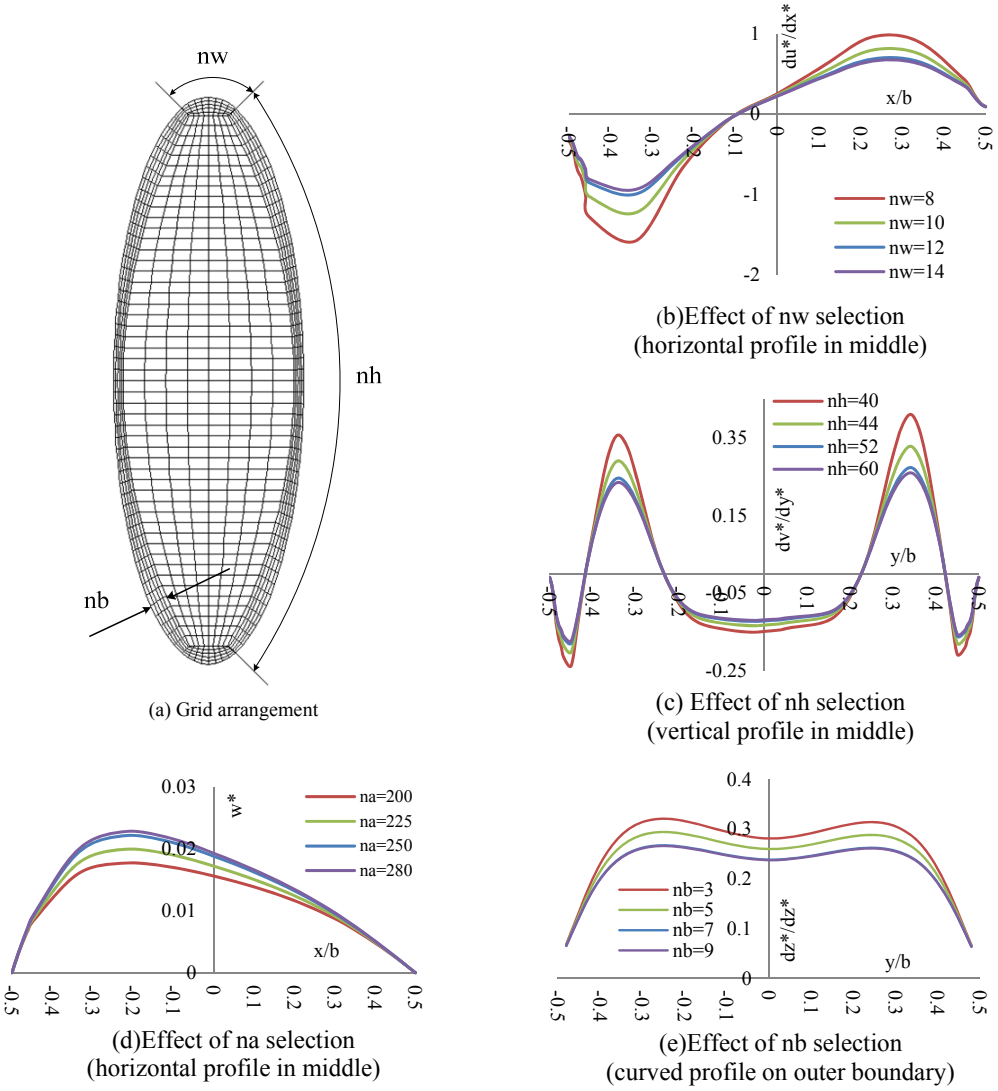

Figure 4.3. Grid arrangement and grid sensitivity analysis for elliptical duct at exit

For handling steeper flow gradients in elliptical ducts, the current analysis uses the different grid arrangement depicted in Figure 4.3. This scheme divides the elliptical duct cross section into five regions, as shown in Figure 4.3 (a) and, the rectangular cells are swept along the axial direction to obtain a fully hexagonal structured mesh. The grid distribution is determined by the parameters *nw*, *nh*, *nb* and *na*, which are respectively, the number of grids on duct width, duct height and duct periphery while *na* represents the number of layers along the axial direction. This formation ensures uniform grid residual throughout the solution domain. Figure.4.3 (b), (c) and (d) show the grid sensitivity analysis in terms of *nw*, *nh* and *nb* and *na,* where 36 permutations are considered. For elliptical duct simulation, the optimal grid selection is taken to be *nw* = 12, *nh* = 52, *nb* = 7 and *na* = 250. It should be noted that by use of Laplace

operation, previously mentioned in section 3.6, good orthogonal and aspect ratio quality is guaranteed on the border of zones.

For the purpose of validating results against published work, Figure 4.4 shows the axial flow velocity in x and y directions predicted by the current 3-dimensional model and those from the analyses of Ghia and Shokhey [10] and Fellouah et al [15], for rectangular cross section. It is seen that both magnitudes and trends of axial velocity are very favourably compared confirming the integrity of the numerical process.

Figure 4.4 also illustrates the secondary flow effect on the axial fluid velocity in the curved passage. The profile on the left (along x axis) shows a skewed peak towards the outer wall arising from the centrifugal action and is characteristically different to axial velocity distribution in straight ducts. This peak gradually spreads towards the centre with increasing flow rate because of the radial pressure build at the outer wall. The profile on the right (along y axis) shows a dip in the centre and two marginal peaks on other side. These peaks essentially correspond to the upper and lower "eye" of secondary vortices. Increased flow rate shows a marginal impact on the profile.

Similarly for an elliptical duct, Figure 4.5 provides a comparison of the axial velocity profiles at the mid cross section planes from the current study with those from Dong and Ebadian [13] and Silva et al. [26]. A very good agreement is clearly evident validating the numerical consistency of the present simulation.

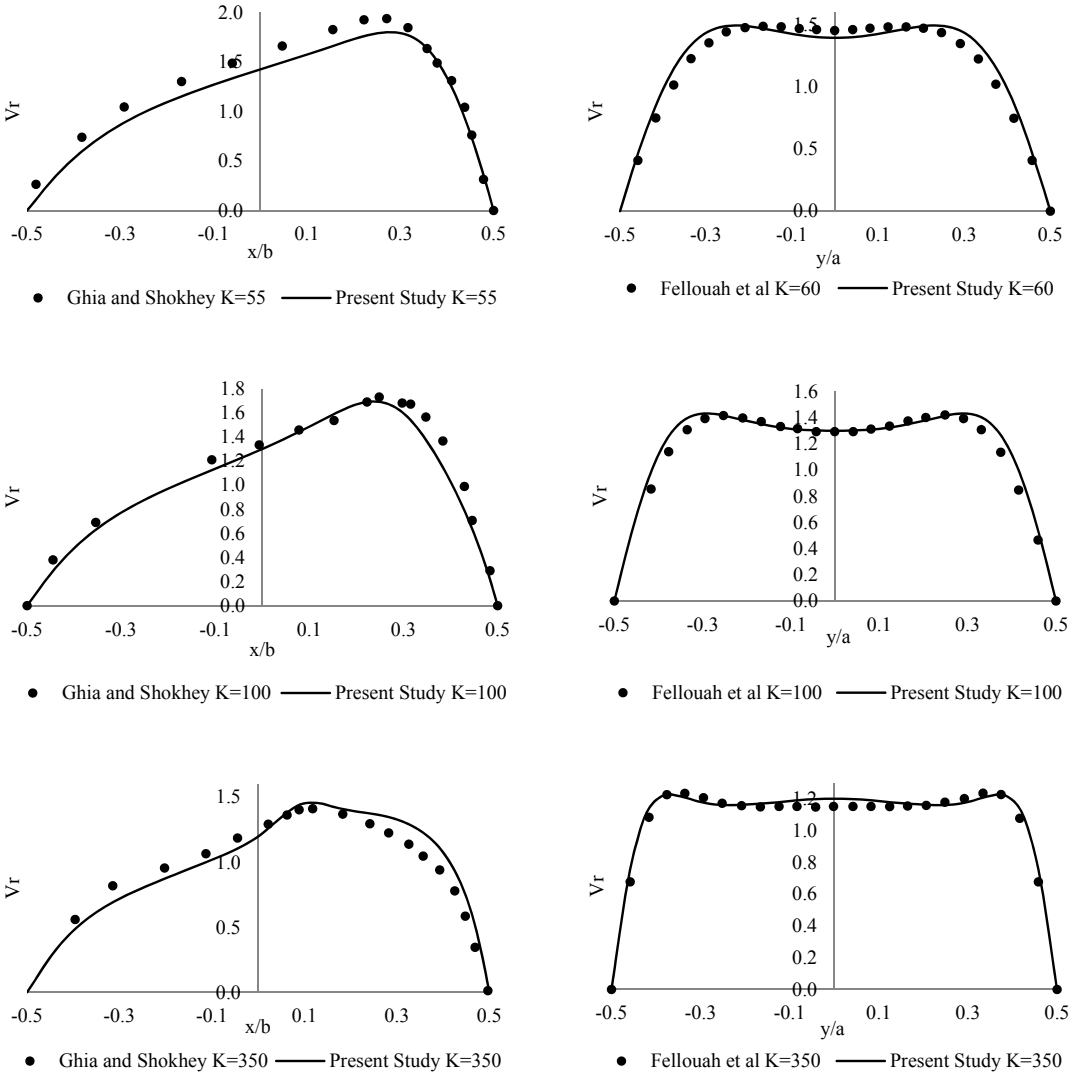

At middle plane (y = 0) along x-axis

At middle plane (x = R) along y-axis

Figure 4.4. Comparison of dimensionless axial velocity profile at curved duct exit plane (θ=180̊), Rectangular cross section, Ar=1

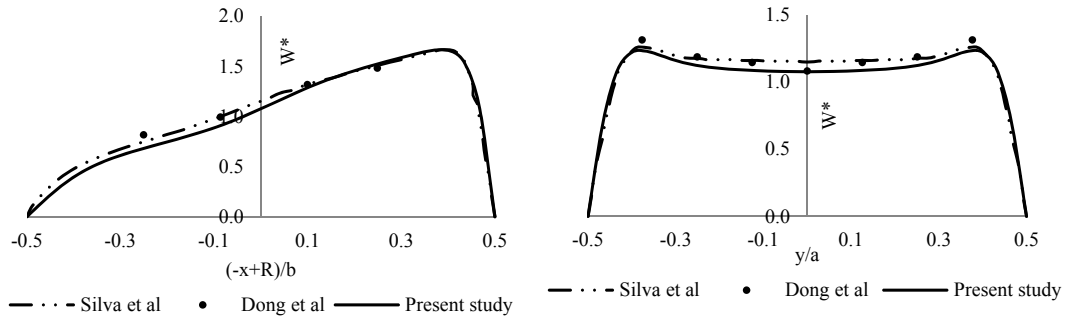

(a) At mid cross section in X-direction

(b) At mid cross section in Y- direction

Figure 4.5. Dimensionless axial velocity profile at curved duct exit
Elliptical cross section (K = 441, Ar = 1.25)

4.4. Results and Discussion

4.4.1 Fluid Flow Characteristics and Geometrical Influence

Figure 4.6 illustrates typical dimensionless helicity profiles at exit of both rectangular and elliptical ducts for several Dean numbers with no external wall heating. These patterns show unique flow features that are not present in straight ducts. Initially at low K, the flow profiles indicate two large counter-rotating vortices that are attributable to the centrifugal action from duct curvature.

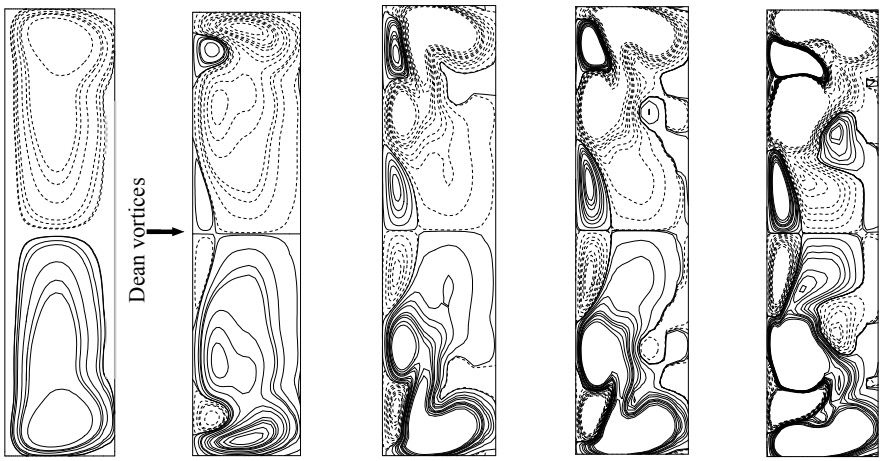

(a) K=80 (b) K=180 (c) K=260 (d) K=300 (e) K=380

Rectangular duct Ar = 4

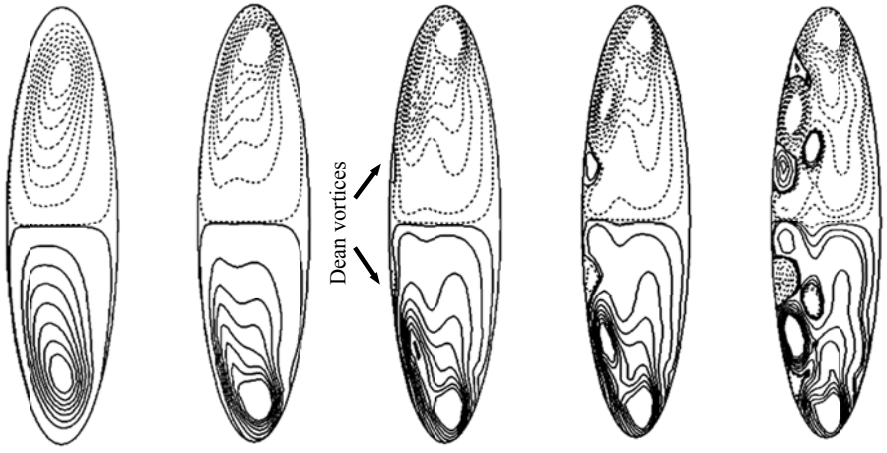

(a) K=80 (b) K=180 (c) K=260 (d) K=300 (e) K=380

Elliptical duct Ar = 4

Figure 4.6. Dimensionless helicity contours in curved ducts for varied flow rates-no wall heating (*Solid and dashed lines represent positive and Negative values respectively*)

In curved ducts, the centrifugal action is manifested as two key effects. It generates a positive radial pressure field directed towards the outer duct wall (left wall in Figure 4.6). Within this positive (adverse) pressure field, the centrifugal force drives the fluid

radially from inner to outer duct wall, hence setting up a lateral fluid circulation called secondary flow. This leads to the formation of counter-rotating vortices observed in Figure 4.6 in the duct cross section.

With increased axial flow (larger K), the secondary fluid motion becomes vigorous and the radial pressure field is intensified. Assisted by fluid viscosity, this positive pressure field acts adversely on the secondary fluid flow moving towards the outer duct wall to slow it down. Consequently near the outer duct wall, a stagnant flow region is formed and a state of fluid equilibrium is established. Above a certain critical value of K, the radial pressure field becomes far greater for fluid equilibrium within the stagnant region and a weak local fluid recirculation is triggered. This flow situation is referred to as the Dean Instability identified by the critical value of the Dean number. The local fluid circulation triggering flow instability is manifested as pairs of additional vortices called Dean Vortices. In Figure 4.6, the onset of Dean Instability occurs within K = 80 to 180 for the rectangular duct while for the Dean vortices between K = 180 to 260. These Dean vortices are designated as the helicity contour corresponding to $H^* = 0.01$. After the inception, Dean vortices gradually grow bigger with increasing K, as depicted in the figure.

It is noticed that in rectangular ducts, the Dean instability tends to occur at a lower K than in elliptical ducts of the same aspect ratio. This is because in rectangular ducts, the secondary vortex motion is less steeply deflected at the outer wall by the cross sectional geometry than in elliptical ducts allowing more freedom for fluid movement and Dean vortex formation.

4.4.2 Dean Instability and Detection of Dean vortices

In curved ducts, the appearance of Dean vortices is traditionally identified through tedious flow visualisation or by numerical trial-and-error approach. In the latter, simulations are repeatedly performed gradually narrowing down the range of K to obtain the critical Dean number and the flow patterns within a chosen tolerance limit. This involves guesswork and significant computational time. Chandratilleke et.al [14] successfully developed a criterion based on zero-potential stream function contours to identify the locations of Dean vortex generation. Whilst that approach is adequate for two-dimensional cases, it is not applicable for three-dimensional flow. The work of Fellouah et al [15] used the radial gradient of the axial velocity as a measure of identifying the flow instability. Such technique is not justifiable because the axial velocity change in radial direction is not physically connected with the secondary vortex

generation. This inadequacy is clearly reflected in the work of Fellouah et al [15], where their simulation failed to detect Dean vortices for some basic flow conditions. For example around K = 180 for a rectangular duct in the current study, Dean vortices are observed, yet the analyses of Fellouah et al [15] and Silva et al [26] did not detect vortices.

As of now, a reliable technique for identifying Dean vortices is not available in literature, particularly for three-dimensional simulations. A generalised approach is realised to be difficult because the formation characteristics of Dean vortices are influenced by strongly inter-dependant effects of duct geometry and the flow variables. In forming a process for Dean vortex detection, the present study proposes two feasible criteria that can be directly performed within the computational process.

4.4.2.1. Criterion 1 - Helicity Threshold Method

This criterion makes use of dimensionless helicity H* for tracking the onset of Dean Instability. Within the computational process, it assigns the lowest threshold value for H* at which the helicity contours are identified in the flow domain. These contours are considered Dean vortices. This selection of H* threshold essentially depends on the contour detection accuracy required, similar to defining the boundary layer thickness with a chosen velocity tolerance in traditional fluid flows.

Through exhaustive simulation runs, the current study proposes H* = ± 0.01 to be an excellent choice that warrants precise and consistent detection of Dean vortices for all cases examined. A key advantage of this technique is that the detection precision can be varied to suit the required accuracy. Also, the technique can be integrated into the computational process to perform locally in the solution domain rather than as a cumbersome post- processing method. Hence, the determination of Dean vortices is more precise and less time consuming for prompt and precise simulation results.

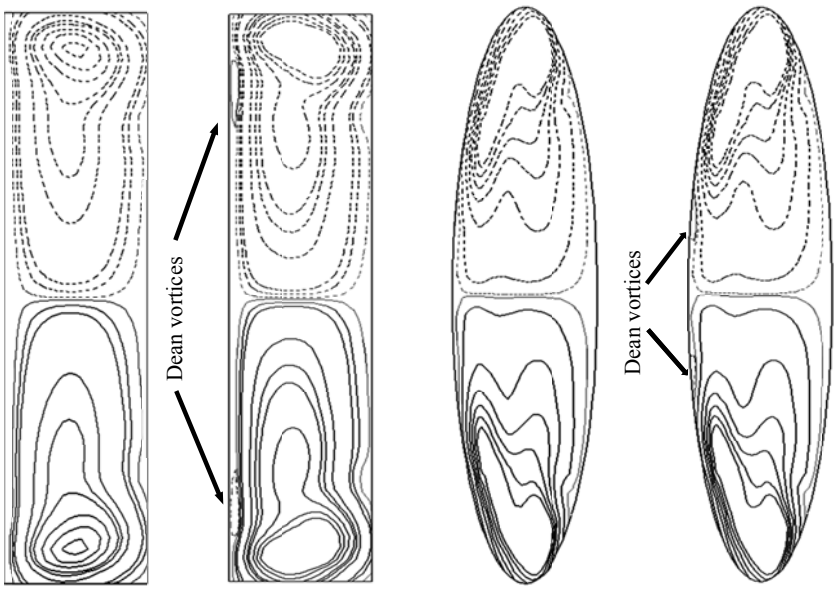

Figure 4.7. Detection of Dean vortex formation using helicity threshold method H* = ± 0.01

Figure 4.7 shows the helicity contours obtained from the helicity threshold method using H* = 0.01, just before and just after the onset of Dean vortices (indicated by arrows). For the rectangular duct, the Dean vortices are initially absent in the flow for K = 95. The helicity contours depicting Dean vortices are first detected with a slight increase in K at 102. Similarly for the elliptical duct, the appearance of Dean vortices is detectable within K = 230 to 235. By using H* < 0.01, this range can be progressively reduced to obtain more precise K for Dean Instability, as K = 100 for the rectangular duct and K =234 for the elliptical duct. However, the use of H* < 0.01 would only result in a marginal benefit towards precision, as noted above while increasing the computational demand. Therefore, H* = 0.01 is concluded to be a very appropriate threshold for detecting Dean Instability. Previous methods never provided this degree of accuracy, flexibility or ability for vortex detection, signifying that this method is far superior to any reported approach including that by Ghia and Shokhey [10] and Fellouah et al [15] using the axial velocity gradient.

4.4.2.2. Criterion 2 - Adverse Wall Pressure Gradient Method

This criterion is based on the features of the fluid pressure gradient along the outer duct wall, which is seen to have a strong affiliation with the appearance of Dean vortices. For several Dean Numbers, Figure 4.8 shows typical outer wall pressure gradient profiles evaluated from Equation.4.8 for a rectangular duct in Figure 4.8 (a) and, for

elliptical ducts in Figures 4.8 (b) and (c). The variable S is the displacement coordinate along the outer duct wall boundary, as indicated in Figure 4.1.

In Figure 4.8 (a) for low values of K, the pressure gradient remains negative over the entire outer wall. As K increases, the inflection points of the profile gradually shift to towards positive magnitude, thus creating regions of adverse pressure gradients at the outer wall. The flow contours indicate that these localities would develop flow reversal leading to Dean Instability and Dean vortices at the outer wall. At K = 139, the inflection points have just become positive, representing the onset of Dean Instability.

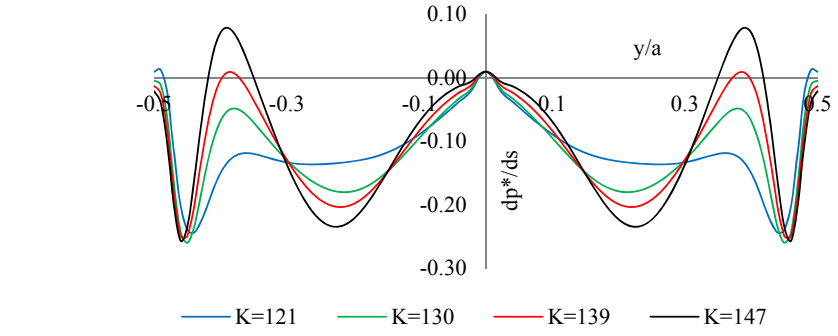

(a) Rectangular duct, Ar = 4

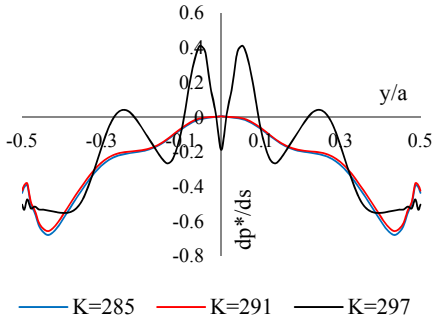

(b) Elliptical duct Ar = 3

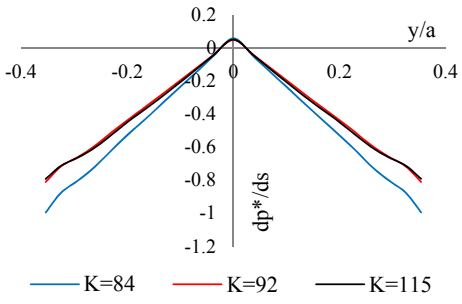

(c) Elliptical duct Ar = 1 (circular)

Figure 4.8. Pressure gradient profiles along the outer wall of curved duct

Figure 4.8 (b) depicts the outer wall pressure gradient profile for an elliptical duct of aspect ratio Ar = 3. At K = 285, the entire profile remains negative over the wall length and the predicted flow patterns in Figure 4.9 (a) do not indicate Dean vortices. At K = 291, the pressure gradient at the duct centre just changes from negative to positive and the corresponding flow pattern in Figure 4.9 (a) shows the onset of Dean vortices at the centre of outer duct wall. For K = 297, the pressure gradient profile shows distinctly positive regions that correlate to Dean vortex locations in Figure 4.9 (a).

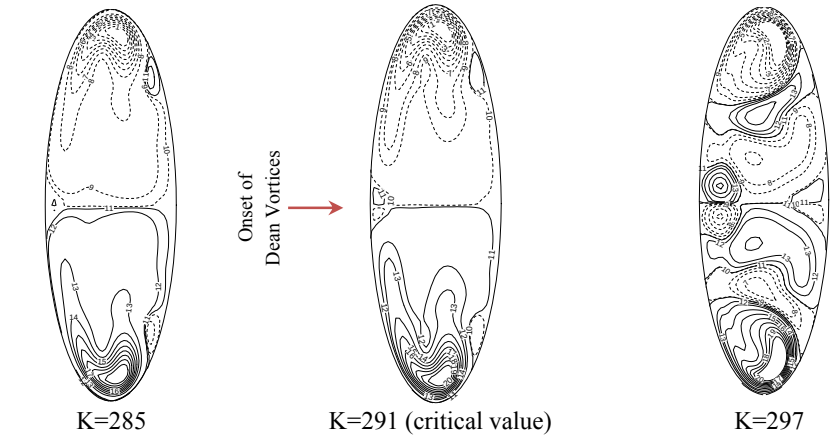

K=285 K=291 (critical value) K=297

(a) Helicty contours for elliptical duct of aspect ratio Ar = 3

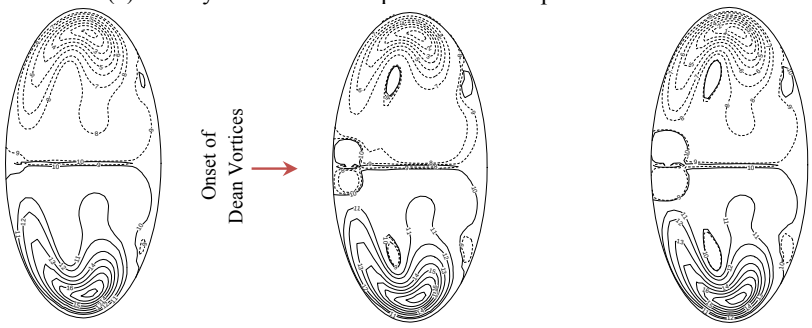

K=196 K=218 (critical value) K=229

(b) Helicty contours for elliptical duct of aspect ratio Ar = 2

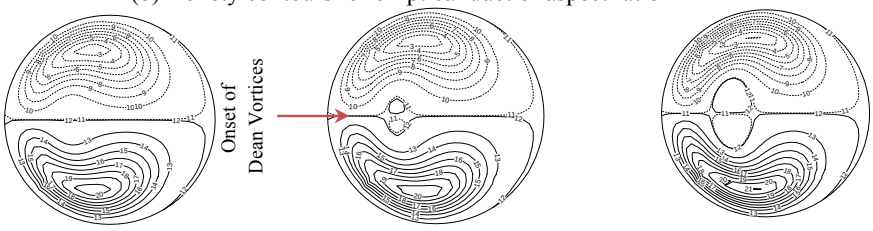

K = 84 K = 92 (critical value) K = 115

(c) Helicty contours for circular duct of aspect ratio Ar = 1

Figure 4.9. Dean vortex formation in elliptical ducts of different aspect ratios
(detected using H = 0.01)*

Above observations conclusively indicate that the adverse or positive pressure gradients at the outer duct wall could be effectively used for detecting the onset and location of Dean vortices. However, this approach has some drawback as discussed below.

Figure 4.8 (c) shows the outer wall pressure gradient for an elliptical duct of aspect ratio Ar = 1 (circular). It does not exhibit the negative-to-positive changeover in pressure gradient as with elliptical ducts having Ar > 1 shown in Figures 4.8 (a) and 4.8 (b). This means the Dean vortices are not predicted according to this criterion. Based on the helicity criterion however, Figure 4.8 (c) indeed shows the onset of Dean vortices at K =92 in the flow. This may seem a contradiction that is clarified below.

Figure 4.9 (c) helicity contours show that, for a duct with Ar = 1, the Dean vortices do not appear at the outer wall like in other duct shapes, but initiated in the centre of the flow. Therefore, the outer wall pressure gradient has lesser bearing on the Dean Instability and Dean vortex formation. As such, the pressure gradient criterion has reduced applicability for elliptical ducts with aspect ratio near unity and tends to over predict the critical Dean Number for instability. It would perform satisfactorily as aspect ratio increases where it could be seen for cases with Ar>1. Overviewing both approaches, the helicity threshold method is recognised to be precise and reliable for detecting the Dean vortices with universal applicability for curved ducts of any shape and aspect ratio.Dean vortices always form initially inside the flow domain close to the outer wall (not attached to it) at the onset of this flow condition. The exact position of these vortices depends on the duct aspect ratio and the cross sectional geometry. Figure 4.10 allows correlation of the pressure gradient and the corresponding vortex position based on helicity while outer wall is located at left side. The figurers indicates that, at low flow rates, the helicity approach identifies the appearance of Dean vortices while the pressure gradient remains negative, meaning that the latter approach does not capture this existence of vortices. Also, it is noted that Dean vortices appear not at the outer wall but in the bulk fluid away from the wall. However, with increased flow rate, Dean vortices will gradually migrate towards the outer wall wherein the pressure gradient becomes adverse (or positive) and both criteria are able to capture Dean vortices.

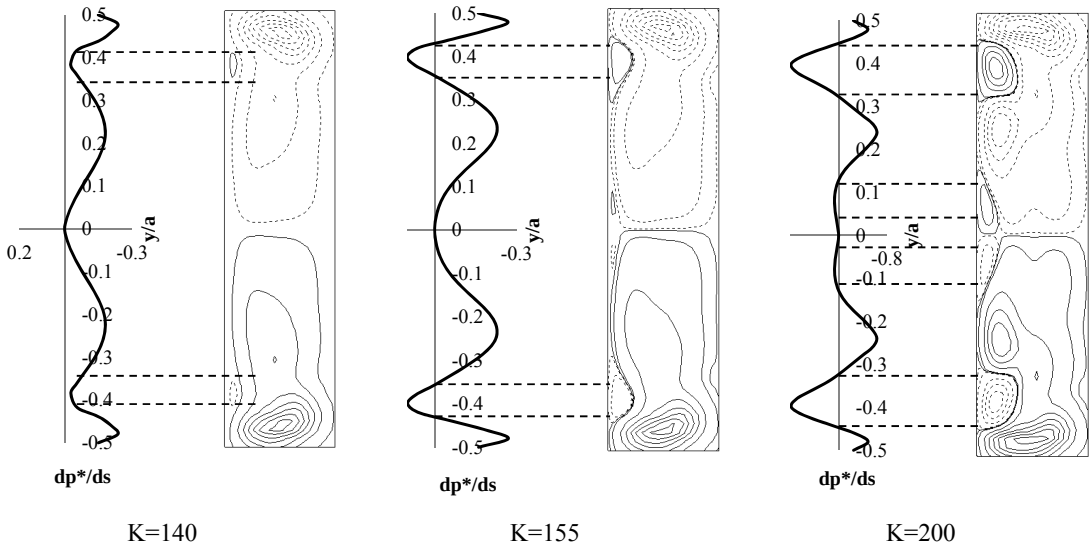

Figure 4.10. Comparison of two criteria for identifying the onset of Dean instability curved duct exit plane (θ=180̊) for different flow rates, Ar = 4

4.4.2.3. Three-dimensional vortex core representation of hydrodynamic instability

Figure 4.11 illustrates a visualisation method for hydrodynamic instability development within the curved duct from its inlet to outlet. Figure 4.11 (i) provides the view with duct inlet in the foreground while Figure 4.11 (ii) shows that with duct outlet in the foreground.

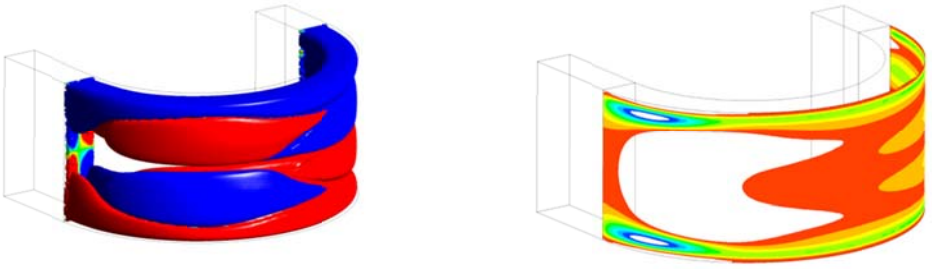

(i) Viewed from duct inlet in foreground

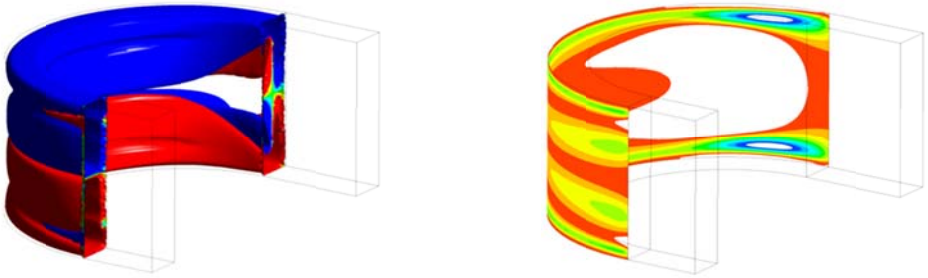

(ii) Viewed from duct outlet in foreground

(a) Vortex core within curved duct (b) Pressure gradient distribution at outer wall

Figure 4.11. Structure of secondary flow and Dean vortices at K=155, Ar=4, $\gamma = 5$

The illustration on the left depicts the iso-value envelop of helicity captured by applying the dimensionless helicity criterion with $H^*=0.01$ discussed in Section 4.4.2.1. The envelop represents the 3-dimensional vortex structures (red and blue indicate opposite vortex rotational directions) within the flow field in the curved duct and accounts for the helicity magnitude, swirling strength and vorticity. The growth sequence of secondary vortices (blue and red) is clearly visible from the inlet up to a location where the Dean vortices also appear in the flow, indicated by two smaller envelops embedded in the main iso-value surface. At the early part of the curved section, weak vortices appear at both upper and lower duct sections. These cannot be recognised as Dean vortices because the flow in this region is developing against curvature effect. With the disappearance of these initially formed vortices, the flow could be considered as fully developed. Thereafter, the extra vortices formed due to centrifugal force are regarded

as Dean vortices. This observation states the flow development concept in curved channels.

The illustration on the right depicts the contours of constant outer wall pressure gradient, discussed in Section 4.4.2.2. The profile shows the presence of adverse pressure gradient (white areas) in the vicinity of inlet. This region extends downstream up to a location where the hydrodynamic instability is triggered, where flow reversal occurs with an observed (colour) change in contour profile.

It is noted that the vortex core iso-surfaces and pressure gradient contours show a remarkable similarity in formation within the duct and identify hydrodynamic instability in conformation with each technique. This signifies the consistency and validity of both criteria as means of detecting hydrodynamic instability. However, the helicity criterion evidently predicts a lower K for instability than the adverse pressure gradient criterion. For example, from Figure 4.7 for Ar = 4, γ = 5, the dimensionless helicity criterion predicts the critical Dean number to be 100 while it is noted to be 155 by the adverse pressure gradient approach in Figure 4.8. This discrepancy arises because; the helicity criterion detects the formation of Dean vortices within the fluid as per assigned H* value while the adverse pressure gradient approach can only detect vortices when they have migrated to the outer wall, which occurs at a slightly increased flow rate (or K).

4.4.3 Effect of duct aspect ratio

Figure 4.12 illustrates the variation of the critical requirement to initiate Dean Instability with aspect ratio for both rectangular and elliptical ducts, obtained using the helicity method in the current study. For comparison, the figure also provides the critical Dean number from the experimental results of Cheng et al. [9] for rectangular ducts.

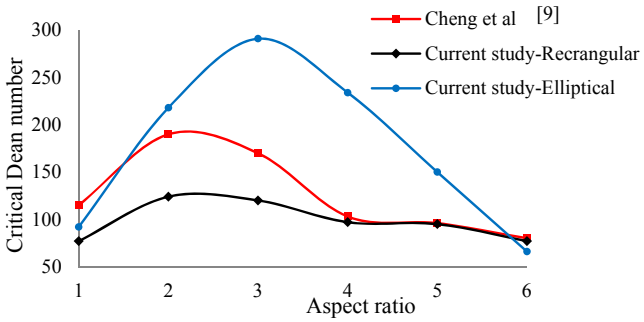

Figure 4.12. Effect of aspect ratio on critical Dean number

It is noted that the critical Dean number initially increases with the aspect ratio up to a certain value and then falls away for higher K. This trend conforms to the trend shown

in Figure 4.9 for elliptical ducts and the observations reported in previous experimental and numerical work. For rectangular ducts, the current model under-predicts the critical requirement for Dean Instability compared to the experimental results of [9]. This is because, the helicity method identifies Dean vortices much early in the growth process, whilst in experiments, the vortices are visually observed after they have grown to a detectable size at a higher Dean number.

4.4.4 Thermal characteristics and Forced convection

4.4.4.1. Effects of flow rate

The helicity contours and the fluid temperature fields in Figure 4.13 illustrate the effect of outer wall heating in rectangular and elliptical ducts for two selected values of K. The comparison of helicity contours in Figures 4.13 and 4.6 indicates the wall heating essentially sets up a convective fluid circulation that interacts with the secondary flow and significantly alters the flow characteristics. This fluid circulation is driven by the buoyancy forces resulting from thermally-induced density changes.

As evident in Figure 4.13 for K=80, at low flow rates, the convective circulation dominates the flow behaviour with less influence from secondary vortices. When the flow rate is increased, the centrifugal action intensifies and more vigorous secondary flow develops in the duct. Consequently, the secondary vortices overcome the thermal buoyancy effects to become more dominant and determine the overall fluid behaviour, as illustrated in Figure 4.13 for K=380.

Due to the confined geometry, the fluid flow within elliptical ducts is generally more constrained and tends to have steeper fluid flow gradients than in rectangular ducts. This geometrical effect is more pronounced at low flow rate when the flow patterns are dominated by thermally-induced buoyancy.

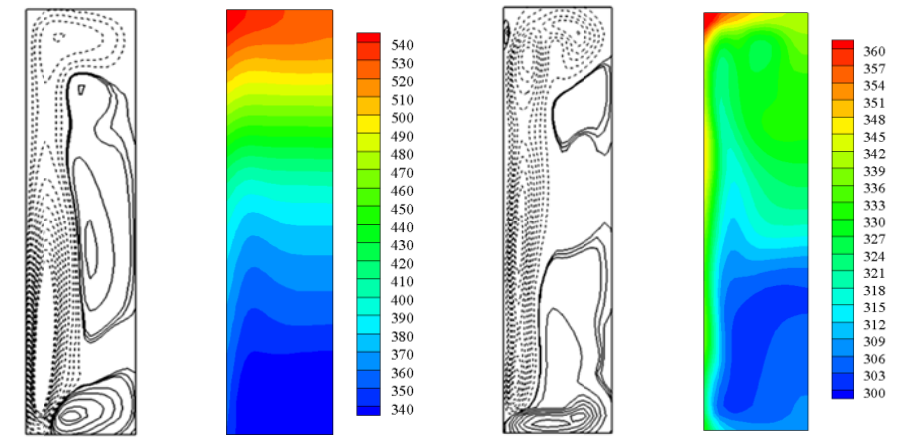

Helicity profile Temperature field K=80 Helicity profile Temperature field K=380

(a) Rectangular duct, Ar = 4

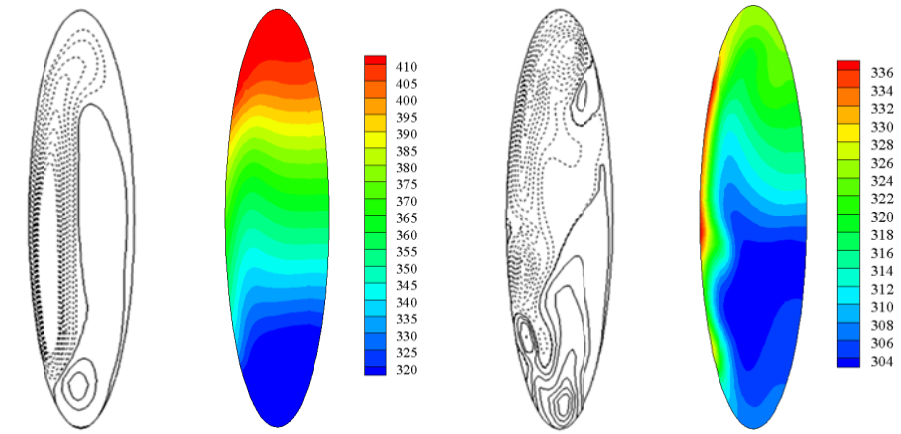

Helicity profile Temperature field K=80 Helicity profile Temperature field K=380

(b) Elliptical duct, Ar = 4

Figure 4.13. Outer wall heating effect on helicity and temperature, q = 250 W/m^2

Figure 4.13 with K=80, clearly demonstrates that the elliptical duct has sharper velocity and temperature gradients at the outer wall compared to the rectangular duct. Consequently, the elliptical duct exhibits a higher rate of forced convection than in the rectangular duct within the lower range of K in Figure 4.14.

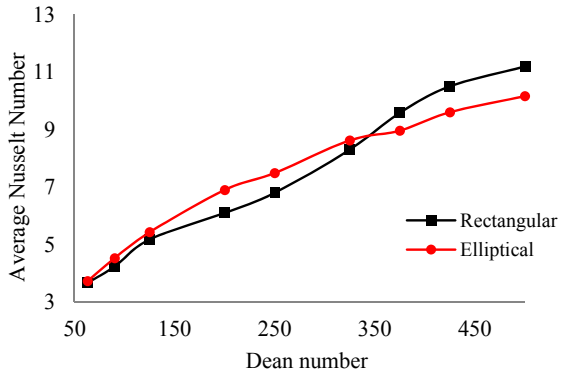

Figure 4.14. Variation of average Nusselt number at outer wall with Dean number, Ar = 4, q = 100 W/m^2

For elliptical and rectangular ducts, Figure 4.15 shows the comparison of skin friction factor, which is essentially dependent on the velocity gradient and related to the duct pressure drop. With inherently steep fluid profiles, the elliptical duct has slightly larger skin friction compared to rectangular ducts with no crossover in the entire flow range.

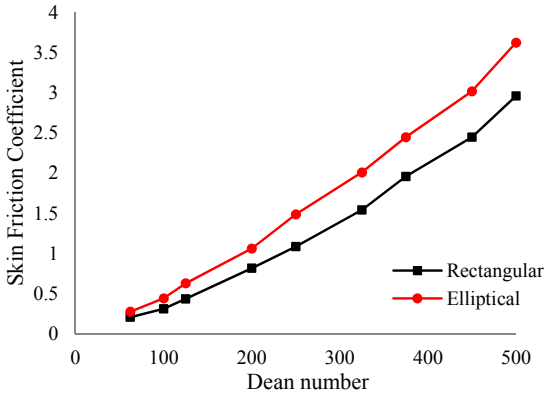

Figure 4.15. Variation of duct skin friction factor with Dean number, Ar = 4, q = 100 W/m^2

4.4.4.2. Effects of outer wall heating

Comparison of helicity contours in Figures 4.6 and 4.13 at K = 380 indicates that with outer wall heating, a tendency is developed to impede the formation process of Dean vortices in both types of ducts. This is instigated by the thermal buoyancy-driven convection that continually acts to displace the fluid layer at the outer wall, thus weakening the formation of the stagnant fluid region, where the Dean Instability would occur. Hence, the flow reversal is undermined with diminished potential for Dean vortex generation. High wall heat fluxes would impart more adversity on the triggering flow conditions of Dean Instability. In figure 4.16, these wall heating effects are clearly evident as a gradual decline in Nusselt number with increased outer wall heat flux for both types of ducts.

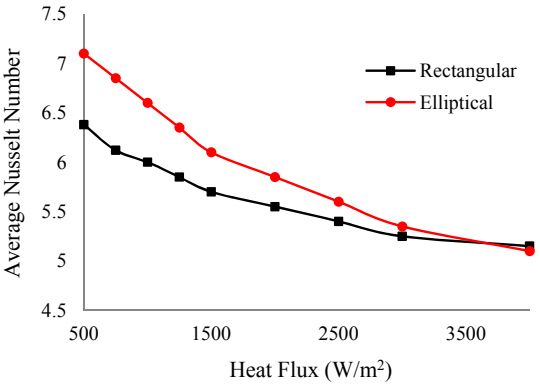

Figure 4.16. Variation of average Nusselt number at outer wall with outer wall heat flux, Ar = 4, K = 250

With high wall heat fluxes, thermally induced convective circulation becomes stronger, imparting additional resistance to the axial fluid motion. This effect is more pronounced in elliptical ducts than in rectangular ducts. Consequently, duct skin friction coefficient tends to be relatively higher for elliptical ducts while indicating some increase with the wall heat flux, as evident in Figure 4.17.

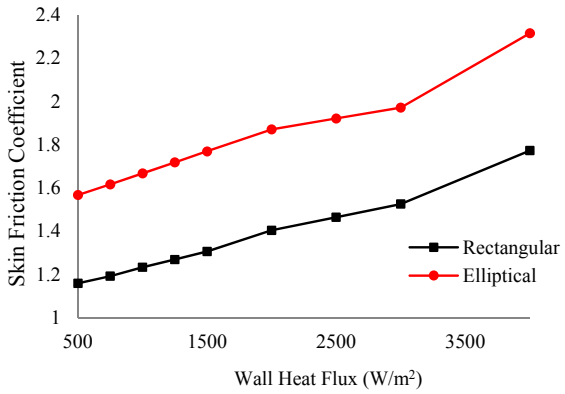

Fig. 14

Figure 4.17. Variation of average duct Skin Friction with outer wall heat flux, Ar = 4, K = 250

4.4.4.3. Thermal optimisation

Figure 4.18 shows the Bejan number (Be) distribution in curved duct cross sections. For both rectangular and elliptical ducts at lower *K*, the flow irreversibility is practically dominated by the entropy generation from wall heat transfer (Be ≈ 1 with a red cast) over the entire flow cross section. As K increases, Bejan Number contours gradually acquire magnitudes less than 1 indicated by the blue cast. This signifies that in curved ducts, the secondary flow provides favourable fluid mixing to transport the hot fluid away from the heated wall, which in turn will improve forced convection.

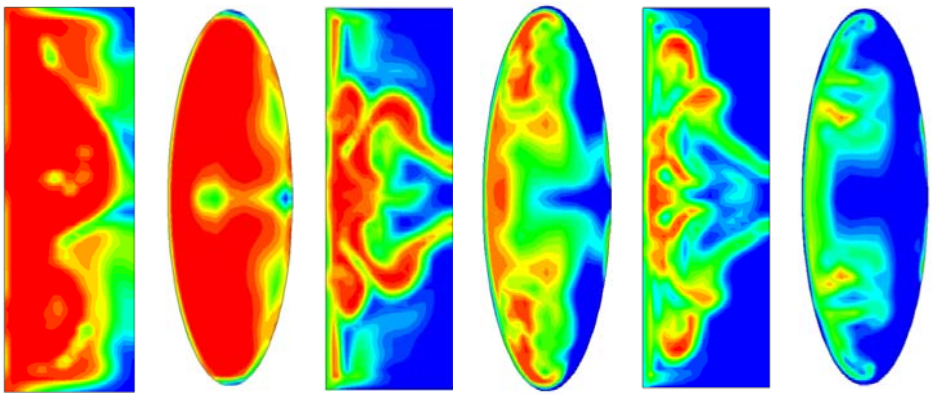

K = 400 K = 1000 K = 1600

Figure 4.18. Bejan Number contours for rectangular and elliptical curved ducts, q = 100 W/m^2

Magnitudes of Be < 1 also signifies an increased contribution to the total irreversibility from viscous effects, which would negate the overall flow benefits. These effects are less pronounced in rectangular ducts than in elliptical ducts. The opposing thermal and hydrodynamic trends identify a potentially useful technique for thermal optimisation of fluid flow through heated curved ducts, as explained below.

Figure 4.19 illustrates the variation of the flow irreversibility components St, Sp and Sg for rectangular and elliptical ducts with K, evaluated using Equation 4.9 and 4.10. It is evident from the figure that, when K is increased, St steadily falls while Sp rapidly grows. Although this falling trend is similar to both types of ducts, the thermal irreversibility component St decays more gently in elliptical duct compared to the rectangular duct. This means, the elliptical duct is less efficient in transporting heat from the wall than the rectangular duct. On the other hand, the viscous irreversibility component Sp grows more rapidly in elliptical ducts, signifying that the elliptical shape causes higher frictional pressure loses.

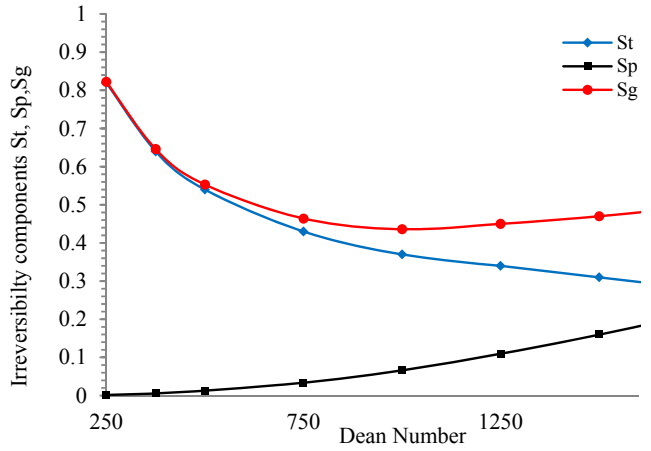

(a) Rectangular duct

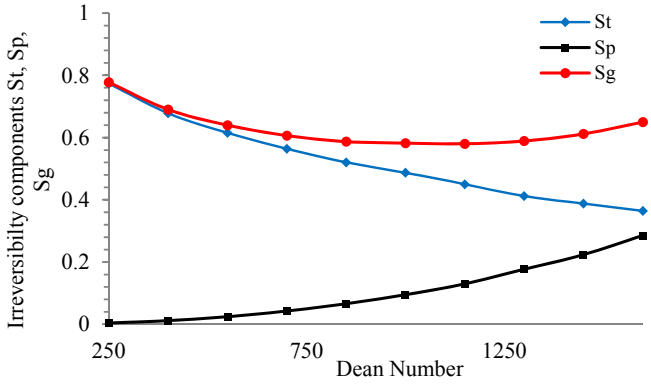

(b) Elliptical duct

Figure 4.19. Curved duct thermal optimisation using total entropy generation

The overall irreversibility Sg, which is the sum of St and Sp, is initially dominated by the thermal irreversibility component and steadily falls with K for both duct shapes. However, the falling gradient is steeper for the rectangular duct, which implies more effectiveness heat transfer in the fluid domain with lesser adversity from viscous effects.

At a certain value of K, Sg shows a minimum magnitude. This point of inflection is identified as practically the best possible "trade-off" between the highest achievable thermal benefits with the least viscous penalty for curved duct flows. It is noted that the magnitude of the lowest overall irreversibility is higher for elliptical ducts than for rectangular ducts, indicating rectangular ducts would thermally better perform.

4.5. Summary

This chapter provides a broad overview of the reported findings from the published numerical and experimental studies on fluid flow in curved duct geometries. The discussion then focusses on the latest contributions to new knowledge in this field by extensive research programmers of the authors where new analytical techniques and methodologies have been discovered, warranting a clearer fundamental understanding on fluid and thermal behaviour in curved ducts.

Improving accuracy over previous methods, the current study formulates a new three-dimensional simulation methodology based on helicity that realistically represent the secondary vortex structures in curved ducts of any shape. The model accurately identifies and predicts unique features of secondary flow and the associated forced convection in both rectangular and elliptical curved ducts. Conforming to the limited data in literature, the predicted results examine the effects of fluid flow rate, duct aspect ratio and heat flux over a wide practical range. The duct geometry and aspect ratio are found to have critical influence on the secondary flow characteristics, indicating a profound effect on Dean vortex formation, Dean Instability and forced convection. Elliptical ducts show marginally inferior thermal performance compared to rectangular ducts under identical flow conditions.

Overcoming a current analytical limitation, this part of study appraises two novel methods for detecting the onset of Dean Instability in curved ducts, confirming their technical feasibility. One such approach uses a defined helicity threshold while the other makes use of features of the outer wall pressure gradient. Both methods offer the option of being able to be integrated into and performed within a computational scheme,

for fast, reliable and accurate detection of Dean vortex formation. However, the helicity threshold method is realized to be more universally applied to all duct shapes and aspect ratios. The pressure gradient approach shows limited functionality for it over-predicts the critical Dean Number in curved ducts of aspect ratio near unity.

The study also develops a useful thermal optimization technique for heated curved duct based on the Second Law irreversibilities. It identifies the elliptical ducts to have less favourable overall thermal and hydrodynamics characteristics than rectangular ducts.

CHAPTER 5

Immiscible Two-Phase Fluid Flow in Curved Channels

5.1. Scope of Chapter

This chapter investigates the behaviour of two non-mixing fluids flowing in a heated curved channel. In simulating this immiscible fluid flow, a multi-phase model based on VOF approach is developed for steady, turbulent, incompressible fluid flow through curved channel. The analysis examines the influence of centrifugal forces arising from channel curvature on the phase distribution and flow patterns, and their impact on the thermal characteristics. Unique flow features are identified through the interactions between the fluid phases and vortex structures of the immiscible flow in curved channels. The convective heat transfer in curved channel is appraised in relation to the behaviour of fluid components and curved channel flow parameters. Finally, the chapter presents a Second Law irreversibility analysis whereby a thermal optimisation technique is developed for immiscible fluid flow through heated curved channels.

5.2. Introduction

Non-mixing multi-component fluid flows often occur in many industrial applications. Some such examples are the transportation of crude oil mixed with water in oil and gas industry, the chemical fluid flow within reactors in pharmaceutical production processes [66] and, the flow of lubricant and refrigerant mixtures in refrigeration systems [67, 68].

The flow behaviour of two-phase immiscible fluids is uniquely different to both single phase fluids and two-phase flow boiling. Such fluids exhibit unusual flow dynamics because, immiscible fluid components may have differential flow (slip) velocities and do not undergo mass exchanges albeit heat transfer may occur over phase boundaries. Thus, the flow behaviour of non-mixing fluids is critically dominated by the relative magnitudes of fluid component properties, in particular the density and viscosity. In

curved channels, the centrifugal forces arising from channel curvature affect more on the heavier of the fluid components. These combined interactions determine the distribution, deformation and interface area of phases, and the flow regimes in immiscible fluid flow. Resulting flow patterns, phase separation, pressure drop and heat transfer characteristics are uniquely different to other types of fluid flows. Consequently, for the development of industrial equipment involving non-mixing fluids, new design methodologies are necessary with a clearer fundamental understanding of immiscible flow behaviour.

Much research has been conducted on immiscible fluid mixtures flowing in straight channels. These typically examine the phase instability arising from the viscosity differences and report substantial influence on fluid and thermal characteristics [69,70]. To the contrary, immiscible fluid flow in curved channels has not much been investigated and many fundamental aspects still remain unexplored in spite of significant applications in process industries.

Multi-phase fluid flow systems are inherently chaotic and potentially unstable due to non-homogeneous fluid properties that create imbalances in flow dynamics. In curved channels, additional complexities appear because of the centrifugal action that induce secondary flow effects and create the possibility of Dean Instability in the fluid.

In single phase fluid flow through curved passages, the presence of secondary flow and Dean vortices is fundamentally linked to the interaction between fluid inertia and viscous forces. With multi-component fluid flows in curved channels, the momentum transfer across phase boundaries also play a role on secondary vortex formation, in addition to the inertia and viscous effects. This is because of the fluid phases have velocity differentials called drift velocity. Process designs ignoring these curvature effects would lead to system inefficiencies and failures such as pipe wall erosion and corrosion and, tube burn out due to non-uniform wall heat transfer.

In analysing immiscible fluid flow, two key transport mechanisms need to be considered. They are the heat and momentum transfer across the interfacial phase boundaries and the heat convection within each fluid phase [71]. Accounting for these and the curvature-induced centrifugal effects, a numerical model is developed in this chapter to investigate the flow of two non-mixing fluid through heated curved channels. The simulation examines the secondary flow circulation within each fluid phase and the

separation of phases that arise from the centrifugal action and the differential phase velocities and fluid properties. The analysis also evaluates the impact on curved channel heat transfer from the phase distribution and the secondary flow behaviour in immiscible fluid flow. In examining this flow condition, the following geometry is considered.

5.3. Geometrical Configuration and Boundary Condition

As shown in Figure 5.1, the immiscible flow simulation is performed on a semi-circular (180^o) curved duct of fixed radius of curvature, which is very similar to the geometrical arrangement used in single-phase analysis. The coordinate system and the dimensions used in the geometry are also given in the figure. The analysis examines the flow within square and circular ducts. For both duct types, a 10 mm width is chosen to permit the hydraulic diameter to be the same between them.

The analysis uses a mixture of water (heavier) and kerosene (lighter) as the immiscible working fluid, which is fed together in to the curved channel through a straight inlet passage. The length of this passage is adjusted depending on the flow rate to ensure fully-developed conditions at the curved channel entry. The flow rates of these fluid phases are independently varied. The flow within the straight section is separately analysed to obtain the fully-developed velocity component profiles, turbulence characteristics and distribution of volume fraction, that are used as input conditions for curved section. This approach significantly reduces the computational demand in analysing curved channel section for all tested flow cases.

At curved channel exit, a short passage is added to provide smooth fluid out flow. This is critically important for multi-phase flow analysis to prevent any "outlet backflow" and/or numerical disruption issues during computations. At this flow exit, pressure outlet boundary condition is applied in contrast to the outlet flow boundary condition used for single-phase flow simulation. For flow cases with wall heating, a constant heat flux within the range of 0 to 5000 $W/m^2.K$ is applied over the entire circumference of the curved passage.

The curved channel geometry is orientated to provide symmetrical influence from gravity on the flow through curved channel. With this orientation, the gravitational forces compel the heavier fluid phase (water) to move along the inner channel wall

while the centrifugal forces act to displace the heavier fluid phase towards the outer wall. Relative strength of these counteracting forces determines the phase profiles of the two fluid components, where the distribution of the heavier phase reflects the role played by the centrifugal forces in this type of flow.

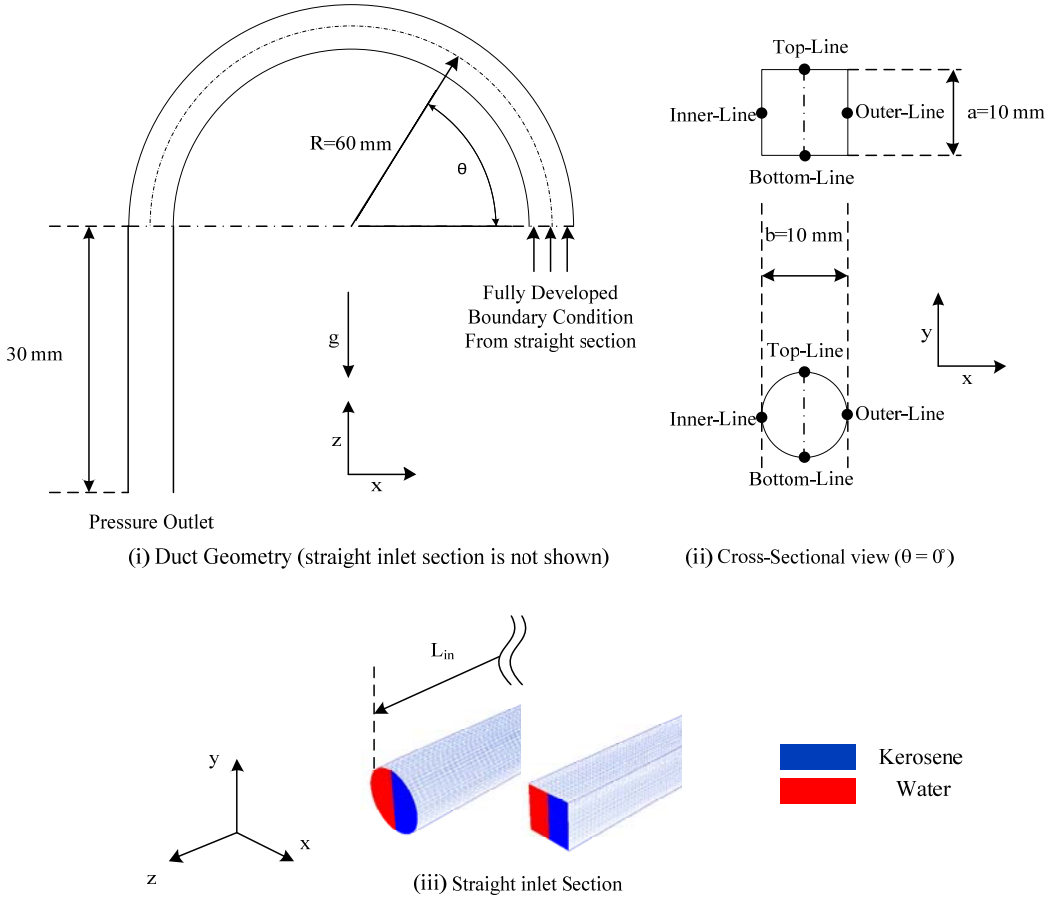

Figure 5.1. Model configuration for immiscible flow simulation showing geometrical dimensions and coordinate system

Chapter 3 described the generic aspects and possible approaches for multi-phase flow simulation. Numerical models for immiscible two-phase flow need to capture some unique flow features that are not present in other types of fluid flow. Immiscible flow through curved channels continually undergoes phase re-distribution and movement with differential flow velocities (or drift) leading to the formation of sharp interfaces between fluid phases. Thus, tracking of these interfaces and appropriate discretisation scheme are vital for simulating immiscible fluid flows. Additionally, as the fluid components are non-mixing, there is no mass transfer across phase boundaries.

Accordingly among the models discussed in Chapter 3, the Volume of Fraction (VOF) approach is identified as the most suitable to handle these special requirements of immiscible flow modelling.

Unlike Eulerian model, the VOF model solves a single set of conservation equations incorporating equivalent density for the whole domain. This approach is adequate for accurate prediction of phase distribution, interfacial movement and velocity fields in immiscible flow [63, 64], drastically saving the computational effort.

The VOF approach is further enhanced by using the Level-Set method [72] that improves the precision of phase boundary tracking. In this, the interface between two phases is captured and tracked by the level-set function defined in terms of the sign distance from the interface. The interface is then implicitly represented by the level set of $\varphi(x) = 0$ and implicitly moved by the advection of $\varphi(x)$, which is split into two steps. The first step of $\varphi(x)$ is advected using a standard numerical method. Then the second step is performed to preserve smooth profile for $\varphi(x)$ and the transition layer thickness. Both of these steps are executed using conservative second order approximations for conserving $\varphi(x)$.

5.4. Governing Equations

As described above, a VOF model coupled with Level-Set function is used for precise interface modelling of immiscible two-phase flow. With a specific discretisation scheme for volume of fraction the model robustness is improved.

Level Set function, is defined by,

$$\varphi(x) = \begin{cases} +\left|d_{\text{int}erface}\right| & x \in Phase-1 \\ 0 & x \in \Gamma \\ -\left|d_{\text{int}erface}\right| & x \in Phase-2 \end{cases} \qquad 5.1$$

where, Γ represents interface area and $d_{\text{int}erface}$ is cell distance from interface

For calculating surface tension, the interface normal and curvature are obtained according to the sign function as,

$$\vec{n} = \left.\frac{\nabla\varphi}{|\nabla\varphi|}\right|_{\varphi=0} \qquad 5.2\ (a)$$

$$\kappa = \nabla.\left.\frac{\nabla\varphi}{|\nabla\varphi|}\right|_{\varphi=0} \qquad 5.2\ (b)$$

Conservation of Level Set function is given by,

$$\nabla.(\vec{u}\,\varphi) = 0 \qquad 5.3$$

Accounting for phase effects with the equivalent bulk density, the continuity equation is given by,

$$\nabla.(\rho_m \vec{u}) = 0 \qquad 5.4$$

Taking subscript "k" to denote each phase, bulk values for a cell are described by,

$$\rho_m = \sum_{k=1}^{n} \alpha_k \rho_k \qquad 5.5\ (a)$$

$$\mu_m = \sum_{k=1}^{n} \alpha_k \mu_k \qquad 5.5\ (b)$$

The momentum equations for the VOF model coupled with Level-Set are derived as,

$$\vec{u}.\nabla(\rho_m \vec{u}) = -\nabla p + \mu_m(\nabla^2\vec{u} + \nabla^2\vec{u}^T) - \sigma\kappa\delta(\varphi) + \rho_m\vec{g} + \vec{F}_c \qquad 5.6\ (a)$$

and

$$\delta(\varphi) = \begin{cases} \dfrac{1+\cos(\pi\varphi/1.5gs)}{3gs} & |\varphi| \le 1.5gs \\ 0 & |\varphi| > 1.5gs \end{cases} \qquad 5.6\ (b)$$

where gs is grid spacing size.

Energy conservation is also a treated as a single equation for the whole domain with bulk properties and is written as,

$$\vec{u}.\nabla(\alpha_m \rho_m c_m T) = k_{fm}\nabla^2 T + \nabla.\tau^T \qquad 5.7$$

Compared to the version of 1983, Wilcox ($k-\omega$) turbulence model, which is a modified version of 2006, is reported to be much suited for representing turbulence similar to that associated with secondary flow encountered in immiscible flows. For this, the key parameters k (turbulence kinetic energy) and ω (specific dissipation rate) are obtained from the most accurate version of closure [60] in tensor notation as:

Kinematic Eddy viscosity:

$$\nu_T = \frac{k}{\tilde{\omega}}\ , \qquad \tilde{\omega} = \max\left\{\omega, C_{\lim}\sqrt{\frac{2S_{ij}S_{ij}}{\beta^*}}\right\}\ , \qquad C_{\lim} = \frac{7}{8} \tag{5.8}$$

Turbulence Kinetic energy:

$$u_j\frac{\partial k}{\partial x_j} = \tau_{ij}\frac{\partial u_i}{\partial x_j} - \beta^* k\omega + \frac{\partial}{\partial x_j}[(\nu + \sigma^*\frac{k}{\omega})\frac{\partial k}{\partial x_j}] \tag{5.9}$$

Specific dissipation rate:

$$u_j\frac{\partial \omega}{\partial x_j} = \alpha\frac{\omega}{k}\tau_{ij}\frac{\partial u_i}{\partial x_j} - \beta\omega^2 + \frac{\sigma_d}{\omega}\frac{\partial k}{\partial x_j}\frac{\partial \omega}{\partial x_j} + \frac{\partial}{\partial x_j}[(\nu + \sigma\frac{k}{\omega})\frac{\partial \omega}{\partial x_j}] \tag{5.10}$$

Closure coefficients and auxiliary relations:

$$\alpha = \frac{13}{25}\ , \quad \beta = \beta_o f_\beta\ ,\ \beta^* = \frac{9}{10}\ ,\ \sigma = \frac{1}{2}\ ,\ \sigma^* = \frac{3}{5}\ ,\ \sigma_d = \frac{1}{8} \tag{5.11}$$

$$\beta_o = 0.0708\ , \quad f_\beta = \frac{1+85\chi_\omega}{1+100\chi_\omega}\ ,\ \chi_\omega = \left|\frac{\Omega_{ij}\Omega_{jk}S_{ki}}{(\beta^*\omega)^3}\right| \tag{5.12}$$

where

$$\Omega_{ij} = \frac{1}{2}(\frac{\partial u_i}{\partial x_j} - \frac{\partial u_j}{\partial x_i})\ ,\ S_{ij} = \frac{1}{2}(\frac{\partial u_i}{\partial x_j} + \frac{\partial u_j}{\partial x_i})\ , \tag{5.13}$$

In simulation models, near-wall treatment for wall-bounded flows is a good measure of models capabilities and precision. In ω-based models viscous sub-layer is solved and matched with defect layer in contrast to classic wall function treatments. For such cases, y^+ needs to be small enough to stay within the sub-layer for the validity of turbulence model at the wall. To comply with this, it is required to have high mesh density, which becomes a model limitation for large domains, for example the two-phase flow boiling case discussed in Chapter 6. Taking y'' to be the direction normal to surface, current closure would be rewritten for the sub-layer as,

$$(\nu + \nu_T)\frac{\partial u}{\partial y''} = u_\tau^2,\ \nu_T = \frac{k}{\tilde{\omega}}\ ,\ \tilde{\omega} = \max\left\{\omega, C_{\lim}\frac{\partial u/\partial y''}{\sqrt{\beta^*}}\right\} \tag{5.14 (a)}$$

$$\frac{d}{dy''}\left[(\nu + \sigma^*\frac{k}{\omega})\frac{dk}{dy''}\right] + \nu_T\left(\frac{\partial U}{\partial y''}\right)^2 - \beta^*\omega k = 0 \tag{5.14 (b)}$$

$$\frac{d}{dy''}\left[(\nu + \sigma\frac{k}{\omega})\frac{d\omega}{dy''}\right] + \alpha\frac{\omega}{k}\nu_T\left(\frac{\partial U}{\partial y''}\right)^2 + \frac{\sigma_d}{\omega}\frac{\partial k}{\partial y''}\frac{\partial \omega}{\partial y''} - \beta_0\omega^2 = 0 \tag{5.14 (c)}$$

For matching to defect-layer solution (i.e. asymptotic to log-layer solution), the following limits should be satisfied:

$$k \to \frac{u_\tau^2}{\sqrt{\beta^*}} \text{ and } \omega \to \frac{u_\tau}{\sqrt{\beta^*}ky''} \quad \text{as} \quad y^+ \to \infty \tag{5.15}$$

Using Equation 4.7 that was introduced in Chapter 4, the non-dimensional Helicity function is now defined for each phase separately, based on applicable reference values.

Dimensionless Helicty function for phase "p" is formulated as,

$$H_P^* = \alpha_p . H . D_h \frac{\nu}{\nu_{ref}} \frac{1}{U^2{}_{in-P}} \tag{5.16}$$

This configuration facilitates the evaluation of Helicity function for each phase according to its material properties and reference values while permitting clear identification of vortex structure.

Fluid pressure is non-dimensionalised as,

$$p^* = \frac{p}{\frac{1}{2}(\alpha_p \rho_p U_{in-p}^2 + \alpha_q \rho_q U_{in-q}^2)} \tag{5.17}$$

In this immiscible flow analysis, the pressure gradient is examined for both phases at the inner and outer channel walls. For this, the pressure gradient is defined in "secondary flow-wise" direction since the secondary flow would occur in opposite directions at inner and outer channel walls. The relevant pressure gradient expressions are identical to those for single phase flow, given in Chapter 4 by Equation 4.8.

For the Second Law analysis and thermal optimisation, the irreversibility expressions for immiscible multi-phase turbulent flow are developed by modifying Equation 4.9 in Chapter 4 as,

$$S_T = (\frac{k_t}{k_m} + 1)\frac{k_m}{T^2}\left[(\frac{\partial T}{\partial x})^2 + (\frac{\partial T}{\partial y})^2 + (\frac{\partial T}{\partial z})^2\right] \tag{5.18 (a)}$$

$$S_P = \frac{\mu_m}{T}\left[2[(\frac{\partial u}{\partial x})^2 + (\frac{\partial v}{\partial y})^2 + (\frac{\partial w}{\partial z})^2] + (\frac{\partial u}{\partial y} + \frac{\partial v}{\partial x})^2 + (\frac{\partial w}{\partial y} + \frac{\partial v}{\partial z})^2 + (\frac{\partial u}{\partial z} + \frac{\partial w}{\partial x})^2\right]$$
$$+ \frac{0.09\rho_m . k . \omega}{T} \tag{5.18 (b)}$$

In these S_T and S_P expressions, additional irreversibility terms appear due to turbulence structures in comparison to the laminar version given by Equation 4.9 in Chapter 4. Volumetric averaging, total entropy and Bejan number are defined similar to single phase model as given by Equation 4.10 and 4.11 in Chapter 4.

5.5. Grid sensitivity analysis and Mesh selection

In relation to single and two-phase flow modelling, the Chapters 3 and 4 presented a brief discussion on generic details of grid generation, restrictions and requirements. For ensuring the reliability of computational fluid dynamics results, a grid sensitivity analysis is a foremost requirement by which the predicted solutions are shown to be independent on the grid size beyond a certain threshold. In this, different grid configurations/topologies could be attempted and/or grid size can be gradually refined until results show no significant change.

For simulations involving turbulence closures, in addition to establishing the grid independence, a chosen grid needs to satisfy specific turbulence modelling requirement in terms of y^+ near the solid wall boundaries to achieve smoother laminar to turbulent transition. For the immiscible flow discussed in this chapter, it is required to ensure y^+ remains below a value of 5 throughout the solution domain [60, 63].

In the immiscible model developed in this Chapter, the analysis is carried out with a fully hexagonal grid for both rectangular and circular channels. However, a five-zone topology is used only for the (elliptical) circular cross section in accounting for sharp gradients, as mentioned in Section 4.33 in Chapter 4.

Figure 5.2 presents the approach adopted to perform the grid sensitivity test and to obtain the optimum mesh size for the immiscible flow analysis discussed in this chapter. The primary phase volume fraction is chosen for examining the grid dependency because this scalar parameter is readily affected by other convective terms. The volume fraction profiles for the primary phase are evaluated at the vertical and horizontal centre planes at the exit of rectangular and circular curved channels and are presented as four sub-figures in Figure 5.2. Meshes 1 to 4 are the finest of the grids tested, representing uniform grid spacing of 1.0 mm, 0.5 mm, 0.25 mm and 0.1 mm, respectively.

It is observed that any finer mesh beyond 0.25 mm grid size (Mesh 3) does not impart significant changes in any of the volume fraction profiles although computational effort is considerably increased. For this reason, Mesh 3 with 0.25 mm spacing is chosen to be the optimal grid size for simulation.

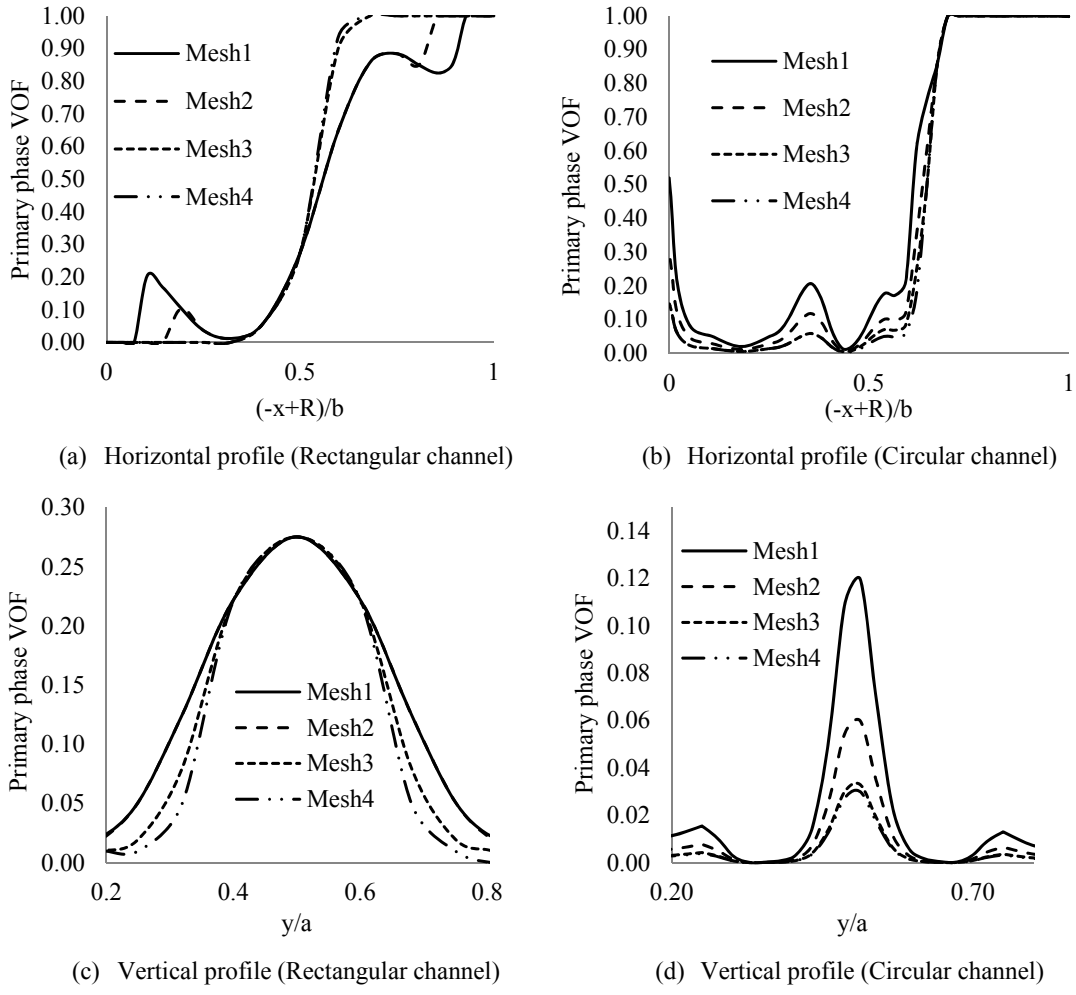

(a) Horizontal profile (Rectangular channel)

(b) Horizontal profile (Circular channel)

(c) Vertical profile (Rectangular channel)

(d) Vertical profile (Circular channel)

Figure 5.2. Grid sensitivity analysis for multi-phase immiscible flow

In addition to the above grid selection satisfying grid independency, the validity of turbulence closure is ascertained for the chosen mesh size. For this purpose, three mesh layers are set up next to the solid wall starting with a grid spacing of 0.01 mm and expanding at a rate of 3. This arrangement provides a reliable y^+ value on the wall and then smoothly integrates these three grid layers with the main grid.

Figure 5.3 depicts y^+ distributions in rectangular and circular channel cross sections along the four planes identified by the "Top-line, Bottom-line, Inner-line and Outer-line" in Figure 5.1. These profiles are obtained for the case of maximum inlet velocity

for both fluid phases at $U_{in\text{-}Phase1} = U_{in\text{-}Phase2} = 1$ m/s. The profiles along the Top-line and Bottom-line in both geometries overlap because there is no effect from gravity or centrifugal forces along the y-axis. With the selected grid size, y^+ value is generally larger for the rectangular channel than the circular channel owing to sharp corners in rectangular geometry. Nonetheless, y^+ remains below 5 over the entre domain confirming the validity of turbulence closure near the solid wall boundary.

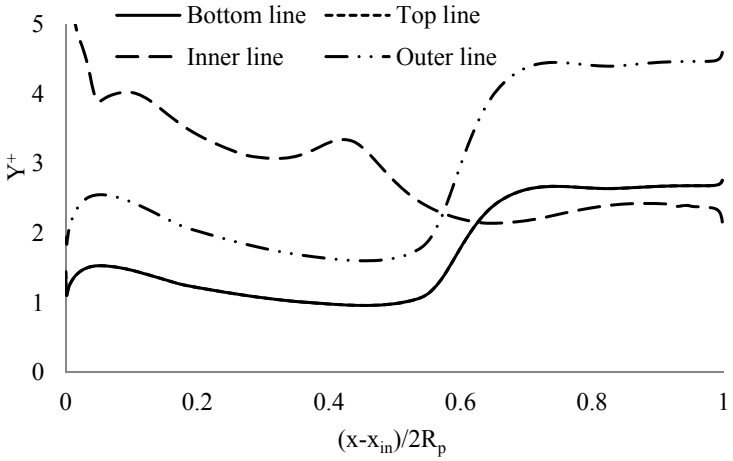

(a) Rectangular cross section

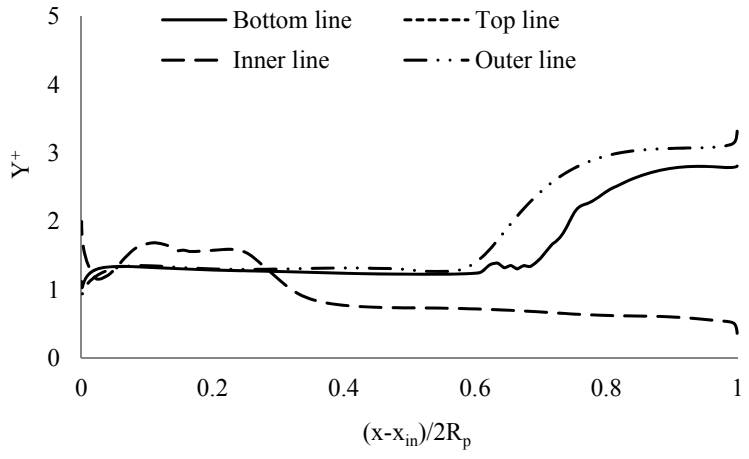

(b) Circular cross section

Figure 5.3. Local y^+ profiles for rectangular and circular channel cross sections

5.6. Results and Discussion

5.5.1 Phase distribution in immiscible fluid flow

The two-phase mixture used in the present case study consists of liquid water (Phase 1) and liquid kerosene (Phase 2), whose physical properties are given in Table 5.1. It is noted that the water is the heavier phase while the kerosene is higher in viscosity and Prandtl number. Thus, the behaviour of Phase 1 is biased towards the secondary flow formation by centrifugal effects whilst that of Phase 2 favours convective thermal transportation. The behavioural differences based on phase properties are used in the following discussions. Both phases enter the straight inlet channel section through equal areas, as shown in Figure 5.1(c), with independently-varied inlet velocities.

Table 3 Material properties of different applied liquid

Property	Kerosene	Water
ρ (kg/m^3)	780	998.2
μ (kg/m.s)	0.0024	0.001003
c_p (J/kg.K)	2090	4182
k_f (W/m.K)	0.149	0.60
Pr	33.7	6.99

The current VOF-based numerical simulation uses a formulation relating the pressure difference between the phases and the interface surface tension. It defines the volume fraction of the heavier phase in relation to the total mixture volume thus, designating a value of one for totally water phase and zero for kerosene only phase. Figure 5.4 depicts the cross sectional phase distribution along the curved channel from its inlet ($\theta = 0^\circ$) to the outlet ($\theta = 180^\circ$) for both rectangular and circular geometries. In this, the red contours indicate Phase 1 (heavier) and the blue contours show Phase 2 (lighter) while the left side of figure represents the inner channel walls.

At inlet ($\theta = 0^\circ$), Phase 1 enters the channel attached to the inner wall while Phase 2 flows closer to the outer wall. The interfacial boundary between the two phases is essentially a vertical line for both types of channels. For locations of $\theta > 0^\circ$, the mixture experiences the centrifugal effect induced by the channel curvature, which is more profound on the heavier Phase 1. However, the dynamic fluid balance among interactive centrifugal, inertial and viscous forces finally determines the rearrangement of fluid phases in the flow domain. This phase migration is clearly illustrated in the sub-figures of Figure 5.4.

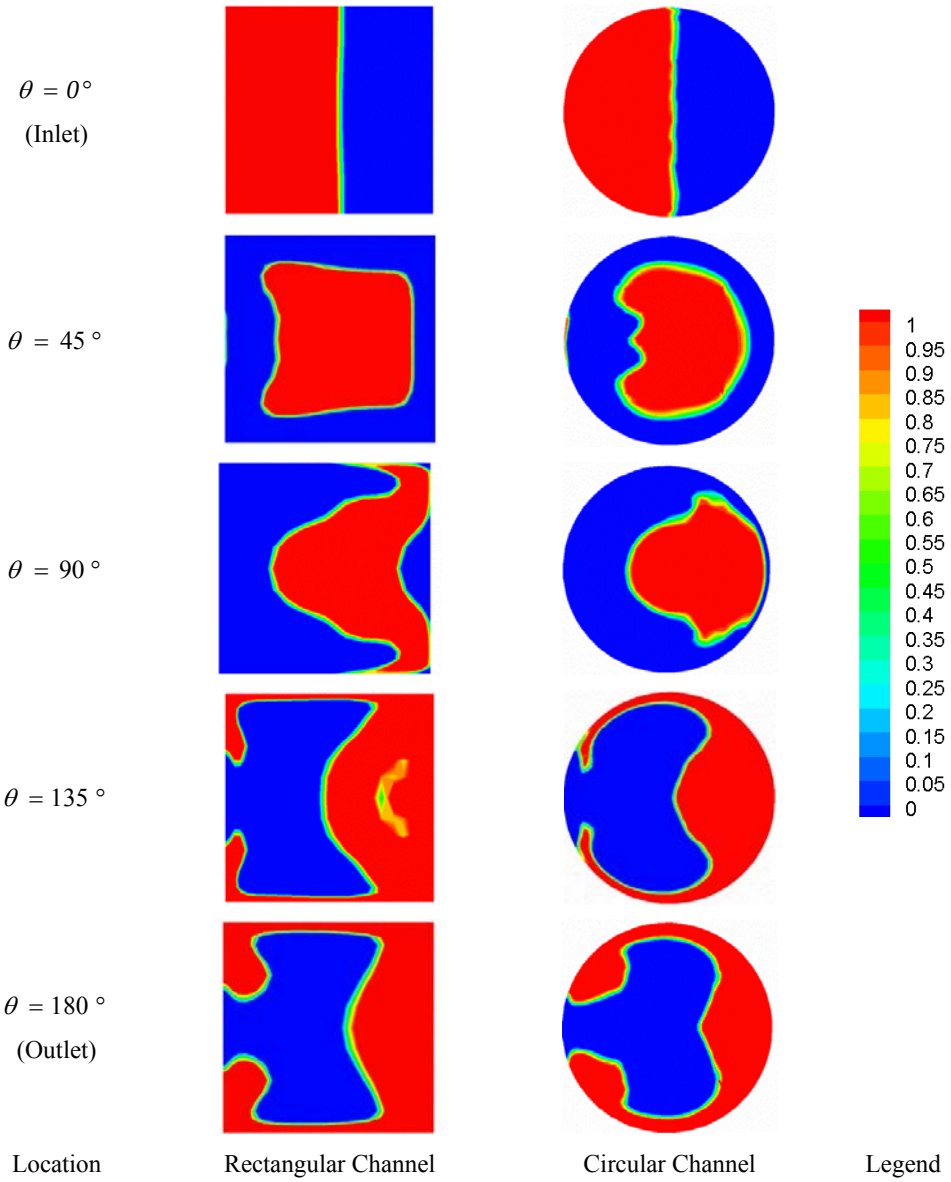

Figure 5.4. Volume of fraction contours depicting phase distribution at various cross sections along rectangular and circular curved channels
(*Left side of sub-figures represents inner channel wall,* $U_{in-1} = U_{in-2} = 1 \ \ m/s$)

At ($\theta = 45^{\circ}$), Phase 1 is seen to reside in dynamic equilibrium in the centre of the cross section surrounded by Phase 2. Moving further downstream, the immiscible mixture is subjected to extended centrifugal action that forces Phase 1 to migrate towards the outer wall, gradually displacing the cushioning layer of Phase 2, as illustrated by sub-figures of $\theta = 90^{\circ}, 135^{\circ}$ and 180°. In these new phase distributions, Phase 1 flows attached to the outer wall while Phase 2 is biased towards inner wall, which is completely opposite to the phase behaviour at inlet.

5.5.2 Immiscible fluid flow patterns and secondary flow vortices

Compared to other types of fluid flows, immiscible two-phase flow in curved channels tends to have unique secondary flow behaviour because these flow characteristics are determined by the coupled action of curvature-induced centrifugal effects and momentum transfer between phases. These are further compounded by the density and viscosity differences between phases that alter the relative strength of inertial, viscous and centrifugal forces in determining the fluid flow behaviour. Consequently, each phase essentially behaves as a separate secondary flow cell within which stagnation regions are developed with the potential for vortex formation and hydrodynamic instability. However due to the momentum coupling between phases, secondary flow circulations within the phases are interlinked, giving rise to more complex flow patterns compared to single phase fluid flow in curved channels.

The flow patterns in immiscible flow are examined by using the dimensionless helicity function, as defined by Equation 5.16, separately for each phase. Figure 5.5 depicts the helicity distribution for each phase along the curved channel from inlet ($\theta = 0^\circ$) to the outlet ($\theta = 180^\circ$) for both rectangular and circular geometries. In this, the red and blue contours are for Phase 1 and Phase 2, respectively while the solid lines and dashed line respectively indicate the clock-wise and counter clock-wise rotations of fluid circulation. The left side of sub-figures in Figure 5.5 represent inner channel wall. As evident, these secondary flow patterns are far more complex and uniquely different to those in single phase fluid flow in curved channels.

At inlet ($\theta = 0°$), Figure 5.5 shows the initial stage of secondary vortex formation within individual phase boundaries. At this stage, Phase 1 flows closer to the inner wall and the fluid circulations in each phase occur in the same corresponding direction at the top and bottom half of channel cross section. When the fluid moves downstream ($\theta > 0^\circ$), the extended centrifugal action intensifies the secondary flow circulation and displaces Phase 2 circulation towards the inner wall, as shown by the patterns at $\theta = 90°$. Such pockets of highly localised secondary vortices do rotate in opposite directions indicating the transfer of fluid momentum between adjacent vortex cells embedded within the same phase or across phase boundaries. By the channel exit ($\theta = 180^\circ$), the momentum transfer of Phase 1 circulations become so strong to confine Phase 2 circulation practically to the centre of channel.

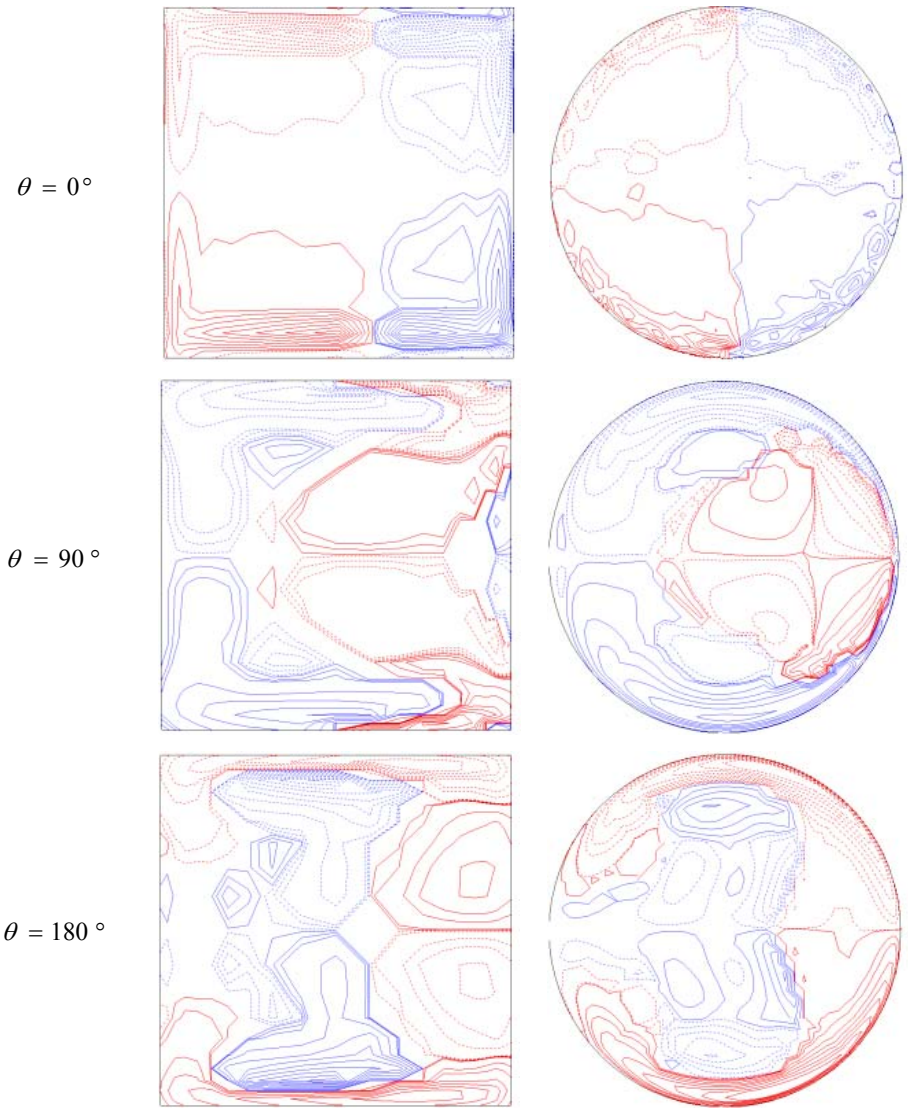

Figure 5.5. Dimensionless helicity contours for immiscible flow domain
(Left side of sub-figures represents inner channel wall, $U_{in-1} = U_{in-2} = 1 \ \ m/s$ *)*

As observed above, the interactive mechanism of the secondary flow developed by centrifugal action and the momentum transfer across phase boundaries uniquely determine the immiscible two-phase flow behaviour in curved channels. For the case depicted in Figure 5.5, each phase enters with an equal inlet velocity of 1 m/s, thus the momentum transfer is not biased towards any particular phase, apart from the possible impact of their fluid property differences. Varied phase velocity differences accentuate the influence on secondary flow behaviour from the momentum flow across phases. Figure 5.6 shows the effects of phase velocity ratio on secondary flow structures.

5.5.3 Phase velocity ratio effects

In examining the effects of the velocity differential (or drift) between phases, three velocity combinations are considered, namely Case (A), Case (B) and Case (C), where the ratios of Phase 1 to Phase 2 velocities are set at 0.25, 1.0 and 4.0, respectively.

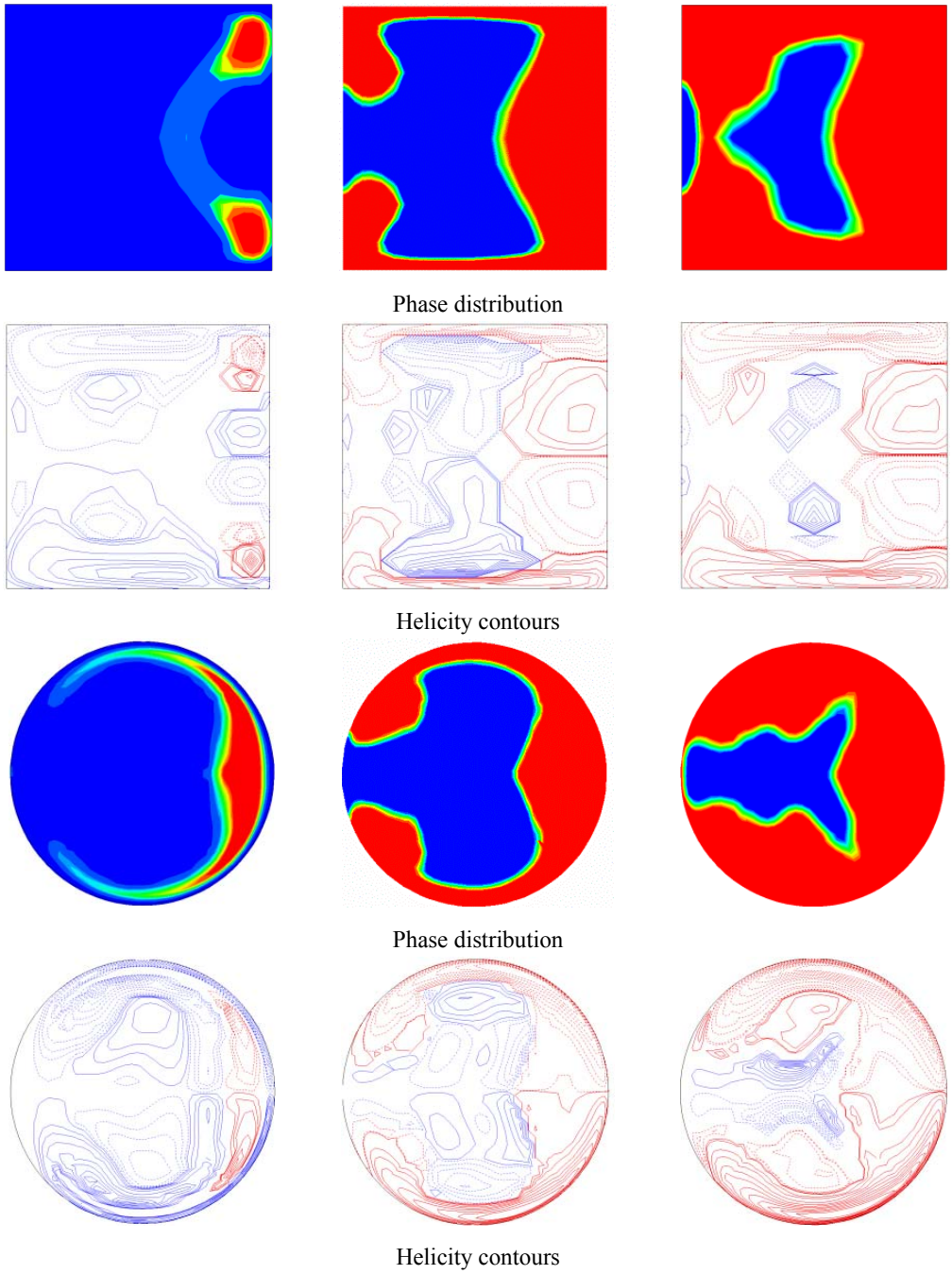

Case A	**Case B**	**Case C**
Velocity Ratio = 0.25	*Velocity Ratio = 1.0*	*Velocity Ratio = 4.0*
$U_{in\text{-}1}$ *= 0.25 m/s,* $U_{in\text{-}2}$ *= 1.0 m/s*	$U_{in\text{-}1}$ *= 1.0 m/s,* $U_{in\text{-}2}$ *= 1.0 m/s*	$U_{in\text{-}1}$ *= 1.0 m/s,* $U_{in\text{-}2}$ *= 0.25 m/s*

Figure 5.6. Velocity ratio effect on phase distribution and secondary flow structures
(Left side of sub-figures represents inner channel wall)

For these three cases, Figure 5.6 depicts the phase distribution and the flow (helicity) patterns at the exit of both rectangular and circular channels. It is observed that, although the heavier Phase 1 enters the curved channel attached to the inner wall, it gets displaced to the outer wall by the channel exit under the influence of centrifugal forces for all velocity ratios. At the low velocity ratio of 0.25, the bulk flow is occupied by strong secondary flow circulation in Phase 2. This circulation imparts momentum transfer on Phase 1 to set up localised Phase 1 circulations near the outer wall. Under these conditions, the flow patterns are dominated by momentum transfer from Phase 2 to Phase 1. As the velocity ratio is increased, the centrifugal forces emphasise the secondary flow circulation in Phase 1 because of its high density and lower dynamic viscosity compared to Phase 2. This causes the circulatory momentum of Phase 1 to act against and reverse the momentum flow from Phase 2. Consequently at increased velocity ratios, the bulk flow pattern begins to be dominated by Phase 1 circulation, as shown by Figure 5.6.

5.5.4 Detection of Dean's Instability

In Chapter 4, the outer wall pressure gradient profile and the dimensionless helicity threshold were presented as possible two techniques for detecting Dean's Instability in single phase fluid flow in curved channels. It was identified that the helicity method is more suitable for all channel geometries since the pressure gradient approach tends to over predict Dean's Instability for circular (and elliptical) channels.

The suitability of the wall pressure gradient approach is appraised in Figure 5.7 for immiscible two-phase flow as a tool for identifying the formation features of secondary flow vortices. This approach would require the evaluation of pressure profiles on the inner and outer channel walls because both fluid phases have simultaneous secondary flow circulations within the confines of their individual phase boundaries.

Considering the flow conditions of Cases (A), (B) and (C), it is readily noticed from Figure 5.7 that the wall pressure gradients show negative-to-positive change at both inner and outer walls. This is in contrast to the cases with single phase flow where only the outer walls show pressure responses to secondary vortex formation. The examination of flow patterns in Figure 5.6 affirms the appearance of secondary vortices at both the inner and outer channel walls. This means that the pressure gradient technique is useful as qualitative method in detecting secondary flow activity in the two phases. However, this usefulness is undermined by the fact that Phase 2 is shifted

towards the channel centre by the influence Phase 1 momentum transfer at high velocity ratios, as depicted in Figure 5.6. As such, although the pressure gradient profile is useful for some qualitative assessment of Dean's Instability, it is uncertain and remains less effective as a criterion for vortex detection in immiscible flow and, the helicity threshold technique is considered more appropriate.

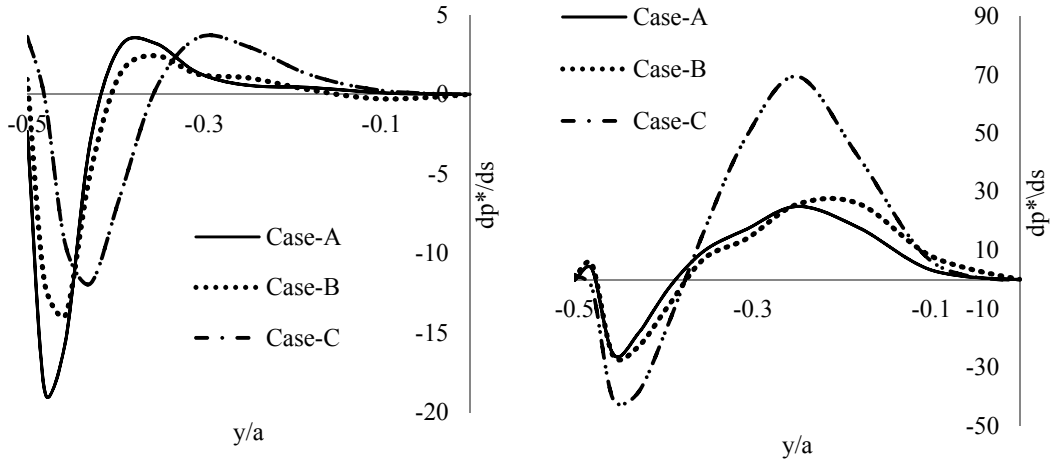

(a) Profile at inner wall (b) Profile at outer wall

Figure 5.7. Wall pressure gradient at exit of rectangular channel for Cases (A) (B) (C)

From Figure 5.7, it is further observed that, sharper and larger gradients are generally present at the outer walls, which are accentuated with increased velocity ratio. This indicates a higher intensity of flow instability in Phase 1 compared to Phase 2, which is clearly supported by the helicity profiles in Figure 5.6 showing a stronger presence of vortices in Phase 1 and subdued circulation in Phase 2.

5.5.5 Behaviour of phase interfacial area

The interfacial area between fluid phases is a crucial parameter for immiscible fluid components reacting with each other, such as in chemical processing where maximised interfacial contact improves production efficiency. Figure 5.8 shows the ratio of interfacial phase area for immiscible flow through curved channel (IA_{Curved}) to that in straight channels ($IA_{Straight}$) with respect to the inlet velocity ratio.

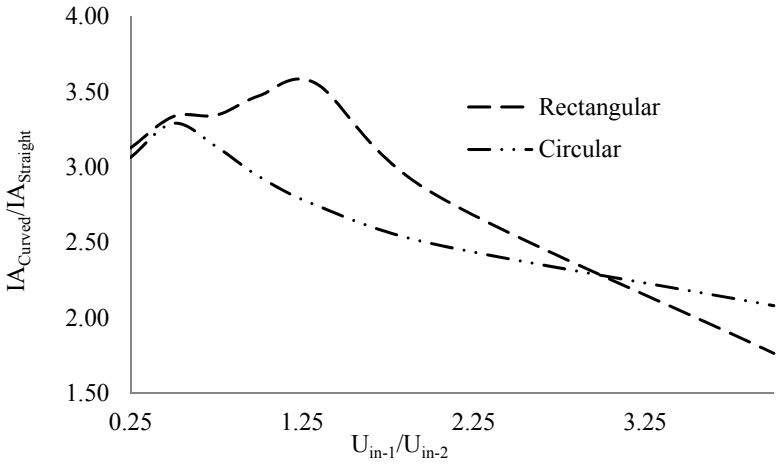

Figure 5.8. Variation of interfacial area between phases with velocity ratio

It is clearly evident that the immiscible flow through a curved channel provides more than 3 times interfacial area between phases compared to a straight channel. This shows the usefulness of the curved geometry in improving the reaction potential between phases although it may accompany a slight pressure loss penalty. A rectangular curved channel is seen to provide up to 60 per cent more interfacial area compared to a circular channel at lower velocity ratios. For increasing velocity ratio, the interfacial area advantage gradually diminishes for both rectangular and circular channels along with higher magnitudes of pressure drop.

5.5.6 Immiscible fluid flow thermal characteristics

As discussed in Chapter 4, the forced convection in single phase fluid flow in curved channels is highly influenced by the secondary vortices and thermally-induced buoyancy. In immiscible fluid flow in curved channels, additional influences are imparted by non-uniform fluid mixture properties on the thermal characteristics. These property differences essentially affect the intensities of the phase momentum exchange and the centrifugal action that drive secondary flow circulations within phases, which in turn directly impact on the channel heat transfer process.

For both rectangular and circular channels, Figure 5.9 illustrates the channel wall temperature distribution and the influence from velocity differences in Phase 1 and 2. For this, Figure 5.9 uses the velocity ratios of 0.25, 1.0 and 4.0 that are considered in Figure 5.6 for Cases (A)(B)(C), respectively. These profiles indirectly demonstrate the effects of having non-uniform fluid properties in the immiscible flow.

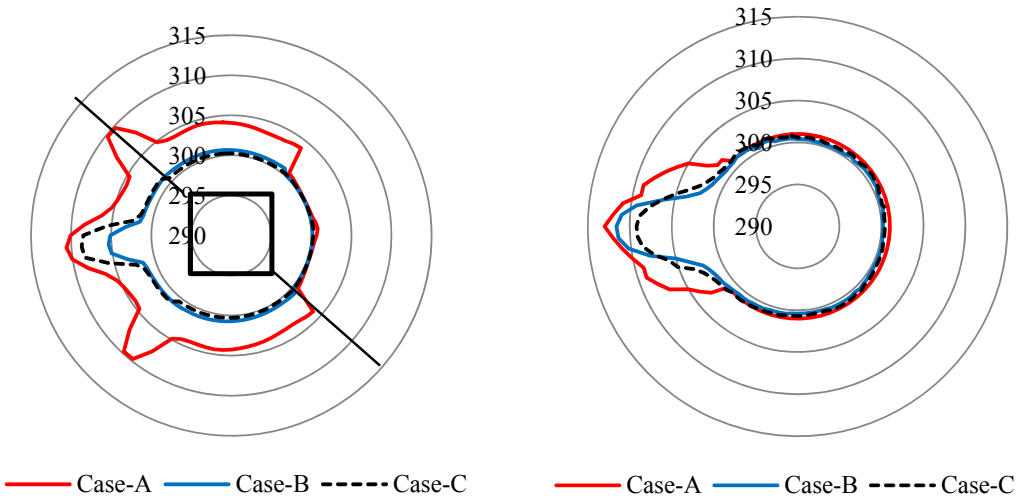

(a) Rectangular cross-section (b) Circular cross-section

Figure 5.9. Channel wall temperature (K) distribution at outlet
(Left side of sub-figures represents inner channel wall)

In analysing these profiles, two crucial aspects are to be noted. Being the phase with a higher density and lower kinematic viscosity, the centrifugal forces have more influence on Phase 1 (Water) in generating secondary flow than on Phase 2 (Kerosene). Therefore, Phase 1 contributes to the overall channel heat transfer process through forced convection due to secondary flow. On the other hand, being the lighter phase with a higher viscosity, Phase 2 is less influenced by centrifugal forces than Phase 1 and is weaker in forming secondary flow circulations. However because of its larger Prandtl number, Phase 2 is more diffusive to heat transportation than Phase 1 and contributes to the overall channel heat transfer by thermal diffusion. These attributes of Phase 1 and Phase 2 are used below in the discussion.

With reference to Figure 5.9(a), it is seen that the peak temperature at the inner wall falls when the velocity ratio is increased from 0.25 to 1.0 and then elevates again when the velocity ratio is further increased to 4.0. This is explained as follows.

As shown by Figure 5.6 at the velocity ratio of 0.25, the rectangular channel walls are mostly in contact with the fluid Phase 2 having less vigorous secondary flow circulation but higher thermal transport characteristics. Therefore, the channel wall heat transfer is primarily governed by Phase 2 and biased towards the attributes of thermal diffusion in phase 2. By increasing the velocity ratio to 1.0, the dominant phase distribution within the channel is shifted from Phase 2 to Phase 1, as depicted in Figure 5.6, concurrently strengthening the secondary flow circulation in Phase 1. Thus, the Phase 1 convective heat transfer based on secondary flow effects is increased while Phase 2 still

contributing with some thermal diffusion. Hence, the higher overall heat flow reduces the channel wall temperature. When the velocity ratio is further increased to 4.0, the channel is primarily occupied by Phase 1 with a very small Phase 2 fluid circulation at the inner wall, as shown by Figure 5.6. Therefore, the overall heat flow is very much biased towards the forced convection brought about by Phase 1 secondary flow circulation. This reduces the magnitude of overall channel heat flow, hence again elevating the inner channel wall temperature at this velocity ratio of 4.0.

The circular channel wall temperature in Figure 5.9(b) behaves slightly different to the rectangular channel temperature. In the circular channel, the peak temperature at the inner wall continually falls when the velocity ratio is increased from 0.25 to 4.0. This is because with the increased velocity ratio, the circular channel cross section geometry readily deflects the Phase 1 secondary flow circulation in the vicinity of the outer wall towards the inner wall, shifting Phase 2 away from the inner wall, as seen in Figure 5.6. Consequently, the phase distribution within this geometry favours heavier Phase 1 reducing the influence from Phase 2 for all velocity ratios. Hence, the overall heat transfer steadily increases with a continuing reduction in inner wall peak temperature.

5.5.7 Flow irreversibility analysis and thermal optimisation

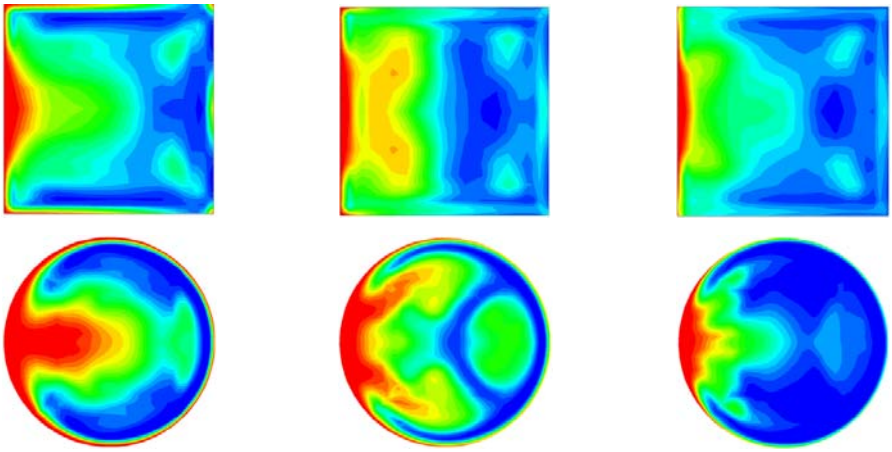

Figure 5.10. Bejan number contours indicating thermal irreversibility map at channel exit
(Left side of sub-figures represents inner channel wall), $\dot{q} = 5000 \ \ W/m^2$

As Bejan Number contours, Figure 5.10 provides a Second Law thermal irreversibility map of the flow situations discussed in Section 5.5.6. It is evident that, at low velocity ratio, heat transfer-related irreversibility (red zones) is essentially confined to the inner channel wall, signifying higher temperature differences in the fluid. This irreversibility has a higher magnitude in circular ducts than in rectangular duct implying the latter

geometry would deliver the wall heat more efficiently to the fluid. However, the rectangular channels tend to have higher phase interfacial area compared to circular channels, as evident from Figure 5.8 and qualitatively seen in the helicity contours of Figure 5.6. This may incur higher viscous loses across phase boundaries in rectangular ducts than in circular ducts. In addressing these, the variations of flow irreversibility due to temperature (S_T), that due to viscous forces (S_P) and the total irreversibility (S_{gen}) are examined in Figure 5.11 with a view to develop a thermal optimisation approach for curved channels.

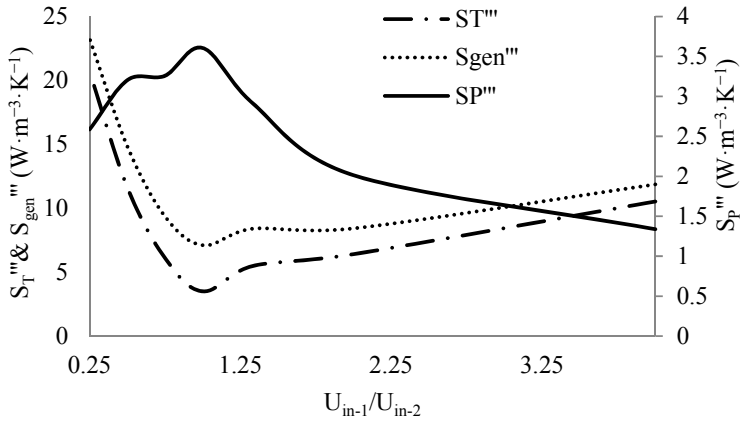

(a) Rectangular cross section

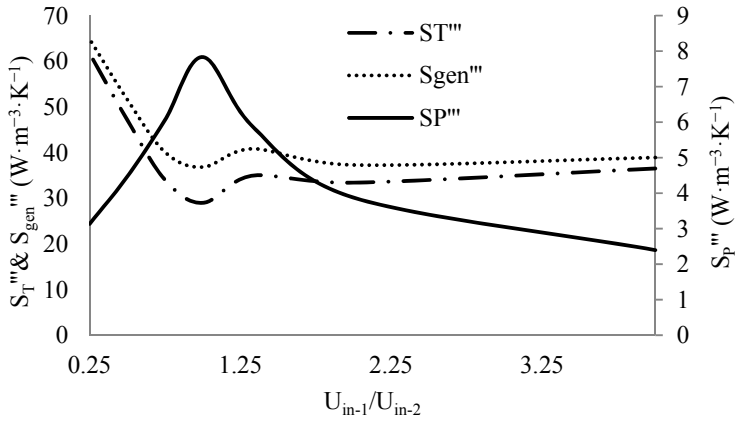

(b) Circular cross section

Figure 5.11. Variation of volumetric-averaged irreversibility and total flow entropy $\dot{q} = 5000 \ \ W/m^2$

Figure 5.11 indicates that thermal irreversibility (S_T) is of much higher magnitude than the viscous irreversibility (S_P) for both channels, implying that the total flow entropy is dominated by heat transfer processes. This is to be expected for there are two thermal mechanisms in operation, namely the secondary flow effects and the enhanced thermal diffusion due to a phase with higher Prandtl number. Figure 5.11 also show that, S_T is

minimised and S_P reaches a peak when the phase velocity ratio approaches unity. Attributable reasons for these behaviours are discussed below.

At velocity ratio of 1.0, helicity profiles in Figure 5.6 qualitatively indicate a higher degree of contact between secondary circulations in Phases 1 and 2, which is vindicated by Figure 5.8 as high phase interfacial area around this flow rate combination. Also, at this velocity ratio, both phases have their highest intensity of secondary circulation, and therefore the phase momentum transfer, as inferred from Figure 5.6. These two mechanisms jointly cause the immiscible flow to experiences largest viscous loses at this velocity ratio.

The minimisation of S_T is a direct result of having the most favourable channel heat transfer at the velocity ratio of 1.0. Under these flow conditions, Phases 1 and 2 contribute to the overall heat transfer through the most intense individual secondary flow circulations, as judged from Figure 5.6 helicity profiles. At this velocity ratio, two fluid phases are similarly distributed within the flow domain. This allows Phase 2 to provide a significant contribution to the overall heat flow from thermal diffusion in addition to its secondary flow-based forced convection. Consequently, both phase jointly operate to increase the overall channel heat flow with the minimised thermal irreversibility.

As evident from Figure 5.11, the total entropy, which is the sum of S_T and S_P, indicates a minimum around the velocity ratio of 1.0. This minimum point represents the best trade-off between opposing aspects of favourable thermal behaviour and adverse viscous loses in the channel. Thus, it suggests an optimisation method for curved channels carrying immiscible mixture of fluids, where the total flow irreversibility acts as a useful and practical design parameter.

5.7. Summary

In this chapter, the fluid and thermal behaviour of a two-phase immiscible fluid mixture was examined within both rectangular and circular curved channels. The unique flow characteristics were assessed and explained by considering the effects from the centrifugal forces due to channel curvature and the momentum transfer across the phases. The channel convective heat transfer process is strongly influenced by the

intensity of secondary flow as well as the non-uniform phase property distribution. Extending this investigation of immiscible multi-phase flow, the next chapter examines the two-phase flow through curved channels with additional mass transfer (evaporation) at phase boundaries.

CHAPTER 6

Flow Boiling In Curved Channels

6.1. Scope of chapter

This chapter focuses on study of a multi-phase flow having mass transfer through interfaces and boiling heat transfer is discussed in details. Using Eulerian multi-phase flow and wall heat partitioning approach and by assigning appropriate closures from literature, unique influence of centrifugal force on phase rearrangement and accordingly boiling heat transfer in curved ducts with different shapes of cross section is investigated. In such term, straight and curved pipe are compared and effectiveness of curvature is discussed regarding heat transfer enhancement and postponing temperature increase in presence of high heat flux.

6.2. Introduction

Flow boiling and associated heat transfer characteristics are crucial design considerations for thermal power generation and heat recovery systems. Through decades of experimental work and numerical modelling, extensive knowledge base has been developed in understanding the flow boiling regimes and thermal behaviour in straight pipes. However, the two-phase flow behaviour in curved fluid passages remains very much an unexplored area although such flow geometries are commonly found as an integral part of many industrial heat transfer equipment of the kind, gas turbine blades, boilers, helical heat exchangers and cooling system of centrifuges. In heated ducts, the secondary flow affects the heat transfer characteristics by phase rearrangement and special vortices structure. In previous chapters, single phase and liquid-liquid flow through curved ducts, a significant degree of investigation has been conducted to understand the intricate details of secondary flow interactions.

Experimental studies were associated with particular concerns regarding boiling such as high working pressure, presences of dry-out, burnout and critical heat flux, boiling investigation was so expensive and in some cases almost inaccessible. Besides, investigations of flow boiling and thermal characteristics in curved passages remain so much unexplored, in terms of numerical modelling.

Influence of source terms such as drag, lift, surface tension and extra turbulence generation sources on boiling and corresponding characteristics are extensively studied. Secondary flow, in multi-phase regimes, effects first on phase rearrangement where the phase with higher density (i.e. liquid phase) experiences a higher centrifugal force and moves toward outer side of curvature. The unsymmetrical resulting flow pattern will fundamentally change the phase change regime (mass transfer from liquid to vapour phase), heat transfer and other boiling characteristics in curved ducts.

This chapter represents an investigation on flow boiling within curved pipes, where pipe curvature intrinsically produces secondary flow and hence, fundamentally different flow characteristics as compared to straight pipes. For this, boiling process influenced by secondary flow effects, the study develops a novel three-dimensional simulation methodology based on a non-equilibrium model with Eulerian multi-phase approach. It incorporates an incompressible multi-phase turbulent solver with k-ε model for excellent integrity of predicted results and considerable computational advantage. The model is tested for numerical stability and validated against reported experimental results. The flow regimes and temperature fields are obtained for flow boiling in curved pipes and compared with those in straight ducts with an analysis on observed differences in fluid and thermal characteristics. The study evaluates individual wall heat flux components that make up the overall heat transfer, namely that from liquid evaporation, quenching, single phase liquid and single phase vapour. These are effectively used for illustration and physical interpretation of the unique effects from pipe curvature on the flow boiling process. The study also discusses the parametric influence from liquid sub-cooling, wall heat flux and centrifugal forces on flow patterns and, the onset of flow boiling in curved pipes along with the phase change and associated heat transfer.

6.3. Geometry, Operating and Boundary Condition

The model geometry is shown in Figure 6.1 along with relevant dimensions and consists of a 90o curved circular pipe of length LH = 950 mm which is connected to a straight pipe section of length LNH = 300 mm. The pipe arrangement is positioned in a vertical plane with the fluid flowing upwards. The curved pipe length is uniformly heated by a constant heat flux while the straight pipe section is unheated. The working fluid water enters the curved pipe at the bottom with a fully developed velocity profile that includes turbulent characteristics. The fluid leaves the straight pipe with a pressure outlet boundary condition. For the purpose of comparing the boiling regimes in curved and straight pipes, a separate model is also developed having straight vertical pipes for both heated and unheated pipe sections with identical dimensions and operating/boundary conditions. The system pressure is set to 40 atm for which the corresponding water properties given in Table .6.1.

Table 6.1. Material Properties of water for both liquid and vapour phases at 40atm (4.053Mpa)

	Liquid	Vapour
ρ (kg/m^3)	798.37	20.09
μ (kg/m.s)	1.05×10^{-4}	$1.75E\times10^{-5}$
k_f (w/m^2.K)	0.6224	0.0515
C_p (J/kg.K)	4860.00	4021.10
T_{sat} (K)	523.5	
σ (n/m)	0.028	
$\Delta h_{standard}$ (J/kg.mol)	2.95×10^{7}	

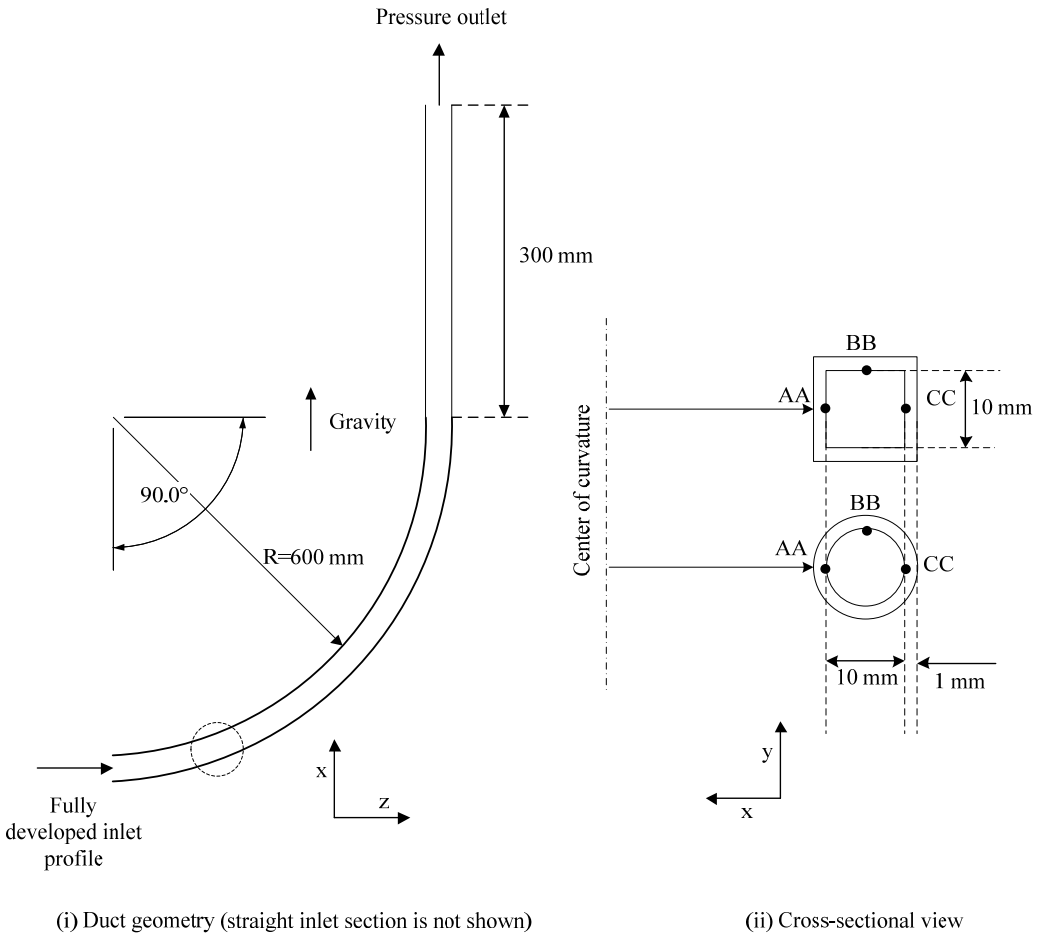

Figure 6.1. Geometry and pipe arrangements applied for current simulation

6.4. Governing equations

6.4.1. Mass and momentum conservation

Flow composition in boiling basically a two-phase vapour-liquid flow with varying regimes ranging from bubbly to full vapour phase. Boiling and condensation in the flow are mass transfer processes associated with heat transfer on phase change. Among multi-phase models, the Eulerian model is reported best for it considers phases separately and solves the sets of momentum and energy equation for each phase. The volume fraction in continuity equation captures the phase boundaries wherein mass and heat transfers are also defined for each phase separately. A model known as boiling closure provides the coupled correlation between heat and mass transfer in boiling/condensation processes.

For the explained configuration of model, continuity equation for the phase "q" is;

$$\nabla.(\alpha_q \rho_q \vec{v}_q) = \dot{m}_{pq} - \dot{m}_{qp} \qquad 6.1$$

The momentum and energy conservation equations;

$$\nabla(\alpha_q \rho_q \vec{v}_q) = -\alpha_q \nabla p + \nabla.\vec{\tau}_q + \nabla.\vec{\tau}^{T}{}_q + \alpha_q \rho_q \vec{g} + \vec{F}_{pq}^{D} + \vec{F}_{pq}^{TD} + \dot{m}_{pq}\vec{v}_{pq} - \dot{m}_{qp}\vec{v}_{qp} + \vec{F}_{q-body} + \vec{F}_{lift} \qquad 6.2\ (a)$$

$$\nabla(\alpha_q \rho_q c_{pq} T_q) = k_{fm} \nabla^2 T_q + \nabla.\tau^{T}{}_{Tq} + Q_{pq} + \dot{m}_{pq} h_{pq} - \dot{m}_{qp} h_{qp} \qquad 6.2\ (b)$$

$\vec{F}_{body}$ and $\vec{F}_{lift}$ are body and lift forces respectively while $\vec{F}_{pq}^{D}$ and $\vec{F}_{pq}^{TD}$ are drag force and turbulence drift force. The effect of surface tension on pressure difference between different phases and shape of boundaries are taken into account by approach suggested by Brackbill et al [73].

6.4.2. Turbulence model

The viscous regime for tube boiling case is turbulent. $\nabla.\vec{\tau}_q$ in equations 6.2 (a)&(b) is Reynolds stress tensor and $\nabla.\tau^{T}{}_{Tq}$ is temperature turbulence tensor which is in from of generalized scalar turbulence tensor. These two terms make momentum and energy equations coupled with two transport equations (depending on applied model) known as turbulent closures. Among available turbulence closures $k-\varepsilon$ and $k-\omega$ are widely applied for multi-phase Eulerian model and reported to have a good consistency with experimental results. Although $k-\omega$ model solves turbulence equation for sub-layer which improves wall turbulent characteristics, considering y^+ confinements, cells number significantly increases due to mesh refinement toward walls. Accordingly, $k-\varepsilon$ with standard wall function could be applied as it represents a good compromise of consistency with experimental results and demand for computational resource. $k-\varepsilon$ RNG turbulence model, which is reported as a reliable model for bubbly flow [74] and where RPI sub-model is used [51, 55], is adopted through following equations:

$$\nabla.(\rho_m \vec{v}_m k) = \nabla^2(\mu_m + \frac{\mu_t}{\sigma_k})k + G_k - \rho_m \varepsilon + S_k \qquad 6.3(a)$$

$$\nabla.(\rho_m \vec{v}_m \varepsilon) = \nabla^2(\mu_m + \frac{\mu_t}{\sigma_\varepsilon})\varepsilon + C_{1\varepsilon}\frac{\varepsilon}{k}G_k - C_{2\varepsilon}\rho_m[\frac{\varepsilon^2}{k}] - R_\varepsilon + S_\varepsilon \qquad 6.3(b)$$

$$\mu_t = \rho_m C_\mu \frac{k^2}{\varepsilon} \qquad 6.3(c)$$

where R_ε is additional term related to mean stress and G_k is turbulent kinetic energy production rate, The RNG constants in equation 6.3 are,

$$\sigma_k = 1 \qquad \sigma_\varepsilon = 1.3 \qquad C_\mu = 0.0845$$
$$C_{1\varepsilon} = 1.42 \qquad C_{2\varepsilon} = 1.68 \qquad 6.4$$

while the bulk values for mixture domain are calculated as

$$\rho_m = \sum_{i=1}^{2} \alpha_i \rho_i \qquad 6.5(a)$$

$$\vec{v}_m = \frac{\sum_{i=1}^{2} \alpha_i \rho_i \vec{v}_i}{\sum_{i=1}^{2} \alpha_i \rho_i} \qquad 6.5(b)$$

Specific turbulence source terms for a turbulent bubbly regime (boiling case) are set according to work of Troshko and Hassan [74] as

$$S_k = 0.75 C_{drag} (\rho_l \alpha_v / d_b) \left| \vec{v}_v - \vec{v}_l \right|^2 \qquad 6.6(a)$$

$$S_\varepsilon = 1.35 C_{drag} (S_k / d_b) \left| \vec{v}_v - \vec{v}_l \right| \qquad 6.6(b)$$

For the Eulerian model, the lift and virtual mass source terms are defined through established approaches and corresponding correlations. However, the characteristics of phase interaction require precise adjustment depending on the physical and numerical condition for boiling to obtain stable solutions. These parameters to be considered are briefly explained below.

6.4.3. Non-Equilibrium model

The current flow boiling simulation is based on a non-equilibrium model and is formulated to alleviate a major modelling drawback in the RPI approach that assumes thermal equilibrium between liquid and vapour phases. Similar to the RPI method, it evaluates three wall heat partitioning components, namely the liquid convective, quenching and evaporative heat fluxes. However for more realistic simulation, the

model also includes a fourth heat partitioning component to account for diffusive heat flux of vapour bubble phase, thus removing the equilibrium assumption of vapour being at saturation temperature adopted by the RPI method. The total wall heat flux is given by the summation of the four terms as,

$$\dot{q}_w = (\dot{q}_L + \dot{q}_Q + \dot{q}_E) f(\alpha_1) + (1 - f(\alpha_1))\dot{q}_V \qquad 6.7$$

The first three terms in Equation.6.7 are the heat flux components due to liquid convection, cyclic-averaged transient heat transfer in liquid re-entering the wall region after bubble detachment and the energy for evaporative phase change. $\dot{q}_v = h_v(T_w - T_v)$ is the diffusive heat flux from wall to vapour bubble that accounts for non-equilibrium vapour phase. The function $f(\alpha)$ is the local liquid volume fraction, which is defined by,

$$f(\alpha) = \begin{cases} 1 - \frac{1}{2} e^{-20(\alpha_l - 0.2)} & \alpha_l > \alpha_{Crit} \\ \frac{1}{2}\left(\frac{\alpha_l}{0.2}\right)^4 & \alpha_l < \alpha_{Crit} \end{cases} \qquad 6.8$$

Interfacial area (A_i), which is important parameter due to its effect on drag force and heat transfer process, is basically depends on bubble diameter; however, as it is affected by bubble collision and it has to be modified. For current study interfacial area is calculated as,

$$A_i = \frac{6\alpha_v(1-\alpha_v)}{D_b} \qquad 6.9$$

In equation.6.2, drag force $\vec{F}_{pq}^{\,D}$ for a bubbly boiling case is obtained from correlation defined by Ishii and Zuber [75] as,

$$\vec{F}_{pq}^{\,D} = \frac{A_i}{8}\rho_l C_D \left|\vec{v}_l - \vec{v}_v\right| \qquad 6.10$$

where drag coefficient is determined by choosing minimum of viscous regime (C_D^{vis}) and distorted regime (C_D^{dis}) that are evaluated from,

$$C_D^{vis} = \frac{24(1+0.1\,\mathrm{Re}_b^{0.75})}{\mathrm{Re}_b\sqrt{\max(\alpha_l.0.5)}} \qquad 6.11(a)$$

$$C_D^{dis} = \frac{2d_b\sqrt{g(\rho_l-\rho_v)/\sigma}}{3\times\max(\alpha_l,0.5)} \qquad 6.11(b)$$

$$C_D = \min(C_D^{vis}, C_D^{dis}) \qquad 6.11(c)$$

In the model, the wall region is partitioned into areas covered by either of bubbles or liquid. Bubble diameter of vapour phase is adjusted according to a function suggested by Kurul and Podowski [76] as follows,

$$d_b = \begin{cases} 0.0015 & \Delta T_{Sub} < 0 \\ 0.00015 - 0.0001\Delta T_{Sat} & 0 < \Delta T_{Sub} < 13.5 \\ 0.00015 & \Delta T_{Sub} > 13.5 \end{cases} \qquad 6.12$$

The lift force $\vec{F}_{lift}$ in Equation 6.2-a is computed from the correlation developed by Moraga et al [77] as,

$$\vec{F}_{lift} = C_{lift}\rho_l\alpha_v(\vec{v}_v - \vec{v}_l)\times(\nabla\times\vec{v}_l) \qquad 6.13(a)$$

and

$$C_{lift} = \begin{cases} 0.0767 & \varphi \le 6\times10^3 \\ [0.12-0.2\exp(-\frac{\varphi}{36000})]\exp(\varphi/3\times10^7) & 6\times10^3 \le \varphi \le 1.9\times10^5 \\ 0.002 & \varphi \ge 1.9\times10^5 \end{cases} \qquad 6.13(b)$$

where $\varphi = \mathrm{Re}_b\,\mathrm{Re}_\nabla$. The bubble Reynolds number and bubble shear Reynolds numbers which are used in Equation 6.13 a&b are defined as $\mathrm{Re}_b = d_b\rho_l|v_l - v_v|/\mu_l$ and $\mathrm{Re}_\nabla = d_b^2\rho_l|\nabla\times\vec{v}_l|/\mu_l$ respectively.

$$\vec{F}_{pq}^{TD} = \rho_l k\nabla\alpha_v \qquad 6.14$$

As the vapour bubbles depart the wall, there would be a heat transfer from vapour bubble to replacing liquid phase given by,

$$\dot{q}_{lt} = A_i h_{sl} (T_{sat} - T_l) \quad 6.15$$

where heat transfer coefficient h_{sl} is calculated from correlation suggested by Ranz-Marshal [78] which is

$$h_{sl} = \frac{k_l}{D_b}(2 + 0.6\,\mathrm{Re}^{0.5}\,\mathrm{Pr}^{0.33}) \quad 6.16$$

Additionally interfacial heat transfer (heat transfer from superheated vapour to liquid) is given by,

$$\dot{q}_{vt} = \frac{\alpha_v \rho_v c_{pv}}{0.05}(T_{sat} - T_v) \quad 6.17$$

where time scale is assumed to be 0.05. Accordingly, the interfacial mass transfer which directly depends on corresponding total heat transfer could be calculated as

$$\dot{m}_i = \dot{m}_{lt} + \dot{m}_{lv} = \frac{\dot{q}_{lt} + \dot{q}_{vt}}{h_{fv}} \quad 6.18$$

Interfacial exchange parameters are briefly summarized in Table 6.1.

Table 6.4. Models applied for interactions between phases

Interaction term	Applied Correlation	Comment	Reference
Drag	Eq 6.10 & 6.11	Using bubble diameter	Ishii and Zuber [75]
Lift	Eq 6.13	Calculating coefficient	Moraga et al. [77]
Heat transfer	Eq 6.16	Vapour to liquid heat transfer	Ranz-Marshal [78]
Turbulence source terms	Eq 6.6	Generalized for bubbly regime	Troshko and Hassan [74]
Bubble Diameter	Eq 6.12	Based on degree of sub-cooling	Kurnul and Podowski [76]

Numerical model simulates multi-phase flow and boiling has been briefly mentioned; however, many well-established equations and closures, extensively available in literature, have not been discussed here, as it is not necessary. Intricate and sensitive case of boiling modelling is not limited with explained methodology and not only for each type of modelling (e.g. pool boiling, nucleate boiling) is different numerical

approach recommended but also in tube boiling flow for each different boiling regimes (e.g. bubbly, slug and annular) models' reliability varies.

Since this study examines a curved pipe, designated between sections of $0°$ and $90°$, the body force consists of centrifugal and gravity forces. Considering position and alignment of curved part of geometry shown in Figure 6.1, centrifugal source term in Cartesian coordinate system is given by,

$$\vec{F}_{q-body} = \rho_q \alpha_q \frac{(v_{xq}{}^2 + v_{zq}{}^2)}{x^2 + z^2}(x\hat{i} + z\hat{k}) \qquad 6.19$$

6.5. Results and Discussions

Using the explained multi-phase, turbulent, boiling model, two boiling cases are examined for the geometry represented in Figure 6.1. Both cases, indicated as Case-A ($T_{Sub} = 4.2 \ K$) and Case-B ($T_{Sub} = 12.5 \ K$), are tested for straight and curved channels having rectangular-circular cross sections. Operating pressure is set to be at 4.053 Mpa where uniform heat flux of q=287.5 kW/m^2 is applied on heated section which has a constant length for all cases. Inlet velocity is another constant parameter in this investigation valued at 1.15 m/s.

6.5.1. Grid Analysis and Validation

The simulation uses a hybrid structured mesh of which the grid dependency and the optimum mesh size are determined by a grid sensitivity analysis. For this, the parameter y^+ is used, as this wall function critically needs to satisfy the condition $30 \le y^+ \le 300$ for the applicability of the k-ε (RNG) model. The grid optimisation is done by choosing a certain grid size and checking the compliance with the y^+ requirement, where excessive refinement would result in cells having y^+ below the permitted limit while grid coarsening would increase it above the upper threshold. The present simulation uses a dynamic mesh arrangement, where depending on the flow conditions, the mesh size is adjusted and the optimum is chosen to keep y^+ within the permitted range over all cells in the solution domain.

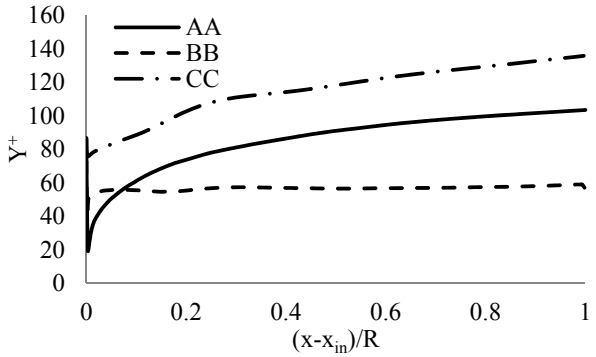

(a) Rectangular Cross-section

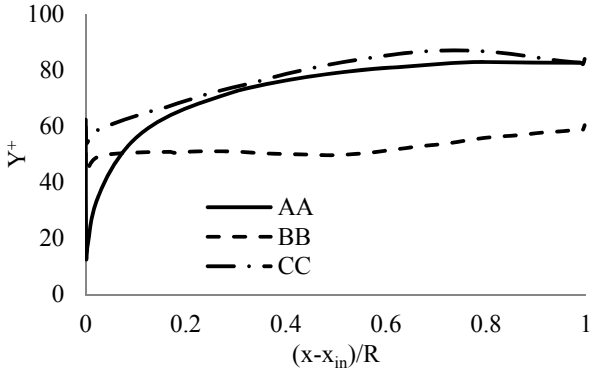

(b) Circular Cross-section

Figure 6.2. Evaluation of y^+ on selected profiles for applied grid

Figure 6.2. illustrates the local values of y^+ for such an optimised mesh for both types of cross-sections. It is evident that the domain contains negligible proportion of cells (1.33 % and 2.73 %) with y^+ below the lower limit of 30, demonstrating excellent compliance of the wall function criterion.

In achieving stable results, the inlet and outlet mass balance and average temperature profiles are also monitored using the standard convergence criteria in addition to satisfying y^+ compliance.

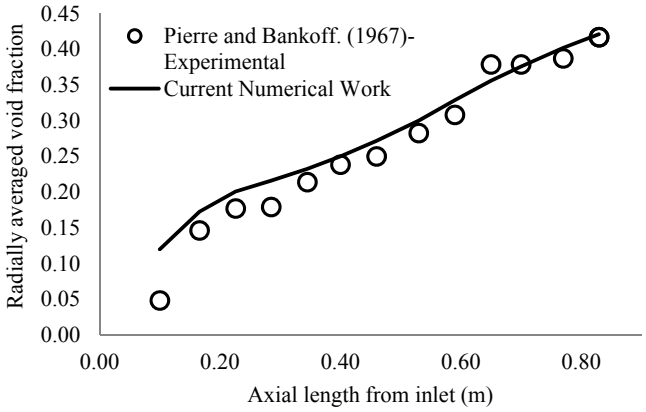

(a) U_{in}=1.15 m/s, q=287.5 kW/m^2, T_{Sub}=4.2 K

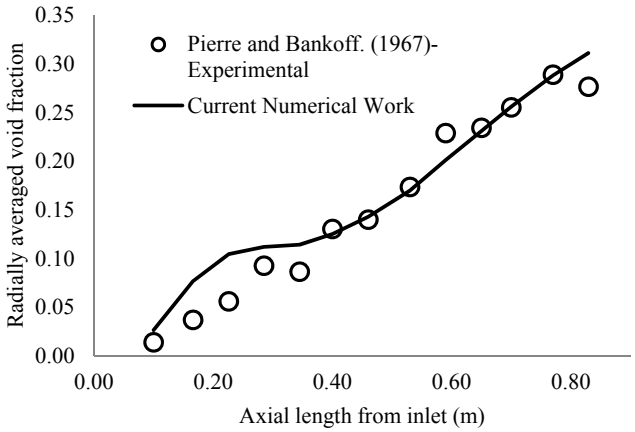

(b) U_{in}=1.15 m/s, q=287.5 kW/m^2, T_{Sub}=12.5 K

Figure 6.3. Validation against experimental results - Void fraction at different axial locations in straight pipe with rectangular cross-section

Figure 6.3 provides a validation of predicted void fraction for straight pipe in current work with the experimental results from Pierre and Bankoff [79]. They used gamma-ray attenuation technique to measure the void fraction in 13 different axial positions and reported results for various operating conditions. In Figure 6.3, the comparison is made for two test cases at a pressure of 4.053 MPa. This shows highly satisfactory agreement between the numerical and experimental values of radially averaged void fraction, indicating the reliability of the present non-equilibrium model.

6.5.2. Phase and wall temperature pattern

Flow and phase pattern in boiling case are crucial as in presence of high heat flux, applied on the tube surface; phase change makes a substantial difference on surface temperature. Phenomena such as dry-out and/or burn-out in boilers are associated with lack of heat convection from tube surface as a result of unpredicted rate of vapour

production. Additionally, boiling is used as a heat transfer enhancement technique: extra heat could be removed by evaporation mechanism as the extra heat is spent on latent heat during phase-change procedure. Therefore, for taking extreme advantages of boiling on surface heat transfer, flow pattern should be optimized with prospective of maximizing quenching heat transfer as well as evaporative heat transfer on the surface. The unique influence of centrifugal force on phase arrangement and vortices structure is shown in Figure 6.4. Bubble diameter, as pointed in numerical approach, has small dimensions as compared to grid size and is considered as a scalar for each cell, on basis of which other related parameter would be calculated. Hence, volume fraction between zero and one resulted from Eulerian approach is justified both physical and numerically. In curved pipe, the void fraction pattern depicts a marked deviation from the "axi-symmetry" observed for straight pipes. It is seen that, in the presence of pipe flow curvature, the vapour phase is highly concentrated closer to the inner wall (left of diagram) while the liquid phase is displaced towards the outer pipe wall (right of diagram). This is because, the centrifugal forces generated by pipe curvature impart more inertia effect on the heavier liquid component, pushing it outwards. Consequently, the void fraction distribution is radially uneven over the pipe cross section unlike in straight pipe. This creates favourable implications on the two-phase boiling heat transfer process, as explained below.

In straight pipe, radially even vapour distribution acts as a uniform thermal barrier for wall heat flow into the liquid. In curved pipe, the void fraction profile biased towards the inner wall improves heat transfer process in two ways. Firstly, it makes the liquid component to have a higher circumferential contact with the heated wall, thus increasing the potential for liquid evaporation. Secondly, at pipe wall areas with thinner vapour distribution, thermal resistance to heat flow from the wall to liquid is reduced. Combination of these mechanisms results in improved overall flow boiling heat transfer rate.

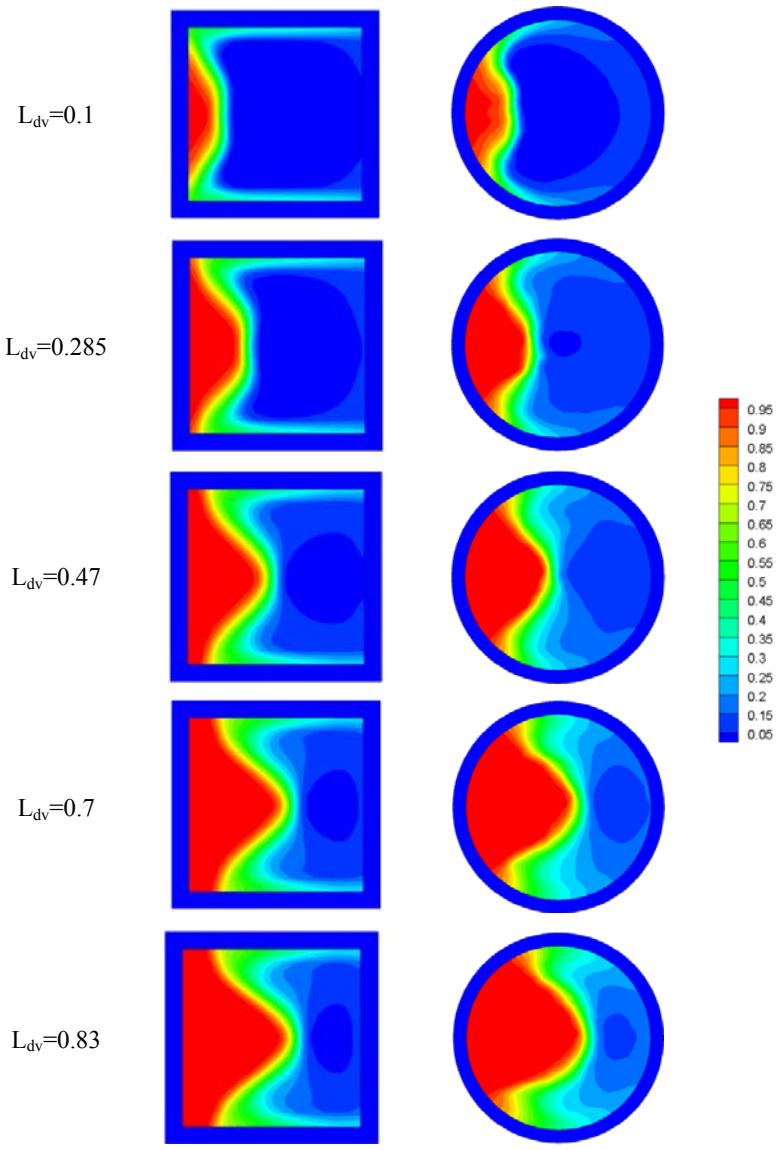

Figure 6.4. Void fraction and dimensionless helicity contours on selected positions (outer wall is located right-side)

As evident in the void fraction contours, qualitative arrangement of phases for rectangular and circular cross section is almost similar and obviously interfacial area is not as sharp as immiscible flow case. Since bubble and liquid elements of flow, due to large density difference, would experience a high difference in centrifugal force, the separation starts from curvature inception. Accordingly, throughout channel the vapour phase remains in area closer to inner wall, liquid phase stocks at outer wall and nucleation sites would largely form on the side walls. The main reason for similar flow and phase pattern for different shapes of cross section is placement of phases on to sides of cross section where no cross-sectional phase takeover happens all through channel.

This intrinsic thermal advantage in curved pipes is clearly illustrated through Figures 6.5 and 6.6.

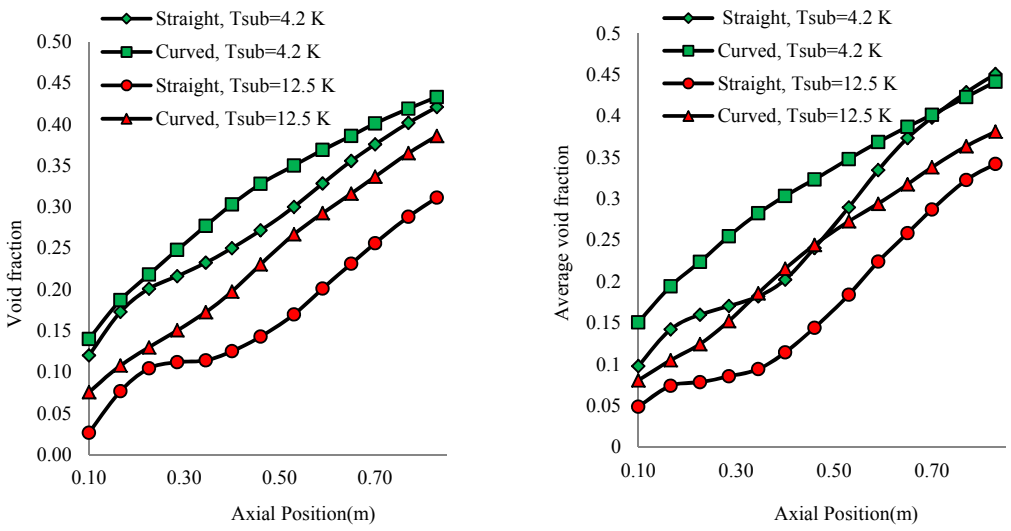

(a) Rectangular cross section (b) Circular cross section

Figure 6.5. Radially-averaged axial void fraction profile for comparison between straight and curved pipe

Figure 6.5 provides the axial variation of the cross sectional void fraction (radially-averaged) for both curved and straight pipes at two liquid sub-cooling values. Considering void fraction for a given axial location, it is observed that flow boiling in curved pipe produces higher volume of vapour than the corresponding straight pipe, regardless of liquid sub-cooling. Also it is noted that, flow boiling in a curved pipe requires shorter length to generate certain void fraction in the flow than in a straight pipe. Thus, it is clearly evident that the pipe curvature acts as a catalyst for enhancing the flow boiling effectiveness. Figure 6.6 provides further evidence for this improved thermal performance.

Average void fraction values are not significantly dependent on shape of cross section as shown in Figure 6.6 (a)&(b). However, there is a marked increase due to curvature effect in vapour generation for both types of rectangular and circular cross sections as compared to straight counterpart.

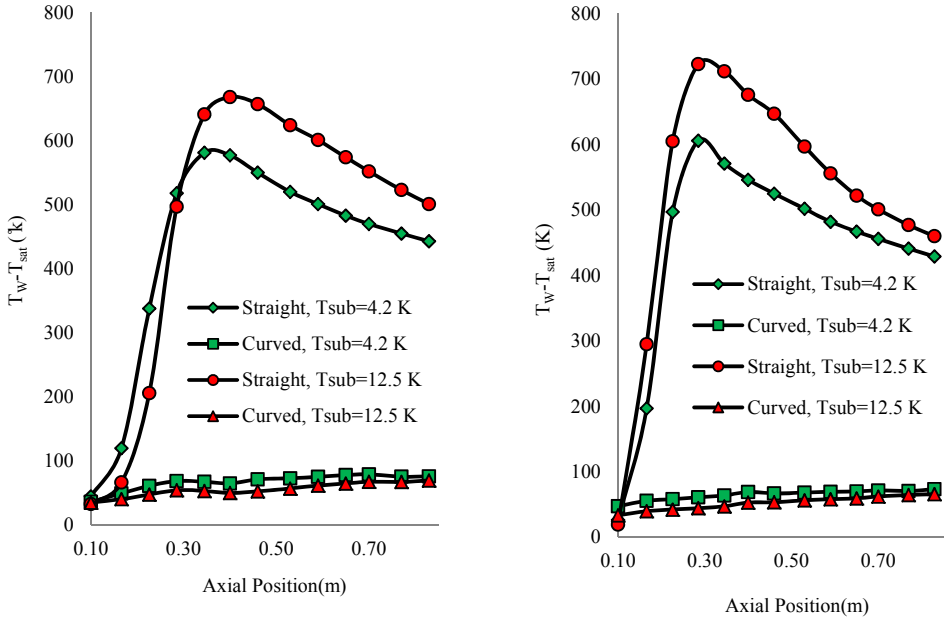

(a) Rectangular cross section (b) Circular cross section

Figure 6.6. Radially-averaged axial wall superheat profile for comparison between straight and curved pipe

In Figure 6.6, the axial variation of wall superheat (radially-averaged) is presented for two liquid sub-cooling values for both curved and straight pipes. In straight pipe, the wall superheat rapidly increases from pipe inlet and then gently falls off as the vapour generation or flow boiling builds up. To the contrary in a curved pipe, the axial wall superheat remains virtually constant at a much reduced value (about 12 times less) over the entire heated pipe. This behaviour implies that the flow boiling in curved pipe begins much closer to the pipe inlet than in straight pipe and the pipe curvature makes the vapour generation process more efficient. Also, it is observed that a curved pipe produces the flow with a given void fraction over a shorter heated length than the corresponding straight pipe, highlighting the improved boiling efficiency.

Flow boiling thermal enhancement in curved pipe is attributed to the skewed profile of void fraction typically illustrated in Figure 6.4. This vapour distribution concentrated around the inner pipe wall allows the liquid component to have a higher contact area with the heated wall whereby the potential for liquid evaporation is increased and the wall superheat is reduced. As such, curved pipes show reduced susceptibility to pipe wall burnout. It is also deduced from Figure 6.7 that the flow boiling process in curved pipe is much less sensitivity to liquid sub-cooling than that in straight pipe. These

trends provide conclusive vindication of the very unique thermal benefits realisable in flow boiling within curved pipes.

Mutual observation of flow and temperature pattern signals that characteristics of boiling heat transfer are majorly factor of phase arrangement rather than vortices structure. Since ratio of each phase surface to total heated surface is almost the same for different cross sections, shape factor is not crucially influential on heat transfer in curved channel under boiling condition.

6.5.3. Wall heat flux mechanisms

A pivotal aspect of the current simulation based on non-equilibrium model is to appraise the wall heat flux components contributing to the overall heat flow. In this, the components considered are: (a) evaporation heat flux (b) heat transfer due to wall quenching (c) convective heat in single phase liquid and (d) convective heat in single phase vapour. Illustrating individual characteristics of these components along the heated pipe length, Figure 6.7&6.8(a) show the profiles for straight pipe and Figure 6.7&6.8 (b), (c) and (d) indicate the profiles for curved pipe at planes AA (inner wall), BB (side wall) and CC (outer wall) indicated in Figure 6.1, respectively for different shapes of cross section.

With reference to Figure 6.7 (a) depicting the straight pipe heat flux behaviour, it is seen that, up to about x/W = 0.25, the wall heat flow is dominated by the evaporative component while the convective heat flux into vapour gradually becomes stronger due to the increased vapour production. Both liquid phase and quenching heat transfer components remain relatively small and insignificant. The two-phase boiling process practically limited up to around x/W = 0.3, where the departure from nucleate boiling (DNB) occurs with the diminishing liquid evaporation leading to pipe wall dry-out. Then the wall heat flux is essentially becomes single phase heat flow in to dry vapour with large pipe wall superheat.

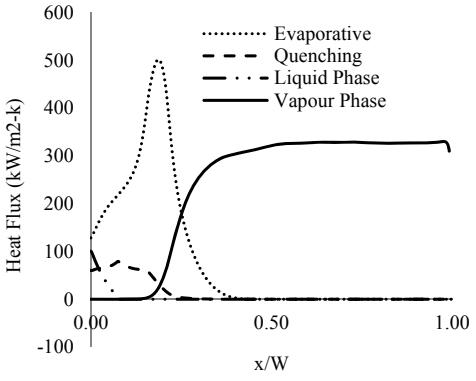

(a) Straight pipe

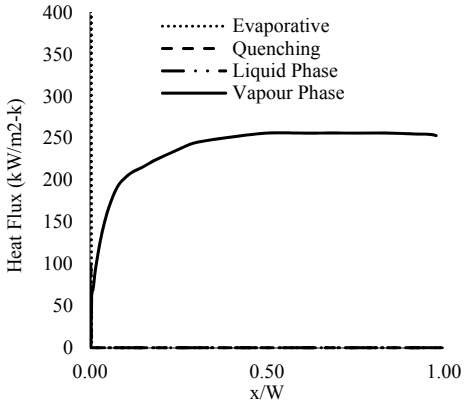

(b) Curved pipe - Profile along AA (*inner wall*)

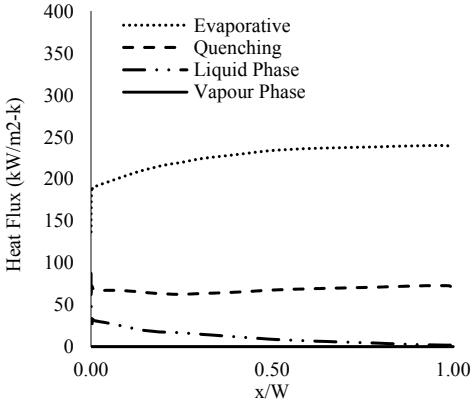

(c) Curved pipe - Profile along BB *(side wall)*

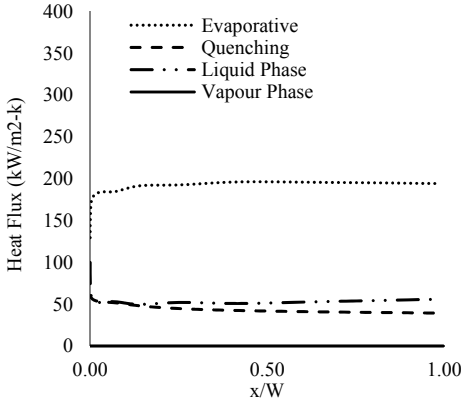

(d) Curved pipe - Profile along CC *(outer wall)*

Figure 6.7. Profiles of wall heat flux components used in simulation model with heat flux partitioning for straight and curved pipes

Curved pipe's unique thermal behaviour in flow boiling is well revealed by the heat flux profiles at AA, BB and CC. The profile for AA (Figure 6.7&6.8 (b)) is much similar to the straight pipe behaviour (Figure 6.7&6.8 (a)) and is dominated by the vapour convective heat flux. The evaporative, liquid phase and quenching heat flux components are insignificantly small and confined to very short length following pipe inlet which is slightly longer for circular cross section (Figure 6.8 (b)). This implies that the inner pipe wall very quickly reaches dry-out conditions, which is to be expected as the curvature effect readily displaces the generated vapour towards the inner pipe wall. The overall heat flux along AA remains predominantly single phase vapour heat flow with large wall heat superheats and pipe wall dry-out.

The profiles along BB and CC given in Figure 6.7&6.8 (b) and (c) portray much similar characteristics. In these, the single phase vapour heat flux component is almost non-

existent over the entire pipe length indicating that the heated wall is primarily exposed to liquid phase. Along the pipe length on BB and CC profiles, the flow boiling occurs without DNB or dry-out. These are attributed to the heavier liquid phase being driven towards the outer pipe wall by the curvature-induced centrifugal forces, as typically demonstrated in Figure 6.4.

Having a large liquid fraction in contact with the outer pipe wall significantly increases number of boiling nucleation sites and accordingly the evaporative wall heat flux component compared to the cases of Figure 6.7&6.8 (a) (straight pipe) and Figure 6.7&6.8 (b) (curved pipe inner wall). The heat flow contributions from single liquid phase and quenching are also significant unlike in straight pipe or along AA for curved pipe. These elevated heat flows combine to provide much higher overall wall heat flux for curved pipe than flow boiling in identical straight pipe.

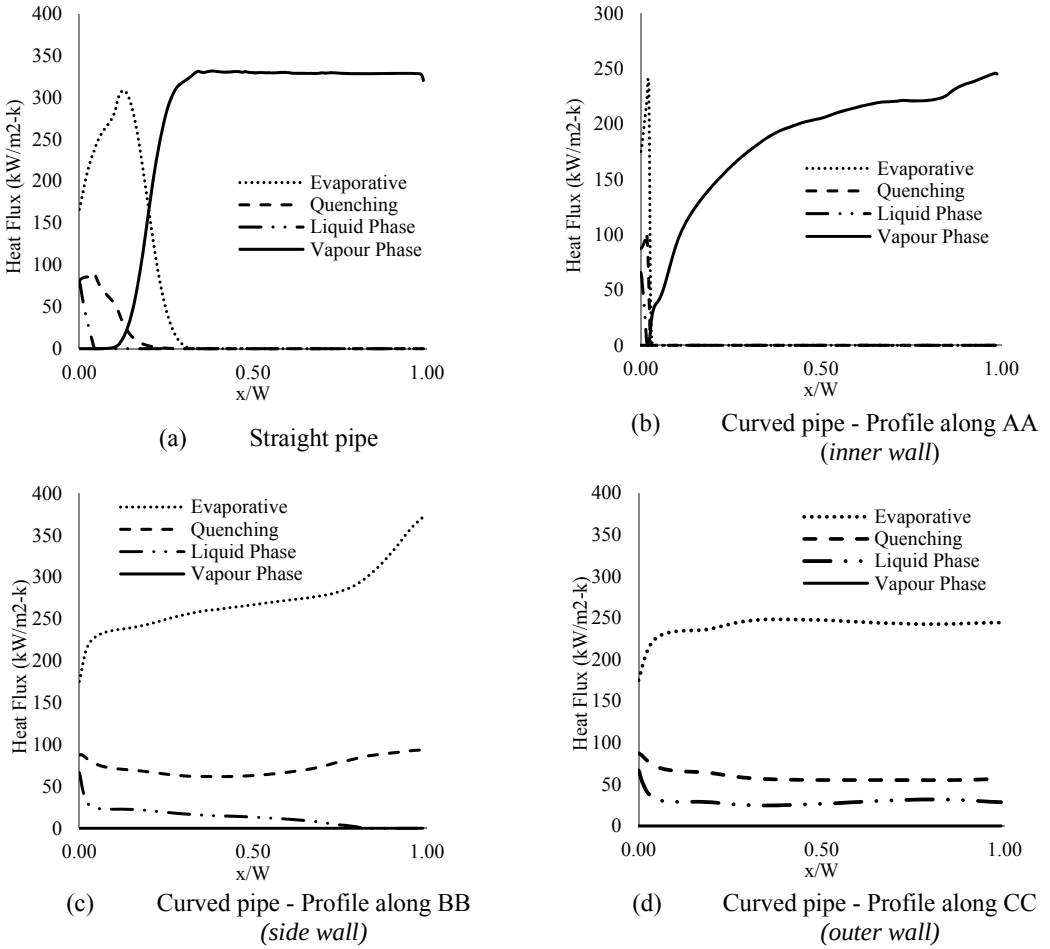

Figure 6.8. Profiles of wall heat flux components used in simulation model with heat flux partitioning for straight and curved pipes

From the above comparative analysis with straight pipe, it is recognised that the curved pipe geometry brings about the secondary flow fluid interaction to the flow boiling process that will delay the departure from nucleate boiling and dry-out at the wall while enhancing the wall heat transfer and reducing the wall superheat. In view of dry-out and burn-out issues associated with boilers tubes, the identified thermal benefits of flow boiling within curved pipe geometry are practically significant and meaningful for sustainable energy resource usage.

Rectangular and circular cross sections have been compared in in term of heat transfer components at the selected cross sections where the emphasis is on effect of curvature. On the given profiles rectangular cross section found to be more effective in vapour generation whereas circular cross section has greater evaporative and quenching heat flux. Such investigation could be extended along with vortices structure assessment, especially to capture effect of sharp corners on temperature rise-up in rectangular cross sections which requires a more detailed analysis.

6.6. Summary

In this chapter, a numerical flow boiling model in curved pipe has been developed incorporating non-equilibrium model with wall heat partitioning, Eulerian multi-phase approach and k-ε turbulence model. The model produces consistent and stable results that are validated against experimental values with a good agreement. The simulation identifies the unique features of flow boiling within curved pipes, where the secondary flow from arising from curvature-induced centrifugal effects significantly alters the boiling regimes and heat transfer characteristics compared to straight pipes.

This numerical analysis concludes that the secondary flow interaction from pipe curvature has intrinsic ability to enhance the thermal effectiveness of flow boiling process by increasing the wall heat flux rates, reducing the wall superheat, delaying the departure from nucleate boiling (DNB) and significantly lowering the possibilities for wall dry-out. Compared to straight pipes, the flow boiling in curved pipes can produce vapour at a higher rate with a shorter pipe length and without much sensitivity to liquid sub-cooling.

Average values of boiling characteristics have been found insensitive against shape of cross section; however, phenomenon such as local temperature increase is observed as a result of vortices structure which could be analysed with more details.

CHAPTER 7

Conclusions

7.1. Research Summary and Significant Outcomes

The study presented in this thesis carried out an extensive review of published literature on the aspects of secondary flow behaviour in single and multi-phase fluid flow through curved channels and the associated heat transfer processes. It identified that, the available simulation methods have yet to provide realistic representations of the complex secondary flow features and their impact on thermal characteristics. Also, the parametric influences of duct geometrical and flow variables remain largely unexplored and poorly understood. Decisive and reliable criteria are presently not at disposal for accurate prediction and identification of Dean vortex generation and the onset of Dean's Instability in curved channel flow fields. Most investigations have been primarily confined to single-phase flow through curved rectangular ducts while the flow behaviours within elliptical and circular geometries have received insignificant priority and attention. Analyses with immiscible and boiling two-phase flow through curved channels are rarer or non-existent. Very few attempts have been made in reported literature to establish suitable techniques to optimise thermal behaviour of fluid flow through heated curved channels in view of practical design requirements. Addressing above key limitations, the study presented in the thesis carefully formulated its research scope, objectives and methodology and, carried out an extensive investigation of which details were presented in previous chapters covering the single phase, immiscible two-phase and two-phase boiling fluid flows through curved channels.

(a) Single-Phase fluid flow in curved channels

Making a significant contribution to improve the current simulation methodologies for single-phase fluid flow, the study developed an advanced three-dimensional numerical model based on (helicity) vortex structures, which is more compatible and congruent with the spiralling fluid motion of secondary flow. In this, necessary User Defined

Functions (UDF) were formulated and integrated into the computational fluid dynamics software package FLUENT as a solver. The adapted modelling approach provides much compliant tracking of vortex flow paths and, very effective capturing of intricate details of secondary vortices, supported by the use of a curvilinear mesh arrangement. The chosen meshes were shown to be more accurate for representing steep flow profiles in a variety of channel geometries attempted. The model was successfully tested for its consistency and prediction accuracy and, validated against the available experimental data to confirm the realisable modelling improvements over the previous models.

In fulfilling a critical analytical need for this field of research, the study formulated two intuitive approaches as a tool for detecting the onset of Dean Instability. One approach using an assigned dimensionless helicity threshold was realised to be universally applicable without fail to all channel shapes and flow conditions, and provided the flexibility to manage the detection accuracy versus computational demand. The second approach using the outer wall pressure gradient profile was found to be extremely useful to obtain prompt qualitative indication of the vortex generation potential. Both techniques are similarly applicable for rectangular geometries while the pressure gradient method was found to over-predict the conditions for Dean's Instability in circular and elliptical ducts. These two criteria are far reliable and accurate than any other reported method in literature while having the provision for performing directly within the computational process.

The single-phase simulation model successfully predicted the fluid flow behaviour within rectangular, elliptical and circular channels, accurately and consistently identifying the onset of Dean's Instability. It precisely captured the centrifugal effects from fluid flow rate, the geometrical influence from channel shape and aspect ratio, and the buoyancy effects from channel wall heating. As such, the study provides unprecedented details on parametric influences with a variety of channel geometries compared to the published work.

The study also developed a useful thermal optimisation technique for heated curved channel flows. Evaluating the individual contributions to flow irreversibilites from heat transfer and fluid viscosity, this proposed technique identified a point of inflection for the overall entropy as practically the best possible "trade-off" between the highest achievable thermal benefits with the least viscous penalty for curved channel flows.

(b) Immiscible Two-Phase fluid flow in curved channels

In view of the relevance to industrial process applications, the simultaneous flow of two non-mixing fluid components within heated curved circular channels was examined. The study developed a new three-dimensional simulation based on Volume of Fraction (VOF) specifically for this type of two-phase flow in circular channel. Suitable mesh arrangements were considered with compatibilities for near-wall turbulence models and capabilities to capture the formations of immiscible fluid phases.

The model was tested for consistency and accuracy. It successfully predicted the unique features arising from the interaction between the centrifugal forces and the momentum transfer between phases. These interactions lead to the formation of secondary vortices simultaneously in each fluid phase. The intensity of phase vortices primarily changed with the velocity ratio between phases, where the flow patterns were dominated by heavier phase at high velocity ratio and by lighter phase at low velocity ratio. As a useful design feature for certain reactive flow processes, it was observed that immiscible flow mixture in a curved channel is able to provide 3.5 times more interfacial area between phases than the corresponding such flows in straight pipes.

It was found in immiscible flows, thermal characteristics are sustained by both forced convection and heat diffusion processes. The former is more contributed by the fluid phase with the higher density for its centrifugal action while the latter by the phase with the higher Prandtl number for its better thermal transport ability. Following the same approach as for single-phase flow, a similar thermal optimisation scheme considering individual phase irreversibilities were successfully developed for this immiscible two-phase fluid flow through curved channels.

A numerical investigation for immiscible two-phase fluid flow in curved channels as presented in this study is not currently reported in the published literature.

(c) Two-Phase flow boiling in curved channels

The single-phase three-dimensional simulation model was modified and extended to describe the two-phase flow boiling processes in curved ducts. This model represents a significant improvement over the previous methods for it applied a realistic approach of wall heat partitioning techniques at the vapour and liquid interfaces. With this, it modelled both mass and heat transfer processes across phase boundaries and included

the interfacial momentum transfer. Thus, this new approach represents the most accurate to-date in terms of physical mechanisms involved among the two-phase flow models for this type of fluid flow with boiling. The model was verified for its consistency and accuracy and, validated against the available experimental data.

The model successfully predicted the unique phase distribution characteristics and boiling heat transfer process in circular channels. It identified that the flow boiling within curved channels is far more efficient than that within straight ducts. In curved channels, wall temperature is significantly reduced while producing higher fraction of vapour than in a corresponding straight duct due to the unique liquid phase distribution driven by the centrifugal forces.

As an overall conclusion, the study presented in this thesis delivers research outcomes that significantly advance the current state of knowledge through new numerical simulation methodologies for multi-phase fluid flow in heated curved channels of various geometries, novel detection methods of Dean's Instability and clearer understanding of secondary flow behaviour in multi-phase flows and associated heat transfer processes.

7.2. Possible Future Research directions

(i) Numerical modelling

The current study is so extensive it seems to have exhausted almost all directions for further numerical work on single-phase flow in curved channels. However, there are more possibilities in multi-phase flow studies. The numerical model developed for the flow boiling heat transfer investigates unique behaviour of phase formation and heat transfer in a limited range of heat flux and Reynolds number. Parametric analysis can be extended for a wider range to observe the influence of various parameters. It would be challenging and interesting to examine the flow behaviour near the critical heat flux condition, where special care may be needed. It would be useful to consider the sub-models suggested by Tentner et al. [80] and Loilev et al. [81] for improved accuracy.

(ii) Experimental work

The vortex-based numerical analysis developed in this study could be verified through the experimental velocity fields. Flow visualisation and quantitative assessment of the

secondary flow vortices are a major challenge because of the intrusive nature of experimental probes such as hot-wire anemometer. Promising optical methods are LDA (or LDV), LIF and PIV where it would be possible to obtain the necessary data sets for the complex flow fields in curved channels. Recent technical development is Stereo-PIV which provides sophisticated real-time fluid field analysis for measuring three-dimensional velocity fields. Such data set would be useful for combining with the helicity threshold method for verifying the formation process of secondary vortex structures and Dean's Instability. Currently, such data do not exist.

Obtaining the flow temperature profiles in curved channels is a challenge that has not been sufficiently addressed. Planar-LIF methods would allow such complex measurements of thermal fields in curved channels for quantitative local temperatures, permitting confident numerical validations.

Application of optical method for boiling case might be challenging and needs special consideration since the measuring systems require tolerating high heat fluxes of the order of 30-800 kW/m^2, where maintaining wall transparency would be an issue. However, it may be possible to use traditional approaches suggested by Pierre and Bankoff [79] to obtain some elementary parameters such as volume fraction or surface temperature for boiling heat transfer in curved channels.

References

1. J. Eustice, Flow of Water in Curved Pipes, Proceedings of the Royal Society of London. Series A, 84 (568) (1910), pp. 107-118.
2. J, Eustice, Experiments on Stream-Line Motion in Curved Pipes, Proceedings of the Royal Society of London. Series A,.85(576) (1911), pp. 119-131.
3. W.R. Dean, Note on the motion of fluid in a curved pipe, Philosophical Magazine Series 7, Vol.4:20 (1927), pp 208-223.
4. W.R. Dean, The stream-line motion of fluid in a curved pipe, Philosophical Magazine Series 7, 5:30 (1927), pp 673-695.
5. W. R. Dean, Fluid Motion in a Curved Channel, Proceedings of the Royal Society of London. Series A, 121 (787) (1928), pp. 402-420. recommend
6. C. M. White, Streamline Flow through Curved Pipes, Proceedings of the Royal Society of London. Series A, 123 (792) (1929), pp. 645-663.
7. J.A. Baylis, Experiments on laminar flow in curved channels of square section, Journal of Fluid Mechanics, 48(3) (1971), pp 417–422.
8. J.A.C. Humphrey, A.M.K. Taylor, J.H. Whitelaw, Laminar flow in a square duct of strong curvature, Journal of Fluid Mechanics, 83 (1977), pp 509–527.
9. K.C. Cheng, J. Nakayama, M. Akiyama, Effect of finite and infinite aspect ratios on flow patterns in curved rectangular channels, in: Flow Visualization International Symposium, Tokyo, October 1977, p. 181.
10. Ghia, K.N., Sokhey, J.S., Laminar incompressible viscous flow in curved ducts of rectangular cross-section, Journal of Fluids Engineering, 99 (1977), pp. 640–648.
11. M. M. Enayet, M. M. Gibson and M. Yianneskis, Measurements of turbulent developing flow in a moderately curved square duct, International journal of heat and fluid flow, Vol 3 (4) (1982), pp 221-224.
12. Sugiyama, Taro Hayashi, Koji Yamazaki, Flow Characteristics in the Curved Rectangular Channels, Bullletin of JSME, 26(216) (1983), pp 532-552.
13. Dong, Z.F., and Ebadian, Numerical analysis of laminar flow in curved elliptic ducts, Journal of Fluid Engineering, 113 (1991), pp. 555-562.
14. T. Chandratilleke, Nursubiyakto. "Numerical prediction of secondary flow and convective heat transfer in externally heated curved rectangular ducts." International Journal of Thermal sciences, 42(2002), pp. 187–198.

15. H. Fellouah, C. C., A. Ould El Moctar, H. Peerhossaini "A criterion for detection of the onset of Dean instability in Newtonian fluids." European Journal of Mechanics B/Fluids, l25 (2006), pp 505–531.
16. L. Helin, L. Thais, G. Mompean, Numerical simulation of visco-elastic Dean vortices in a curved duct, Journal of Non-Newtonian Fluid Mechanics, 156 (2009), pp 84-94.
17. H. Fellouaha, C. Castelainb, A. Ould-El-Moctarb, H. Peerhossaini, The Dean instability in power-law and Bingham fluids in a curved rectangular duct, J. Non-Newtonian Fluid Mech, 165 (2010), pp. 163–173.
18. K. C. Cheng and Mitsunobu Akiyama, Laminar forced convection heat transfer in curved rectangular channels, international of heat and mass transfer, 13 (1970), pp. 471-490.
19. Y. Mori, Y. Uchida, T. Ukon, Forces convective heat transfer in a curved heat channel with a square cross section, International journal of heat and mass transfer,14 (1971), pp. 1787-1805.
20. V. P. Tyagi and V. K. Sharma, An analysis of steady fully developed heat transfer in laminar flow with viscous dissipation in a curved circular duct, International journal of heat and mass transfer, vol.18, (1975), pp 69-78.
21. Hoon Ki Choi, Seung O. Parkt, Mixed convection flow in curved annular ducts, International Journal of Heat and Fluid Flow, 37 (17) (1994), pp. 2761-2769.
22. M. J. Targett, W. B. Retallick and S. W. Churchill, Local coefficients for forced convection in curved rectangular channels of large aspect ratio with unequal uniform heating, International Journal of Heat and Mass Transfer, Vol.38(11) ,(1995), pp. 1989-1999.
23. P. M. Ligrani and S. Choi, Effects of Dean vortex pairs on surface heat transfer in curved channel flow, International Journal of Heat and Mass Transfer, 39(1) (1996), pp. 27-37.
24. P. M. Ligrani and S. Choi, A. R. Schallert and P. Skogerboe, Mixed convection in straight and curved channels with buoyancy orthogonal to the forced flow, International Journal of Heat and Mass Transfer, 1996, 39(12): 2473-2484.
25. P. M. Ligrani and C. R. Hedlund, Transition to turbulent flow in curved and straight channels with heat transfer at high Dean number, International Journal of Heat and Mass Transfer 41(12) (1998), pp. 1739-1748.

26. Ricardo Junqueira Silva, Ramon Molina Valle, Marcio Ziviani, Numerical hydrodynamic and thermal analysis of laminar flow in curved elliptic and rectangular ducts, International journal of thermal science, 38 (1999), pp. 585-594.
27. C. R. Andrade and E. L. Zaparoli, Effect of temperature-dependent viscosity on fully developed laminar forced convection in curved duct, International communication in heat and mass transfer, 28(2) (2001), pp. 211-220.
28. J. Christopher Sturgis, I. Mudawar, Single phase heat transfer enhancement in a curved rectangular channel subjected to concave heating, International Journal of Heat and Mass Transfer 42(7) (1999), pp. 1255–1272.
29. T.T. Chandratilleke, Performance enhancement of a heat exchanger using secondary flow effects, in: Proc. of 2nd Pacific—Asia Conf.Mech. Eng., Manila, Philippines, 9–11 September, 1998.
30. T.T. Chandratilleke, Secondary flow characteristics and convective heat transfer in a curved rectangular duct with external heating, 5th World Conference On Experimental Heat Transfer, Fluid Mechanics and Thermodynamics [ExHFT-5], Thessaloniki, Greece, September 24–28, 2001.
31. S. Yanase, R. N. Mondal, Y. Kaga, Numerical study of non-isothermal flow with convective heat transfer in a curved rectangular duct, International Journal of Thermal Sciences 44 (2005),.pp. 1047–1060.
32. Ko. T. H, K. Ting, Entropy generation and optimal analysis for laminar forced convection in curved rectangular ducts: A numerical study, International Journal of Thermal Sciences, 45 (2006), pp. 138–150.
33. Ko, T. H. "Numerical investigation on laminar forced convection and entropy generation in a curved rectangular duct with longitudinal ribs mounted on heated wall." International Journal of Thermal Sciences, 45 (2006), pp. 390–404.
34. Ko, T. H. "A numerical study on entropy generation and optimization for laminar forced convection in a rectangular curved duct with longitudinal ribs." International Journal of Thermal Sciences, 45 (2006), pp. 1113–1125.
35. Ko, T. H, "A numerical study on entropy generation induced by turbulent forced convection in curved rectangular ducts with various aspect ratios." International Communications in Heat and Mass Transfer 36 (2008), pp. 25-31.
36. Liqiu Wang, Fang Liu, Forced convection in slightly curved micro-channels, International Journal of Heat and Mass Transfer,50 (2007), pp. 881–896.

37. Fang Liu, Liqiu Wang, Analysis on multiplicity and stability of convective heat transfer in tightly curved rectangular ducts, International Journal of Heat and Mass Transfer, 52 (2009), pp. 5849–5866.
38. Jiangfeng Guo , Mingtian Xu , Lin Cheng, Second law analysis of curved rectangular channels, International Journal of Thermal Sciences, 50 (2011), pp. 760-768.
39. P. Poskas, V. Simonis, V. Ragaisis, Heat transfer in helical channels with two-sided heating in gas flow, International Journal of Heat and Mass Transfer, 54 (2011), pp. 847–853.
40. Wu-Shung Fu, Chung-Jen Chen, I-Chou Liu, Liang-Ying Hou, Experimental investigation for effects of a reciprocating motion on mixed convection of a curved vertical cooling channel with a heat top surface, International Journal of Heat and Mass Transfer, 54 (2011), pp. 5109–5115.
41. Hui Gao, Liejin Guo, Ximin Zhang, Liquid–solid separation phenomena of two-phase turbulent flow in curved pipes, International Journal of Heat and Mass Transfer, 45 (2002), pp. 4995–5005.
42. Yong-Ming Shen, Chiu-On Ng, Hao-Qing Ni, 3D numerical modelling of non-isotropic turbulent buoyant helicoidally flow and heat transfer in a curved open channel, International Journal of Heat and Mass Transfer, 46 (2003), pp 2087–2093.
43. Vimal Kumar, Mohit Aggarwal, K.D.P. Nigam, Mixing in curved tubes, Chemical Engineering Science, 61 (2006), pp. 5742–5753.
44. Chi-Chuan Wang, Ing Youn Chen, Yur-Tsai Lin, Yu-Juei Chang, A visual observation of the air–water two-phase flow in small diameter tubes subject to the influence of vertical return bends, chemical engineering research and design, 86 (2008), pp. 1223–1235.
45. Donata M.Fries and Philipp Rudolf von Rohr, Liquid mixing in gas–liquid two-phase flow by meandering micro-channels, Chemical Engineering Science 64 (2009), pp. 1326-1335.
46. M. O. Lutset, Experimental Study of Temperature Distribution in the Vicinity of Film Boiling. Heat and mass transfer and physical gas dynamics, 38(4) (2000), pp. 623-630.

47. M. Shiotsu, K. Hama, Film boiling heat transfer from a vertical cylinder in forced flow of liquids under saturated and sub-cooled conditions at pressures. Nuclear Engineering and Design, 200 (2000), pp. 23–38.
48. W. Liu, H. Nariaib, F. Inasaka, Prediction of critical heat flux for sub-cooled flow boiling. International Journal of Heat and Mass Transfer, 43 (2000), pp. 3371-3390.
49. Baduge Sumith, Fumito Kaminaga, Kunihito Matsumura, Saturated flow boiling of water in a vertical small diameter tube, Experimental Thermal and Fluid Science,. 27 (2003), pp. 789–801.
50. Xiangdong Li, Rongshun Wang, Rongguo Huang, Yumei Shi, Numerical investigation of boiling flow of nitrogen in a vertical tube using the two-fluid model. Applied Thermal Engineering, 26 (2006), pp. 2425–2432.
51. Bostjan Koncar, Eckhard Krepper, CFD simulation of convective flow boiling of refrigerant in a vertical annulus, Nuclear Engineering and Design, 238 (2008), pp. 693–706.
52. R. Sindhuja, A.R. Balakrishnan, S. Srinivasa Murthy, Post-CHF heat transfer during two-phase up-flow boiling of R-407C in a vertical pipe, Applied Thermal Engineering. 30 (2010), pp. 167–173.
53. C.N. Chen, J.T. Han, T.C. Jen, L. Shao, Dry-out CHF correlation for R134a flow boiling in a horizontal helically-coiled tube, International Journal of Heat and Mass Transfer, 54 (2011), pp. 739–745.
54. J. Christopher Sturgis, I. Mudawar, Critical heat Flux in a long, curved channel subjected to concave heating, International Journal of Heat and Mass Transfer, 42 (1999), pp. 3831-3848.
55. Jong Chull Jo, Woong Sik Kim, Chang-Yong Choi and Yong Kab Lee, Numerical Simulation of Sub-cooled Flow Boiling Heat Transfer in Helical Tubes, Journal of Pressure Vessel Technology ASME, 131(1) (2009) 011305-1.
56. F. M. White, Viscous Fluid Flow, (1974), McGraw-Hill
57. H. Versteeg, W. Malalasekra, An Introduction to Computational Fluid Dynamics: The Finite Volume Method Approach (2nd Edition), (2007), John Wiley & Sons Inc.
58. A. Bejan, Convective Heat Transfer (2nd Edition), (1995), John Wiley & Sons Inc.
59. F. P. Incropera, Dewitt, Bergman, Lavine, Fundamental of Heat and Mass Transfer (6th Edition), (2007), John Wiley & Sons Inc.

60. D. C. Wilcox, Turbulence Modelling for CFD (3rd Edition), (2010), DCW Industries Inc.
61. G. F. Muchnik, S. D. Solomonov,A. R. Gordon, Hydrodynamic Development of a Laminar Velocity Field in Rectangular Channels, Fizicheskii Zh,. 25(4) (1973), pp. 671–675.
62. Joe F. Thompson, Bharat K. Soni, Nigel P. Weatherill, Handbook of Grid Generation, (1998), CRC Press.
63. ANSYS FLUENT Theory guide (Release 13.0), (2010), Southpointe: ANSYS Inc.
64. O. Ubbink, Numerical prediction of two fluid systems with sharp interfaces, PhD Thesis, the University of London (1997).
65. A. Bejan, Entropy Generation Minimization, (1996), Florida: CRC Press Inc.
66. Adrian Wegmann, Philipp Rudolf von Rohr, Two phase liquid–liquid flows in pipes of small diameters, International Journal of Multiphase Flow, 32 (2006), pp. 1017–1028.
67. H. H. Kruse and M. Schroeder, Fundamentals of lubrication in refrigerating systems and heat pumps, International Journal of Refrigerating, 8 (1985).
68. M. Sunami, K. Takigawa, S. Suda, New Immiscible Refrigeration Lubricant for HFCs, (1994), International Refrigeration and Air Conditioning Conference. Paper 237.
69. D. D. Joseph, M. Renardy and Y. Renardy, Instability of flow of two immiscible liquids with different viscosities in a pipe, International Journal of Fluid Mechanics, 141 (1984), pp. 309-317.
70. C. D. Eastwood, L. Armi , J. C. Lasheras, The breakup of immiscible fluids in turbulent flows, International Journal of Fluid Mechanics, 502 (2004), pp. 309–333.
71. S. Vashisth, K.D.P. Nigam, Prediction of flow profiles and interfacial phenomena for two-phase flow in coiled tubes, Chemical Engineering and Processing, 48 (2009), pp. 452–463.
72. E. Olsson, G. Kreiss, A conservative level set method for two phase flow, Journal of Computational Physics, 210 (2005), pp. 225–246.
73. J.U. Brackbill, D.B. Kothe, C.Zemach, A continuum method for modelling surface tension. Journal of computational Physics,100 (1992), pp. 335-354.
74. A.A.Troshko, Y.A.Hassan, A two-equation turbulence model of turbulent bubbly flows, International Journal of Multi-phase Flow, 27 (2001), pp. 1965-2000.

75. Mamoru Ishii, Novak Zuber, Drag Coefficient and Relative Velocity in Bubbly, Droplet or Particulate Flows, AlChE Journal, 25(5) (1979), pp. 843-855.
76. N. Kurul and M.Z. Podowski, On the modelling of multidimensional effects in boiling channels, In proceedings of the 27th national heat transfer conference, Minneapolis, (1991), Minnesota, USA.
77. F.J. Moraga, R.T. Bonetto, R.T. Lahey, Lateral force on spheres in turbulent uniform shear flow. International journal of Multiphase flow, 25 (1999), pp. 1321-1372.
78. W.E. Ranz and W.R. Marshal. Evaporation from dros, Part i and Part ii. Chm. Eng. Prog.. 48(4) (1952), pp. 173-180.
79. C. C. St. Pierre, S. G. Bankoff, Vapor Volume Profiles in Developing Two-Phase Flow, International Journal of Heat and Mass Transfer, 10 (1967), pp. 237-249.
80. A. Tentner, S.Lo and V.Kozlov, "Advances in Computational Fluid Dynamics Modelling of Two-phase Flow in a Boiling Water Reactor Fuel Assembly", International conference on nuclear engineering, Miami Florida (2006).
81. A. Loilev, M.Samigulin and V.Ustinenko, Advances in Modelling of Cladding Heat Transfer and Critical Heat Flux in Boiling Water Reactor Fuel Assemblies, The 12th International Topical Meeting on Nuclear Reactor Thermal Hydraulics (NURETH-12). Pittsburgh, Pensylvania (2007).